Formation of massive early-type galaxies at z=3 studied by deep near-infrared imaging and spectroscopic observations

博士論文

Formation of massive early-type galaxies at z=3 studied by deep near-infrared imaging and spectroscopic observations

(近赤外線深撮像・分光観測による赤方偏移z=3での大質量早期型銀河形成の研究)

久保　真理子

平成 ２５年

2

-

ABSTRACT

Formation histories of massive early-type galaxies is one of the key questions to solve how stars have been formed and assembled in the galaxies since they are most massive galaxies in the universe. We studied this question from these two studies; 1. The deep near-infrared (NIR) imaging and spectroscopic observations of the protocluster at $z = 3.09$ in the SSA22 field; 2. The observations of the objects with multiple stellar components at $z = 2-3$ which may be the early-phase of the formation history of massive early-type galaxies.

We studied the SSA22 protocluster, which is known as one of the most significant structures at high redshift, by using deep and wide NIR imaging and spectroscopic data taken with Multi-Objects InfraRed Camera and Spectrograph (MOIRCS) equipped on Subaru Telescope ($K_{\rm AB} < 24$ and 111.8 arcmin^2). We selected the candidate protocluster galaxies with photometric redshifts ($z_{\rm phot}$) based on the spectral energy distribution (SED) fittings. Then we found a surface number density excess of the K-band selected galaxies at $2.6 < z_{\rm phot} < 3.6$. Especially, the Distant Red Galaxies (DRGs; $J-K_{\rm AB} > 1.4$), Hyper Extremely Red Objects (HEROs; $J - K_{\rm AB} > 2.1$), galaxies detected in *Spitzer* MIPS 24 μm, *Chandra* X-ray and quiescent galaxies selected from rest-frame UV-NIR colors at $2.6 < z_{\rm phot} < 3.6$ show more significant density excesses. This suggests that massive early-type galaxies in the clusters of galaxies in the current universe are just forming in this protocluster.

To confirm the protocluster memberships of these candidates, we conducted the NIR spectroscopic observations with MOIRCS. We observed 67 galaxies and confirmed redshifts of 39 galaxies; 24 of them are certainly the protocluster members. Notable fraction of the DRGs, HEROs, 24 μm sources and X-ray sources among the targets are the protocluster members, which supports our results from the imaging observations.

First of all, we characterized the structure of the SSA22 protocluster by using the velocity dispersion and number density of the protocluster galaxies. As a result, we obtained that the mass of the SSA22 protocluster is several 10^{14} M$_\odot$ to 10^{15} M$_\odot$, suggesting that the SSA22 protocluster is very rare density peak at $z \sim 3$ and likely to be one of the progenitors of most massive clusters of galaxies in the current universe.

Then we investigated the properties of the protocluster galaxies, which may be the progenitors of massive early-type galaxies hosted in most massive clusters of galaxies in the current universe. A large stellar mass, comparable to a half of Coma cluster have already been formed. The reddest galaxies in the protocluster ($J - K_{\rm AB} > 2.4$) have the SEDs dominated by old stellar populations. It supports the early-formation of massive early-type galaxies in such a high density region. Most of them are also detected in X-ray, suggesting the quenching of their star-formation activities by the active galactic nuclei (AGN).

We also identified the multiple stellar components of the Lyα Blobs and ASTE/AzTEC sub-mm sources in the SSA22 protocluster. They are likely to be multiple mergers of stellar components at the early-phase of the formation histories of massive elliptical galaxies, predicted in the cosmological numerical simulations. Their stellar components are certainly dynamically bounded and with small velocity offsets. Some of them have multiple old stellar components, which suggest that it have taken long times from the formation of the stellar components to merge to the central objects. This picture is consistent with the predicted scenario of formation of massive ellipticals via hierarchical multiple mergers.

-

Contents

6

-

Chap.1. INTRODUCTION

1. FORMATION OF MASSIVE EARLY-TYPE GALAXIES

Formation history of massive early-type galaxies is one of the key to solve how stars formed in the universe. Early-type galaxies are the dominant population in the core of clusters of galaxies in the current universe. They have several characteristics e.g., large stellar mass; old stellar populations; a tight color-magnitude relation, i.e., red sequence (e.g., Bower et al. 1992). These characteristics give us several constraints about their formation histories. For example, tight color-magnitude relation they obey suggests that bulk of the stars of early-type galaxies should have been formed early; It is known that the red sequence already exist as early as at $z \sim 1$ (e.g., Ellis et al. 1997; Stanford et al. 1998). The red sequence at $z > 2$ in the protoclusters, high density region at high redshift are also studied (e.g., Zirm et al. 2007; Kodama et al. 2007). They reported that the red sequence at the brightest-end are already seen at $z \sim 2$ while the red sequence is not significant at $z > 3$. On the other hand, the peak of cosmic star-formation density is found as $z = 2-4$ (e.g., Hopkins & Beacom 2006). Massive early-type galaxies might be some of the effective star-formers at that epoch.

In a last decade, many red galaxies at $z > 2$, which are very plausible progenitors of massive galaxies in the current universe have been studied by using the deep imaging observations at NIR wavelength.

Distant Red Galaxies (DRGs; Franx et al. 2003) are selected based on the simple color selection, $J - K_{\rm vega} > 2.3$ ($J - K_{\rm AB} > 1.4$). By this color criterion, we can select the dusty star-forming red galaxies and/or old red galaxies with significant Balmer/4000Å breaks at $z = 2 - 4$. It is shown from further studies of DRGs that they have large stellar mass and are typically dominated by dusty star-forming galaxies while some of them are the galaxies dominated by old stellar population (e.g., van Dokkum et al. 2004; Labbé et al. 2005; Papovich et al. 2006).

Massive quiescent galaxies found at high redshift are also thought to be the progenitors of massive early-type galaxies in the current universe. The massive quiescent galaxies with spectroscopically confirmed redshifts were identified up to $z \approx 3$ (e.g., Daddi et al. 2005; van Dokkum et al. 2008; Gobat et al. 2012) while the candidates are found at $z > 4$ (e.g., Straatman et al. 2013). It have been reported that massive early-type galaxies at $z > 1.5$ typically have remarkably compact structures. They have elliptical like morphologies but the sizes of them are a few times smaller than the early-type galaxies with similar stellar mass in the local universe. In consequence, the surface stellar mass densities of them are 1-2 orders of magnitude higher than the local galaxies with similar stellar mass (e.g., Daddi et al. 2005; Trujillo et al. 2006; van Dokkum et al. 2008). It is also reported that the massive quiescent galaxies at high redshift are dominated by such compact ones but compact massive early-type galaxies in the current universe seem to be rare (e.g., Cassata et al. 2011; Cassata et al. 2013), although there still remain arguments about the observational bias of the local objects (e.g., Poggianti et al. 2013; Stockton et al. 2014). Suppose that massive early-type galaxies at high redshift are dominated by the compact objects which are not seen in the local universe, there should be further structural evolutions of them through e.g., minor and/or dry mergers.

Clustering strength of the galaxies also inform us what are the progenitors of massive galaxies in the current universe. The clustering strength of the spatial distribution of the galaxies reflects the mass of the host dark matter halos where the clustering strength of the

dark matter halo depends on halo mass (e.g., Mo & White 1996). Adopting some models of the redshift evolution of clustering strength of dark matter halo (e.g., Sheth & Tormen 1999), we can investigate the relations between the progenitors at high redshift and the ancestors in the current universe. The dependence of the clustering strength on the properties of the galaxies at high redshift is studied in many studies (e.g., Daddi et al. 2003; Ichikawa et al. 2007; Quadri et al. 2007; 2008). The red galaxies like DRGs are one of the most strongly clustered galaxies at $z \sim 2-4$. Therefore, they are likely to be hosted in most massive dark matter halos and plausible to be the progenitors of the most massive galaxies in the current universe. The sub-mm galaxies (SMGs e.g., Tamura et al. 2009), rest-frame UV selected galaxies at $z > 4$ (it may be due to the fact that only the galaxies at bright-end have been investigated. e.g., Adelberger et al. 2005; Ouchi et al. 2010) also show strong clusterings and are likely to be the progenitors of most massive galaxies in the current universe.

Several formation models of massive early-type galaxies have been proposed. The monolithic collapse of gas cloud (Eggen et al. 1962) or mergers of massive disk galaxies (Toomre & Toomre 1972) had been proposed in early studies.

The formation histories of massive early-type galaxies are also predicted from the recent high resolution cosmological numerical simulations (e.g., Meza et al. 2003; De Lucia et al. 2006; Naab et al. 2007; Dekel et al. 2009a). There are two major formation modes of massive early-type galaxies in these simulation; in situ formation (mergers of clumps formed by gravitational instabilities of gaseous disk) and also hierarchical multiple mergers of galaxies. The early phase of both modes may be seen as gravitationally bounded small clusters of multiple stellar components. The properties of remnant ellipticals depend on the properties of the stellar components, e.g., wet or dry.

The plausible such phenomena are found from the recent deep NIR imaging observations obtained by using Hubble Space Telescope (HST) or 8-10 m class telescopes (e.g., Prescott et al. 2012; Uchimoto et al. 2012; Umehata et al. submitted). They are important objects to study the formation history of massive early-type galaxies.

2. THE PROTOCLUSTERS

Although some massive quiescent galaxies have been found at $z > 2$, the relationships of them with massive early-type galaxies in the local universe are not so clear. Namely, whether compact massive quiescent galaxies at high redshifts are actually the progenitors of bulk of massive early-type galaxies and if so, how they evolved into normal ellipticals. Therefore we study the protocluster, namely the progenitors of the clusters of galaxies in the current universe since massive early-type galaxies dominate the core of clusters of the galaxies in the local universe. Not only to study the progenitors of massive early-type galaxies, the protoclusters are also important to study the structure formation in the universe.

The clusters of the galaxies at $z < 1$, sometimes at $z \sim 1.5 - 2$ are found from detection of their central extended X-ray sources originated in the hot virialized gas at the center of clusters of galaxies. Sunyaev-Zeldovich (SZ) effect is also used to search clusters of galaxies, namely the distortion of cosmic microwave background (CMB) radiation when the CMB photons encounter the energetic electrons in hot central cluster gas and gain energies (inverse-Compton effect). But it is difficult to find the progenitors of the clusters of galaxies from these ways at higher redshift.

Instead, the protoclusters at $z > 1$ are found as the overdensities of galaxies. They are generally found from the narrow-band surveys of Lyα emitters (LAEs), Hα emitters (HAEs) and also color selection of LBGs around the radio galaxies (e.g., Steidel et al. 2005; Kurk et al. 2004; Venemans et al. 2007; Kodama et al. 2007; Overzier et al. 2009; Tanaka et al. 2011; Matsuda et al. 2011). Since the powerful radio galaxies are thought to be the progenitors of the brightest cluster galaxies in clusters of galaxies in the current universe, they are thought to be tracers of the protoclusters and actually the overdensity of the galaxies are found around the radio sources. Some protoclusters are found from the blank field surveys (e.g., Steidel et al. 1998; Toshikawa et al. 2012; Spitler et al. 2012). One of the most famous protocluster is the SSA22 protocluster at $z = 3.09$ (Steidel et al. 1998, 2000), which we are going to study.

When we study the protoclusters, we have to keep in mind to compare structures which will evolve into similar structures in the current universe. It is well known that there are the environmental dependence on the properties of the galaxies in the current universe (e.g., Oemler 1974; Dressler 1980; Kauffmann et al. 2004). It is predicted in the biased structure formation scenario in the CDM universe that the galaxies are preferentially formed from the density peaks in the high density region at high redshift (Kaiser 1984). Then it is needed to compare the clusters of galaxies which will evolve into similar structures in the current universe to study the evolution of galaxies in the protoclusters.

The clusters of galaxies at $z < 1$ are characterized their dynamical masses from their central extended X-ray sources but it is difficult to detect such X-ray sources at higher redshift. Instead, the velocity dispersion of the galaxies in the protoclusters are used to characterize the dynamical mass of the protoclusters (e.g., Venemans et al. 2007). The strength of the overdensities are also used to characterize the structures (e.g., Steidel et al. 1998; Venemans et al. 2005; Venemans et al. 2007). Assuming the imprints from the cosmological simulations, we can compare the structures with the similar rareness at given redshifts. Note that these procedures still suffer from the observational restrictions. Then, to date, we can only obtain rough estimate of the dynamical masses of the protoclusters at $z > 2$ and it is difficult to

perform robust comparison of them with similar stellar mass. But at least, we can show the deviation of the structures from the general field and characterize some very distinct structures.

The SSA22 protocluster is well characterized as very rare density peak of the LAEs at $z = 3.09$ and is very plausible to evolve into one of the most massive clusters of galaxies in the current universe (Yamada et al. 2012). We can investigate how massive early-type galaxies were formed at $z = 3$ in most massive clusters by studying the SSA22 protocluster.

3. THE SSA22 PROTOCLUSTER

The SSA22 protocluster at $z = 3.09$ is known as one of the most outstanding structures. This protocluster was first discovered as a redshift spike of LBGs (Steidel et al. 1998) and then confirmed through the identification of a concentration of LAEs at $z = 3.09$ (Steidel et al. 2000; Hayashino et al. 2004; Yamada et al. 2012). The density excess of the LAEs at $z = 3.09$ in the SSA22 field is $\sim$15 times higher than that expected from mass fluctuations at ~ 50 Mpc scales (Yamada et al. 2012) and the rareness probability (i.e., the probability to find such a rare overdensity) at 10 Mpc scale was found to be 0.0017% (Mawatari et al. 2012). Thus, the SSA22 protocluster is well characterized as a very significant density peak of galaxies at $z = 3.09$, which may be a progenitor of one of the most massive structures in the current universe.

It is also reported that there are overdensities of Lyα Blobs at $z = 3.0$) (LABs, Matsuda et al. 2004) and ASTE/AzTEC 1.1 mm sources (Tamura et al. 2009; 2010; Umehata et al. submitted). LABs are extended Lyα nebulae in which active star-formation may occur. ASTE/AzTEC sub-mm sources indicate the dusty starburst with SFR ~ 1000 $M_{\odot}yr^{-1}$ in the protocluster. The overdensity of active galactic nuclei (AGN) among the LBGs and LAEs in the SSA22 protocluster are also reported (Lehmer et al. 2009a; 2009b), suggesting the presence of more massive galaxies and/or enhanced AGN activities in such high density region.

In order to study how stellar mass builds up in the protocluster, observations that probe rest-frame optical wavelength are essential. Uchimoto et al. (2012) (here after U12) conducted deep and wide-field near-infrared (NIR) observations of the SSA22 protocluster using the Subaru 8.2 m telescope equipped with the Multi-Objects InfraRed Camera and Spectrograph (MOIRCS). They observed galaxies to a magnitude limit of $K_{\rm AB} = 24$ over a 111.8 arcmin^2 area around the LAE density peak. They selected protocluster galaxy candidates using photometric redshifts and simple color criteria appropriate for DRGs and HEROs. Through these selection criteria, they found that there is a significant surface number density excess of these stellar mass selected galaxies compared to those in blank fields.

Another notable discovery by Uchimoto et al. (2012) was the detection of "multiple merging galaxies" associated with the LABs and an ASTE/AzTEC sub-mm source. They found that multiple sub-components with $z_{\rm phot} \approx 3.1$ are clustered with separations up to $20''$ ($\approx$150 kpc at $z = 3.09$) within extended Lyα halos of LABs or within the beam size of the ASTE/AzTEC. This suggested that star formation is actively occurring in each sub-component before these systems undergo mergers that subsequently lead to the formation of massive galaxies. High-resolution cosmological numerical simulations show that such phenomena are indeed expected in the early phase of the formation of massive early-type galaxies (e.g., Meza et al. 2003; Naab et al. 2007).

4. **THIS STUDY**

From these above, to study the formation history of the massive early-type galaxies, it is very important to study the properties of the red galaxies in the protocluster, which are plausible progenitors of massive early-type galaxies in the current universe. The protoclusters which are well characterized as very rare peaks are suitable for the purpose since they are very plausible progenitors of most massive clusters in the current universe. The SSA22 protocluster is very suitable target for the purpose.

The early-phase of the formation history of massive early-type galaxies are also important, which are predicted to be multiple mergers of the stellar components in the cosmological numerical simulations.

This paper organized with two parts. First we study the formation of massive galaxies in the SSA22 protocluster at $z = 3$ by using the NIR deep imaging and spectroscopic data. Next, we study the multiple merging galaxies identified in the SSA22 protocluster.

Chap.2. The massive galaxy formation in the SSA22 protocluster

1. THE NIR IMAGING OF THE SSA22 PROTOCLUSTER AT Z ≈ 3.09

First, we study the SSA22 protocluster by using the NIR deep and wide imaging data taken with Subaru MOIRCS and also multi-wavelength imaging data (Kubo et al. 2013, here after K13). In this section, we review the results of K13. In this paper, we assume cosmological parameters of $H_0 = 70$ km s^{-1} Mpc^{-1}, $\Omega_M = 0.3$ and $\Omega_\Lambda = 0.7$. $E(B-V) = 0.08$ is used for the Galactic extinction in the SSA22 field following Yamada et al. (2012). We use the AB magnitude system throughout this paper.

1.1. Data description and reduction

1.1.1. *Description of the data*

The data used in this study are summarized in Table 1. There are only a few protoclusters with such multi-wavelength and deep imaging data, which allow us to study the stellar populations of the galaxies in detail.

The JHK_s-band images were obtained by using Subaru MOIRCS (U12). The area observed with MOIRCS is located in the SSA22-Sb1 field (Matsuda et al. 2004), which covers the highest density region of the LAEs at $z \approx 3.09$ (Hayashino et al. 2004; Yamada et al. 2012). In total, 111.8 arcmin^2 area of the sky was observed. The data was calibrated to the UKIRT JHK-band photometric system (Tokunaga et al. 2002). A detailed description of the data and the reduction procedures are described in Uchimoto et al. (2008) and U12. Briefly, the limiting magnitude in the K-band is $K = 24.1$ (5σ detection limit for a $1''.1$ diameter aperture). The full width at half maximum (FWHM) of the point spread function (PSF) in the K-band is $\sim 0''.5$. The sizes of PSF in J-band are similar to those in K-band, and are $0''.5$ to $0''.7$. Aperture photometry was performed using the PHOT task in IRAF.

Source detections were performed on the K-band images using SExtractor (Bertin & Arnouts 1996). Objects with 16 continuous pixels above 1.5σ of the background fluctuation were extracted. We use MAG_AUTO of SExtractor as the pseudo total magnitudes of the objects. Hereafter, this paper is focused on the sample of the K-band selected galaxies with $K_{\rm AUTO} < 24$.

To supplement the K-band data, we use the $u^\star$-band archival image taken by CFHT MegaCam (P. I. Cowie, see also Matsuda et al. 2004), the $BVRi'z'$ and the $NB497$-band images taken by Subaru Suprime-Cam (Matsuda et al. 2004; Hayashino et al. 2004) and the 3.6μm, 4.5μm, 5.8μm and 8.0μm-band images by *Spitzer* IRAC (Webb et al. 2009). The entire field observed with MOIRCS is covered by the optical and the IRAC images. $NB497$ is a narrow-band filter with the central wavelength of 4977Å, which is used to detect Lyα emission from galaxies at $z = 3.061 - 3.125$. All the optical images are smoothed so that the PSF sizes are matched to be $1''.0$ in FWHM. The PSF sizes of the IRAC images are $\sim 1''.7$, slightly depending on the wavelength. Hereafter, IRAC 3.6μm-band AB magnitudes

are quoted using the [3.6μm] notation; we apply the same corresponding notations to the 4.5, 5.8, and 8.0μm bands.

We also made use of the *Spitzer* MIPS 24 μm data (Webb et al. 2009) and the point source catalog of *Chandra* 0.5-8 keV data (Lehmer et al. 2009a).

The MOIRCS field is almost entirely covered by the 24 μm data except for ~ 4 arcmin^2 region at the north-west edge of the M5 (the west edge FoV, see in U12) field. The *Chandra* data covers the entire MOIRCS field except for the M5 region. We therefore study the X-ray properties of galaxies in the available 99.8 arcmin^2 overlapping area. The nominal limiting fluxes are $\approx 6 \times 10^{-16}$ erg cm^{-2} s^{-1} in the full-band (0.5-8 keV), $\approx 2 \times 10^{-16}$ erg cm^{-2} s^{-1} in the soft-band (0.5-2 keV) and $\approx 1 \times 10^{-15}$ erg cm^{-2} s^{-1} in the hard-band (2-8 keV), respectively. The *HST* images cover only a few patchy regions, less than 10 arcmin^2 total area (for $F160W$-band), but are useful to see the structural properties of some interesting objects.

1.1.2. *Optical and NIR photometry*

We use photometric redshifts obtained from SED fitting to select protocluster galaxy candidates. For this purpose, we use the flux of the objects in $u^\star BVRi'z'JHK$ and IRAC 3.6μm, 4.5μm, 5.8μm and 8.0μm bands after correcting for the effects of different PSF sizes. The flux in the optical $u^\star BVRi'z'$ bands is measured using a 2$''$.0-diameter circular aperture. We smoothed the JHK band images to have the PSF sizes of 1$''$.0 and then obtain 2$''$.0-diameter aperture fluxes. Since the IRAC images have large PSF sizes ($\sim 1''.7$ diameter), we first obtain 3$''$.0-diameter fluxes and then apply aperture corrections. To obtain the aperture correction factors for each object, we smoothed the K-band images to have the PSF sizes of 1$''$.0 and 1$''$.7 to be matched with the optical and the IRAC images, respectively. For each object, the ratio of the fluxes within a 2$''$.0-diameter aperture on the former image to the flux within a 3$''$.0-diameter aperture on the latter image was measured to obtain the correction factor.

We also use $J-K$, $i'-K$ and $K-$[4.5μm] colors of the galaxies in our analyses. The $J-K$ colors are measured from 1$''$.1-diameter apertures after the J and K images are smoothed so that their PSF sizes are matched with each other. If objects are not detected in J-band above 2σ threshold, we use the 2σ values for upper limits. The $i'-K$ colors are the same as those obtained for SED fitting (see description of photometry above). To obtain $K-[4.5\mu\mathrm{m}]$ colors, we measured the 3$''$.0-diameter aperture flux on the IRAC images and then corrected them to the 1$''$.1-diameter aperture values. The aperture correction factor is the ratio of the 1$''$.1-aperture flux on the original K-band images to the 3$''$.0-aperture flux on the smoothed K-band image.

1.1.3. *MIPS 24 μm photometry*

Since the PSF size of the 24 μm image is relatively large ($\sim 6.0''$), source confusion is very significant. Therefore, we obtained 24 μm fluxes using the PSF fitting method described in Le Floc'h et al. (2005), which makes use of the DAOPHOT package in IRAF (Stetson 1987). The procedure starts by fitting a template PSF, derived using bright sources, to all the sources in the image. Next, source fluxes are estimated by subtracting the contributions from blended sources. For this task, we used the positions of objects detected in the K-band

images as a prior. Fluxes were obtained using 6″.0-diameter apertures, which were aperture corrected using the PSFs derived from isolated bright sources.

Due to the inhomogeneous exposure time over the observed field, the noise level of the 24 μm image varies by position. The background noise level expected for a 6″.0 diameter aperture was estimated within 80″$\times$ 80″ square regions surrounding each source. The limiting total flux (3σ) is $\approx$ 40–100 μJy. We use the conservative nominal detection limit of $f_{24\mu\mathrm{m}} =$ 100 μJy in investigating their sky distribution and their surface number density.

TABLE 1
Data set

Band	Instrument	Reference	Depth
J	MOIRCS/Subaru	Uchimoto et al. (2012)	24.1-24.5[a]
H	MOIRCS/Subaru	Uchimoto et al. (2012)	23.6-24.0[a]
K	MOIRCS/Subaru	Uchimoto et al. (2012)	24.5-25.0[a]
$u^\star$	MegaCam/CFHT	-[b]	26.1[c]
B	Suprime-Cam/Subaru	Matsuda et al. (2004)	26.45[c]
V	Suprime-Cam/Subaru	Matsuda et al. (2004)	26.5[c]
R	Suprime-Cam/Subaru	Matsuda et al. (2004)	26.6[c]
$NB497$	Suprime-Cam/Subaru	Matsuda et al. (2004)	26.2[c]
i'	Suprime-Cam/Subaru	Hayashino et al. (2004)	26.2[c]
z'	Suprime-Cam/Subaru	Hayashino et al. (2004)	25.5[c]
3.6μm	IRAC/*Spitzer*	Webb et al. (2009)	24.1[d]
4.5μm	IRAC/*Spitzer*	Webb et al. (2009)	23.9[d]
5.8μm	IRAC/*Spitzer*	Webb et al. (2009)	22.5[d]
8.0μm	IRAC/*Spitzer*	Webb et al. (2009)	22.1[d]
24 μm	MIPS/*Spitzer*	Webb et al. (2009)	40-100μJy[e]
0.5-8keV	*Chandra*	Lehmer et al. (2009a)	$\approx 6 \times 10^{-16}$ erg cm^{-2} s^{-1}[f]
0.5-2keV	*Chandra*	Lehmer et al. (2009a)	$\approx 2 \times 10^{-16}$ erg cm^{-2} s^{-1}[f]
2-8keV	*Chandra*	Lehmer et al. (2009a)	$\approx 1 \times 10^{-15}$ erg cm^{-2} s^{-1}[f]
$F160W$	WFC3/*HST*	-[g]	26.7[h]

[a] 5σ detection limiting magnitude in 1.1″ diameter aperture.
[b] P. I. Cowie (in CFHT archive)
[c] 5σ detection limiting magnitude in 2.0″ diameter aperture on the images smoothed so that the PSF sizes are matched to be 1.0″ in FWHM.
[d] 5σ detection limiting magnitude corrected to the flux in 1.1″ diameter aperture on the images with the PSF sizes of 0.5″. Here, we adopt the average aperture correction factor of the relatively isolated sources.
[e] 3σ detection limit of the total flux in the 107.8 arcmin^2 field also observed with MOIRCS.
[f] The nominal detection limit in the 99.8 arcmin^2 field also observed with MOIRCS
[g] P. I. Siana, Proposal ID; 11636 (in *HST* archive)
[h] 5σ detection limiting magnitude in 0.6″ diameter aperture

1.2. The selection of the candidate protocluster galaxies

We first selected the candidate protocluster galaxies based on the photometric redshifts to study the properties of the galaxies in the SSA22 protocluster.

We detect the objects on the K-band images ($K_{\rm AUTO} < 24$, here after we call K-selected) and estimated the photometric redshifts. The photometric redshifts are estimated based on the spectral energy distribution (SED) fitting of the observed flux values with the model SEDs. We use the fluxes of the objects in $u^{\star}BVRi'z'JHK$, 3.6μm, 4.5μm, 5.8μm and 8.0μm bands after aperture correction. The detailed procedures of the SED fitting are described in the §2.3. in this Chapter. Note that Salpeter Initial Mass Function (IMF) (Salpeter 1955) is used for the study with the imaging data (§1 in this Chapter) while Chabrier IMF (Chabrier 2003) is used for the study with the NIR spectroscopy (From §2 in this Chapter to the end of the paper), since Chabrier IMF are adopted in the comparison sample for NIR spectroscopy. It is reported in Erb et al. (2006a) that the stellar mass obtained adopting Salpeter IMF is 1.8 times larger than that obtained with Chabrier IMF.

Here we briefly describe the accuracy of our photometric redshifts. Figure 1 is the comparison of the photometric redshifts and spectroscopic redshifts of the K-selected galaxies obtained by our study. The spectroscopic redshifts cited here are obtained from NASA IPAC Extragalactic Database (NED). The bottom panel of Figure 1 shows the relative errors of the photometric redshifts, $\Delta z/(1+z_{\rm spec})$ where $\Delta z = (z_{\rm spec} - z_{\rm phot})$. The standard deviation is $< \Delta z/(1+z_{\rm spec}) >= 0.08$, excluding the galaxies with $|\Delta z|/(1+z_{\rm spec}) > 0.5$. For galaxies at $z_{\rm spec} = 3.02 - 3.16$, $< \Delta z/(1+z_{\rm spec}) >$ is 0.07. The median photometric redshift of the protocluster galaxies is $z_{\rm phot} = 3.06$, which agrees well with that of the spectroscopic sample. The accuracy of our photometric redshifts is comparable to those obtained in other surveys with similar data-sets (e.g., GOODS-North field, Ichikawa et al. 2007). We use the spectroscopic redshift if available (here after we call $z_{\rm best}$).

Then we select the K-selected galaxies with $2.6 < z_{\rm best} < 3.6$ as the candidate protocluster galaxies. Figure 2 is the sky distribution of the K-selected galaxies at $2.6 < z_{\rm best} < 3.6$.

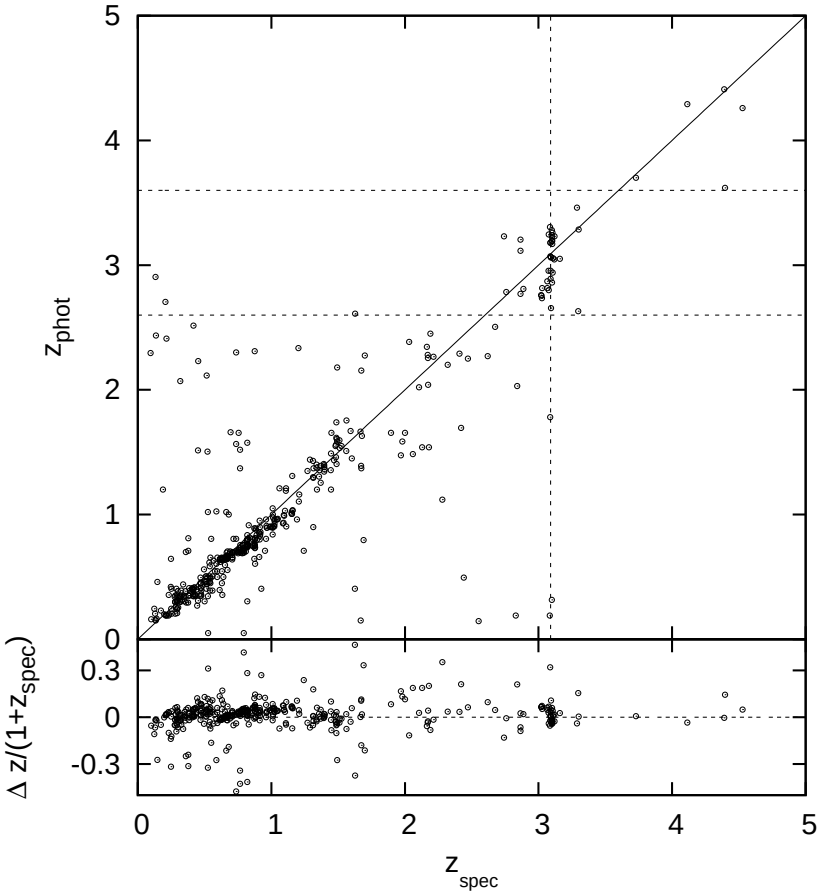

FIG. 1.— *Top*; The comparison between the spectroscopic redshifts available in the NASA/IPAC Extragalactic Database and our photometric redshifts of the K-selected galaxies in the SSA22 field. The vertical dashed line shows the median redshift of the protocluster. The horizontal dashed lines are drawn at $z_{\rm phot} = 2.6$ and $z_{\rm phot} = 3.6$. We plot the relative errors of the photometric redshifts $\Delta z/(1 + z_{\rm spec})$ where $\Delta z = (z_{\rm spec} - z_{\rm phot})$ in the *bottom* panel.

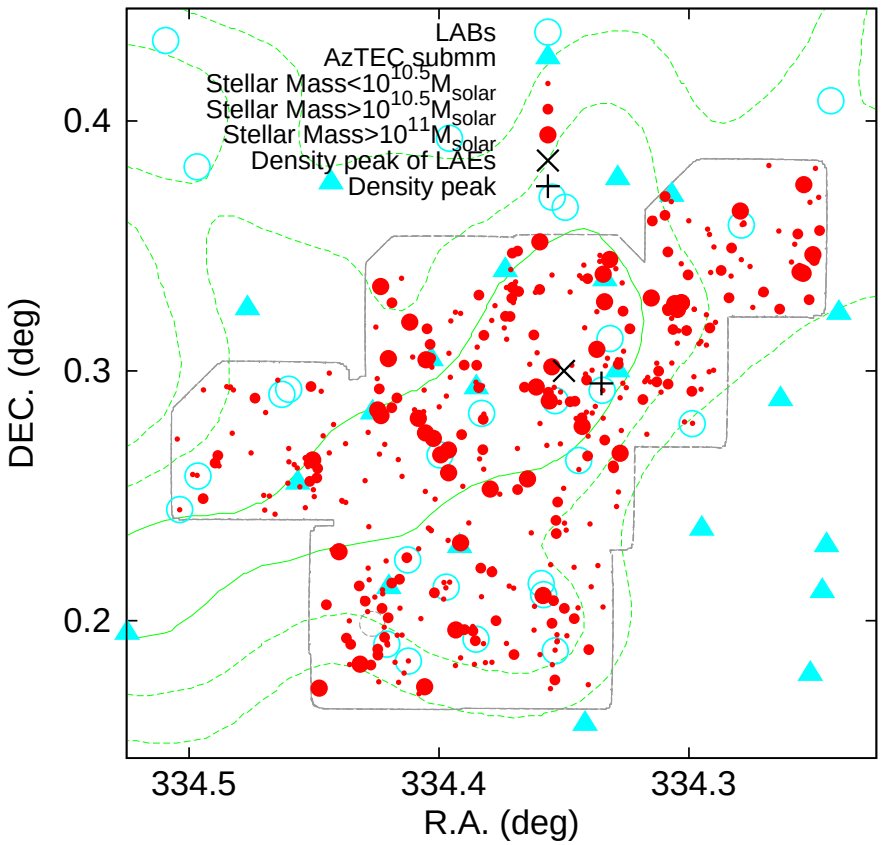

FIG. 2.— The sky distribution of the objects with $K_{\rm AB} < 24$ at $2.6 < z_{\rm phot} < 3.6$ in the SSA22 field (red filled circles). The region enclosed with Gray line is the field observed with JHK-bands. The size of the circles indicates the stellar mass of the galaxies. The black cross is the density peak of them and x-mark is that of the LAEs at $z = 3.09$. The LABs (cyan circles), ASTE/AZTEC sub-mm sources (cyan triangles) and the density contour of the LAEs (green lines) are plotted.

1.3. The density excess of the K-selected protocluster galaxies

In the left panel of Figure 3, we show the cumulative surface number density of the K-selected galaxies at $2.6 < z_{\rm best} < 3.6$ in the entire SSA22 field. The error bar in each bin corresponds to the 1σ Poisson error. For comparison, we also plot the redshift distribution of the K-selected GOODS-N galaxies from the MOIRCS Deep Survey (MODS) catalog (Kajisawa et al. 2006) with $K < 25.1$ (5σ detection limit) in a 103.3 arcmin^2 area, and $< \Delta z/(1+z_{\rm spec}) > \sim 0.12$ for the whole sample. The surface number density of the galaxies with $K < 24$ in the SSA22 field is 3.87 ± 0.19 arcmin^{-2}, which is 1.7 times of that in GOODS-N. If we subtract the contribution of field galaxies (based on GOODS-N) from the SSA22 number counts, we estimate that there is an excess of ≈ 180 K-selected galaxies, potentially sources that are members of the protocluster.

We identified the position of the large-scale density peak of the K-selected galaxies at $2.6 < z_{\rm best} < 3.6$ on the sky by smoothing their distribution with a Gaussian kernel of scale $\sigma = 0.5$ arcmin. We found the location of the peak at (α, δ) $\approx$ ($22{\rm h}17^{\rm m}20^{\rm s}$, $+00°17.'7$), which is indicated in Figure 2. Interestingly, the location of the peak is within 1 arcmin of the peak of the $z = 3.09$ LAE distribution, which was obtained using a smoothing scale of 1.5 arcmin in Yamada et al. (2012) (The smoothing scales differ in their and our studies since the FoV of our study is too small to use similar smoothing scale.). The density peak of the simple color-selected DRGs was also found to be near that of the protocluster LAEs (Uchimoto et al. 2012). The right panel of Figure 3 is the cumulative surface number density of the K-selected galaxies at $2.6 < z_{\rm best} < 3.6$ within 1.5 Mpc radius around the density peak. We find the density of $K < 24$ galaxies in this region of SSA22 to be 2.1 times of that found in the GOODS-N field.

The surface number density of the DRGs at $2.6 < z_{\rm best} < 3.6$ is 2.5 times higher than that of the galaxies selected based on the photometric redshifts in GOODS-N. This excess increases to a factor of 2.7 near the K-selected source density peak. Overdensities of red galaxies in protoclusters at $z \sim 2$ have also been found in other studies (e.g., Kodama et al. 2007; Zirm et al. 2007; Doherty et al. 2010). On the other hand, no significant density excesses of the DRG-like objects were observed in some protoclusters at $z \sim 3$, including MRC 0943-242 at $z = 2.93$ (Doherty et al. 2010) and MRCS0316-257 at $z = 3.13$ (Kuiper et al. 2010; based on Balmer-break selection of galaxies with colors similar DRGs). Kuiper et al. (2010) noted that it is difficult to detect the surface number density excess of DRGs with their sample due to limited area and depth. We note that our NIR data in the SSA22 field is wider and deeper than those used by Doherty et al. (2010) and Kuiper et al. (2010). As we show from the NIR spectroscopy in later, notable fraction of the DRGs in the SSA22 field are actually at $z_{\rm spec} \approx 3.09$, which support that there is certainly a density excess of the DRGs in the SSA22 protocluster.

We summarise the surface number density and density excess of some unique objects in Table 3.2.4. There are more significant surface number density excess of the 24 μm sources, X-ray sources and quiescent galaxies (selected based on rest-frame UV-NIR colors, described in later) at $z_{\rm phot} \sim 3.1$ than the K-selected galaxies only selected by $z_{\rm phot}$. There is also significant density excess of the K-band luminous LAEs.

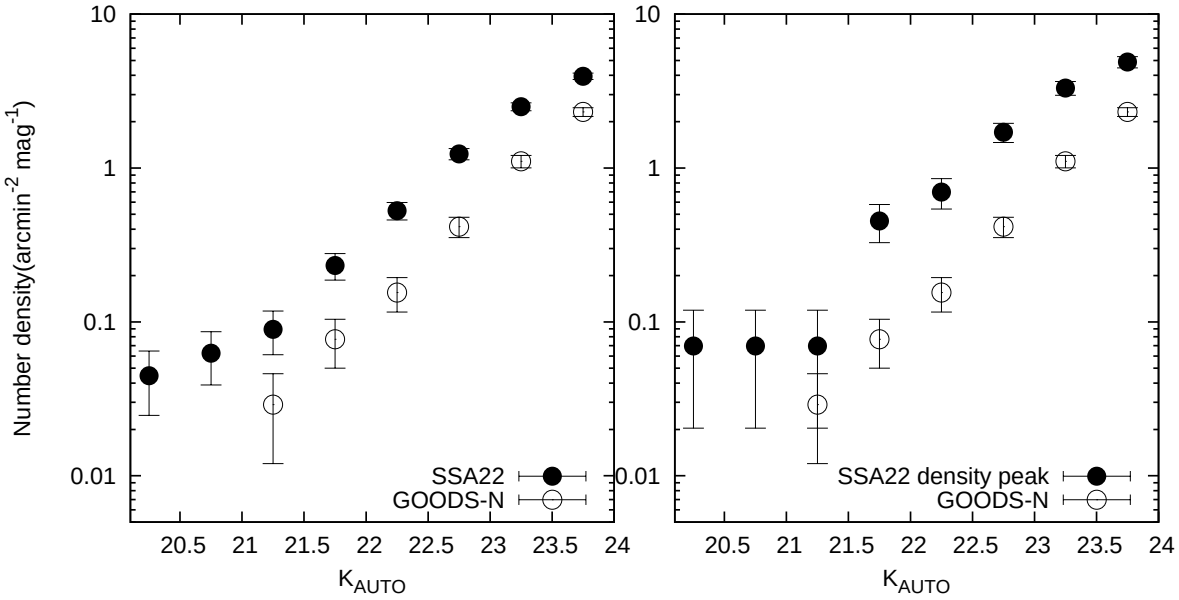

FIG. 3.— *Left*; The cumulative surface number density of the K-selected galaxies at $2.6 < z_{\rm best} < 3.6$. The black filled circles are that in the entire SSA22 field and the black open circles are that in the GOODS-North field. *Right*; Similar to the left panel but the black filled circles are the cumulative surface number density at the SSA22 highest density region.

TABLE 2
NUMBER COUNTS OF THE CHARACTERISTIC K-SELECTED GALAXIES AT $2.6 < z_{\rm best} < 3.6$

Classification	$N_{\rm obj}$[a]	Number density (arcmin^{-2})	Ratio[b] (SSA22 / field)
$K < 24$	433(49)	3.87±0.19	1.7±0.1
$M_{\rm star} > 10^{11}\ M_\odot$	43(11)	0.38±0.06	1.8±0.5
$10^{10.5}\ M_\odot < M_{\rm star} < 10^{11}\ M_\odot$	116(7)	1.03±0.10	1.6±0.2
$M_{\rm star} < 10^{10.5}\ M_\odot$	274(31)	2.45±0.15	1.7±0.2
Quiescent galaxies	11(1)	0.10±0.03	- [c]
$24\mu m (f_{24\mu\rm m} > 40\ \mu$Jy)	31(5)	0.29±0.05	-
$24\mu m$ detected ($f_{24\mu\rm m} > 100\ \mu$Jy)	22(3)	0.20±0.04	1.9±0.7
Chandra full-band ($f_{0.5-8\rm keV}$ >6×10^{-16} erg cm^{-2} s^{-1})	19(10)	0.19±0.04	2.5±1.0
Chandra soft-band ($f_{0.5-2\rm keV}$ >2×10^{-16} erg cm^{-2} s^{-1})	14(8)	0.14±0.04	2.4±1.2
Chandra hard-band ($f_{2-8\rm keV}$ >1×10^{-15} erg cm^{-2} s^{-1})	13(8)	0.13±0.04	3.4±1.9
LAEs	9(5)	0.08±0.03	6.8±2.3[d]

[a]Number of the K-selected galaxies at $2.6 < z_{\rm best} < 3.6$ ($2.6 < z_{\rm spec} < 3.6$).
[b]Ratio of the surface number density in the SSA22 protocluster to that in the general field. All the samples but LAEs are compared with those in the MOIRCS Deep Survey in GOODS-N field (Kajisawa et al. 2011). The LAEs are compared with those in SXDS field (Ouchi et al. 2008; Ono et al. 2010).
[c]None of the K-selected galaxies at $2.6 < z_{\rm best} < 3.6$ in GOODS-N field satisfy the color criterion of the quiescent galaxies.
[d]Ratio of K-band detection rate of the LAEs in SSA22 and in SXDS field.

1.4. The stellar population of the K-selected protocluster galaxies

Figure 4 displays the $i'-K$ versus $K-[4.5\mu\mathrm{m}]$ color-color diagram for K-selected galaxies with $2.6 < z_{\mathrm{best}} < 3.6$ in the SSA22 and GOODS-N fields. This diagram has been used in previous studies to distinguish between star-forming and quiescent galaxies at $z > 2$. For example, Labbé et al. (2005) and Papovich et al. (2006) studied $z > 2$ DRGs in the Hubble Deep Field-South (HDF-S) and GOODS-South field, respectively. For the SSA22 sample, we show the 268 K-selected galaxies at $2.6 < z_{\mathrm{best}} < 3.6$ that are detected in the 4.5μm and do not suffer from source blending with nearby sources. The detection limit at 4.5μm after applying aperture corrections is ≈ 23.9 (5σ limit).

We classified galaxies by comparing their $i' - K$ versus $K - [4.5\mu\mathrm{m}]$ colors with simple synthetic models. We classified galaxies with $i' - K > 3.0$ & $K - [4.5\mu\mathrm{m}] < 0.5$ as quiescent galaxies, since these colors are consistent with those expected for galaxies with single-burst ages > 0.5 Gyr. Galaxies with $K - [4.5\mu\mathrm{m}] > 0.5$ were classified as heavily dust obscured starburst galaxies, since these colors are consistent with those expected for galaxies with constant continuous star formation history with $E(B-V) \sim 1$. Finally, the star-forming galaxies with moderate dust obscuration are expected to distribute throughout the region with $i' - K < 3.0$ and $K - [4.5\mu\mathrm{m}] < 0.5$. We indicate the DRGs and LBGs (Steidel et al. 2000) in Figure 4. Note that it is more appropriate to take the color cut line in Figure 4 drawn at a slat to select the quiescent galaxies exhaustively. But we set this color selection to avoid the contamination of dusty starburst galaxies.

The DRGs span a wide range of colors and dominate the population of the reddest galaxies in $i' - K$. On the other hand, LBGs are typically blue in $i' - K$ and correspond to star-forming galaxies with moderate extinction. There are some very red objects in $K - [4.5\mu\mathrm{m}] \gtrsim 1.5$ which could be AGNs with power-law spectra in the NIR (e.g., Daddi et al. 2007; Yamada et al. 2009).

We carefully checked the observed SEDs of the quiescent galaxy candidates, since their red colors could be due to the presence of strong $[\mathrm{O_{III}}]\lambda\lambda5007$ emission lines. Indeed 4 out of the 15 candidates show clear excesses in the K-band only; they are typically ~ 0.3 mag redder in $H-K$ and ~ 0.4 mag bluer in $K-[3.6\mu\mathrm{m}]$ than the average colors of the remaining 11 objects. All of these 4 galaxies are fainter than $K = 23$. It is also found from the NIR spectroscopic observations described in later that the contributions of $[\mathrm{O_{III}}]\lambda\lambda5007$ emission lines to K-band flux values are negligible. The SEDs of the remaining 11 objects, on the other hand, are well fitted by the models of quiescent galaxies with ages of 0.5–2 Gyr at $z = 3.1$. If we consider only galaxies with $K < 23$, we find a corresponding $2.6 < z_{\mathrm{best}} < 3.6$ quiescent galaxy surface density of 0.10 ± 0.03 arcmin^{-2} in SSA22. All of these quiescent galaxies satisfy the DRG color selection criterion in $J - K$, suggesting the presence of significant Balmer or 4000 Å breaks. On the other hand, $\approx 20\%$ of the DRGs with $K < 23$ at $2.6 < z_{\mathrm{best}} < 3.6$ in SSA22 lie in the color range of quiescent galaxies.

There is one quiescent galaxy that is detected in 24 μm. However, the SED of this object is also well fitted by a model of passive evolution with an age of 1.7 Gyr at $z \approx 3.09$, with a slight excess over the model at $> 5.8\mu$m. The observed light at wavelengths shorter than 4.5μm is dominated by the old stellar component, while the mid-infrared emission maybe due to dust heated by an AGN. For the remaining 10 objects without 24 μm detections, we stacked their 24 μm images and found no significant stacked detection. The corresponding

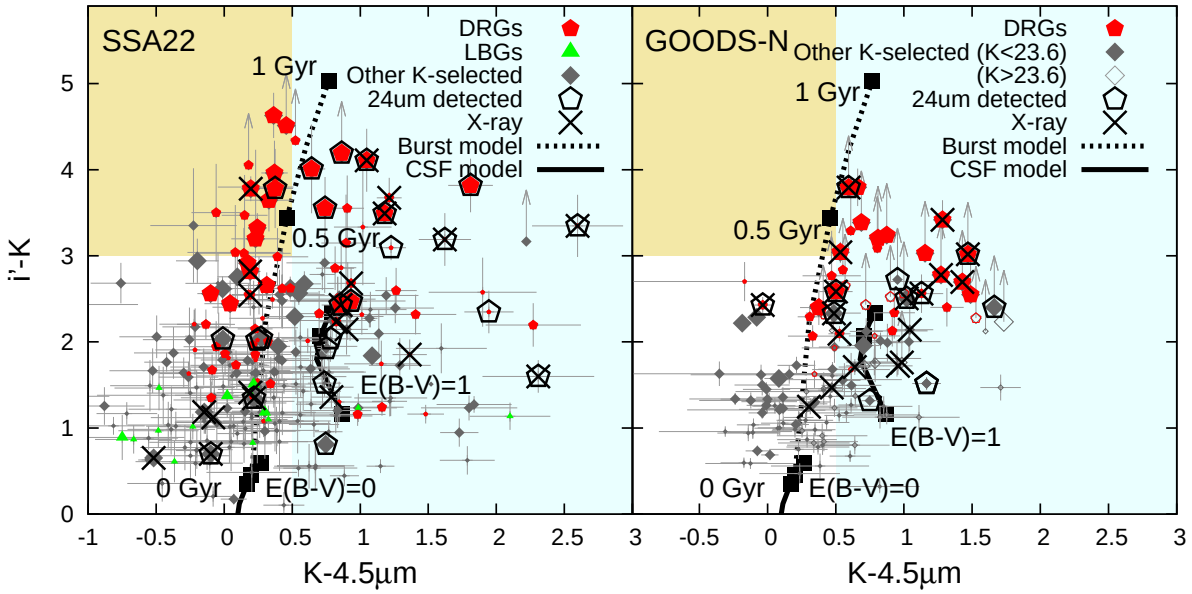

FIG. 4.— $i' - K$ versus $K - [4.5\mu\mathrm{m}]$ two color diagram of the K-selected galaxies at $2.6 < z_{\mathrm{best}} < 3.6$ in the SSA22 (left) and GOODS-N (right) field. The gray filled diamonds are all the K-selected galaxies which are also detected in $[4.5\mu\mathrm{m}]$. The size of the symbols reflects the stellar masses of the objects classified as $M_{\mathrm{star}} < 10^{10.5}\ M_{\odot}$ (small), $10^{10.5}\ M_{\odot} < \mathrm{M_{star}} < 10^{11}\ M_{\odot}$ (medium) and $M_{\mathrm{star}} > 10^{11}\ M_{\odot}$ (large). The red filled pentagons and the green filled triangles are the K-selected galaxies at $2.6 < z_{\mathrm{best}} < 3.6$ classified as DRGs and LBGs, respectively. The open black pentagons are the galaxies detected in 24 μm and the black crosses are those detected in *Chandra* full- and/or soft- and/or hard-bands. The black dotted line and square points are the color evolution track with age for single burst star formation model at $z = 3.1$. The square points are at 0, 0.5, 1.0 Gyr from bottom to top. The black solid lines and square points are those for constant continuous star formation model with $E(B-V) = 0$ (0 Gyr point is out of the range of the figure) and 1. We classified the galaxies at the region filled with yellow as the 'quiescent galaxies' ($i' - K > 3.0$ & $K - [4.5\mu\mathrm{m}] < 0.5$), at the region filled with light cyan as the 'dusty starburst galaxies' ($K - [4.5\mu\mathrm{m}] > 0.5$) and non-colored region as the 'normal star-forming galaxies' ($i' - K < 3$ and $K - [4.5\mu\mathrm{m}] < 0.5$). In the GOODS-N field, $F775W$-band of *HST* ACS with the detection limit of $i_{775} = 25.6$ (5σ limit) is used. Therefore we plot the galaxies fainter than $K_{\mathrm{AUTO}} = 23.6$ with open symbols in GOODS-N.

upper limit of the 24 μm flux for the stacked sources is 17 μJy (2σ).

The stellar masses of the quiescent galaxies span the range of $10^{10.8-11.7}\ M_{\odot}$, comparable to those of local massive early-type galaxies. On the other hand, $\approx 20\%$ (9/43) of the K-selected galaxies with stellar mass $> 10^{11}\ M_{\odot}$ at $2.6 < z_{\mathrm{best}} < 3.6$ in SSA22 are classified as the quiescent sources.

The presence of these quiescent galaxies in the SSA22 field is conspicuous. With the same color criterion and detection limits, we found *no* such quiescent galaxies at $2.6 < z_{\mathrm{best}} < 3.6$ in the MODS GOODS-N sample. Furthermore, few DRGs in GOODS-S field satisfy our selection criterion for quiescent galaxies (Papovich et al. 2006) despite having a broader redshift range for selection. If we correct the number of the foreground/background galaxies adopting the 1.8 times density excess of the protocluster field (Table 3.2.4), the fraction of the quiescent galaxies among the K-band selected galaxies with stellar mass $> 10^{11}\ M_{\odot}$ is expected to be at most $\approx 50\%$ (i.e., 9/19).

1.5. The density enhancement of the X-ray sources

We plot the K-band magnitudes versus the X-ray flux of the K-selected galaxies at $2.6 < z_{\rm best} < 3.6$ in Figure 5. In the GOODS-N field, there are only a few objects brighter than the nominal detection limits for the *Chandra* observations in SSA22. About half of the X-ray detected objects in SSA22 are also detected at 24 μm (> 100 μJy). The AGNs in the SSA22 protocluster seem to be more powerful and more dust attenuated than those in the general field at similar redshifts. The 24 μm detection rate is largest for the hard-band sample, which is consistent with AGN having large dust attenuation in the protocluster. The more luminous X-ray objects are observed in the SSA22 protocluster, which also suggests the enhanced AGN activity.

There may be further contributions from a hidden population of dust obscured AGNs that are faint in X-ray emission. Daddi et al. (2007) investigated 24 μm sources at $z > 2$ and found that the galaxies that are more luminous than $L_{8\mu{\rm m}} > 10^{11}\ L_{\odot}$ in νL_{ν} show a statistically significant X-ray detection when stacked. In the SSA22 field, among 31 K-selected galaxies at $2.6 < z_{\rm best} < 3.6$ detected at 24 μm, we find 10 that are also detected in the X-ray band. Since the detection limit in 24 μm in the SSA22 field corresponds to $L_{6\mu{\rm m}} \sim 10^{11}\ L_{\odot}$ in νL_{ν}, it is reasonable to expect that there are additional dust obscured AGNs not detected in X-ray. Therefore, we consider the AGN hosting rate to be a lower limit.

The excess AGN hosting rate of LAEs and LBGs in the SSA22 protocluster was reported in Lehmer et al. (2009a; 2009b) and Webb et al. (2009). All the galaxies at $z_{\rm spec} \approx 3.09$ detected in X-ray listed in Table 1 of Lehmer et al. (2009a) lie in the MOIRCS observed area. All of them are also members of our K-selected sample. A similar enhancement was also reported for LAEs and BX/MD galaxies in the HS 1700+64 protocluster at $z = 2.30$ studied by Digby-North et al. (2010).

The excess AGN hosting rate of the galaxies in the SSA22 protocluster may be due to the enhanced activity of AGNs and/or the presence of more massive host galaxies in the protocluster environment. Given that supermassive black hole (SMBH) masses and their host galaxy stellar masses are tightly correlated in the local Universe (e.g., Kormendy & Richstone 1995; Magorrian et al. 1998), it is possible that the enhanced AGN hosting rate is due to the presence of more massive galaxies there. In Table 3.2.4, we tabulate the surface number density of K-selected galaxies over three stellar mass ranges. The density excess in each stellar mass bin is similar to that of the whole K-selected galaxy sample. Therefore, at least, the excess AGN hosting rate of the K-selected galaxies at $2.6 < z_{\rm best} < 3.6$ is not likely to be simply due to the presence of more massive host galaxies in the SSA22 protocluster. The hard-band X-ray detection rates are $14 \pm 6\%$ in SSA22 and $9 \pm 6\%$ in GOODS-N for K-selected galaxies with $M_{\rm star} > 10^{11}\ M_{\odot}$ and $2.6 < z_{\rm best} < 3.6$. Further observations are needed to constrain how the protocluster environment influences the AGN activities.

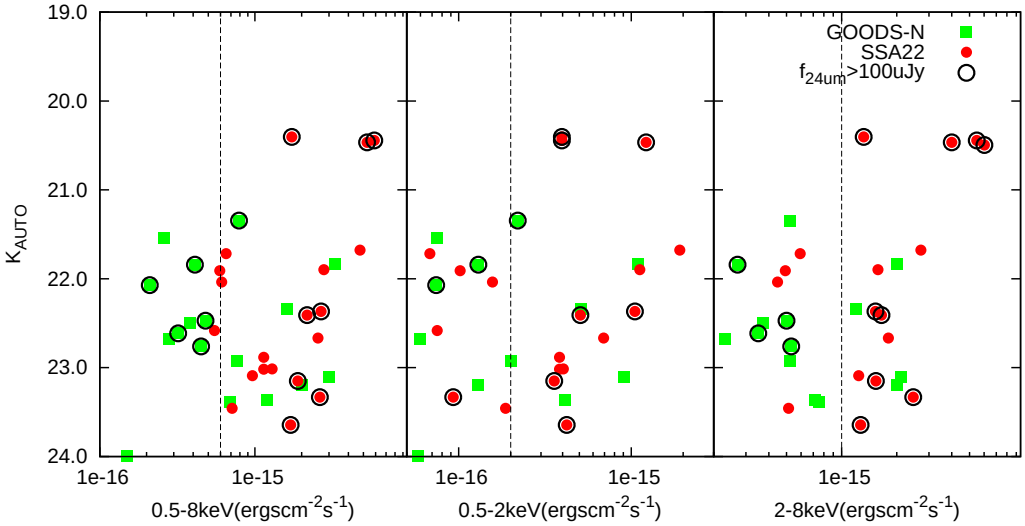

FIG. 5.— Total magnitudes in K-band versus fluxes in X-ray distributions for the K-selected galaxies at $2.6 < z_{\rm best} < 3.6$. The figures are full- (0.5-8 keV), soft- (0.5-2 keV) and hard-band (2-8 keV) from left to right. The red filled circles are the K-selected galaxies at $2.6 < z_{\rm best} < 3.6$ in 99.8 arcmin^2 of the SSA22 field. The green filled squares are the K-selected galaxies at $2.6 < z_{\rm best} < 3.6$ in 103.3 arcmin^{-2} in GOODS-N field. The black circles are the objects with $f_{24\mu{\rm m}} > 100$ μJy. The dashed lines in each panel are the nominal detection limits of *Chandra* data in the SSA22 field.

1.6. Summary of the NIR imaging observations

We identified the K-selected galaxies at $2.6 < z_{\rm best} < 3.6$ that are candidate members of the SSA22 protocluster at $z = 3.09$ using deep and wide NIR observations and photometric redshift fitting.

We found the surface number density excess of the K-selected galaxies at $2.6 < z_{\rm best} < 3.6$ in the SSA22 protocluster field over that of the general field. We also found that DRGs ($J - K < 1.4$) and 24 μm detected galaxies among the K-selected population at $2.6 < z_{\rm best} < 3.6$ show even larger surface number density excesses.

We identified 11 quiescent galaxies in our sample by using their rest-frame UV to NIR colors. No such galaxies were identified throughout the entire GOODS-N field. Such significant clustering of the quiescent galaxies at $z \approx 3$ is reported here for the first time. Additionally, we found a density excess of dusty starburst galaxies selected by the color criterion, which indicates that the SSA22 protocluster galaxies are still experiencing enhanced star formation.

There is also a density excess of K-selected galaxies at $2.6 < z_{\rm best} < 3.6$ detected in the X-ray bandpass. These sources are typically more obscured and X-ray luminous than those in the general field.

From the above, we conclude that there are already a significant fraction of evolved quiescent massive galaxies in the SSA22 protocluster. However, star-formation and also AGN activity is still ongoing and enhanced over the field. This protocluster may be at a key formation epoch of elliptical galaxy formation in a protocluster that will collapse to form a rich galaxy cluster by $z = 0$.

2. THE NEAR-INFRARED SPECTROSCOPY OF THE GALAXIES IN THE SSA22 PROTOCLUSTER

The photometric redshifts are not accurate enough to show the protocluster memberships of each individual galaxy. To obtain the accurate redshifts, we need spectroscopic follow-up observations. Spectroscopic redshifts are also useful to measure the dynamical properties of the clusters (and also those of the individual galaxies), constrain the properties of Inter Stellar Matter (ISM), perform more accurate SED fitting of each galaxy and so on.

We present the NIR spectroscopic observation of the candidates of the protocluster galaxies. Since the rest-frame optically selected candidates of the protocluster galaxies are typically faint in rest-frame UV, nebular emission lines in rest-frame optical wavelength are useful. For the galaxies at $z = 3$, $[O_{III}]\lambda5007$ is the strongest available emission line.

2.1. Sample selections and Observations

The observations are conducted with MOIRCS on Subaru Telescope during 2012 September 29-30 and October 27-28. We used Multi-Object Spectroscopy (MOS) mode on MOIRCS. The location of the slit masks and the targets are shown in Figure 6. Summary of the observations is given in Table 3.

Our targets are the candidate members of the SSA22 protocluster selected as $K < 24$ (at 5σ limit) and with $2.6 < z_{\rm phot} < 3.6$. The detailed descriptions of our photometric redshift measurements were described in § 1.2. 2.3.3 (also given in U12 and K13). We put priorities on the DRGs, HEROs, *Spitzer* MIPS 24 μm sources, *Chandra* X-ray sources and counterparts of the LABs and ASTE/AzTEC 1.1-mm sources (based on Webb et al. 2009; Lehmer et al. 2009b; Matsuda et al. 2004; Umehata et al. submitted), which we have show significant density excess by imaging studies. We use four slit masks to cover the density peak of the protocluster and also LAB01, one of the largest LABs. In total, 67 objects were observed. List of the targets is given in Table 2.1. Four objects were observed twice with different slit masks.

MOIRCS consists of two channels, Ch1 and Ch2, with each $3'.5 \times 4'.0$ field of view (FoV). We used the Volume Phase Holographic K-band grism for Ch2 (VPH-K; Ebizuka et al. 2011). The VPH-K grism is a newly developed grism for MOIRCS with $R \sim 1700$ with $0''.8$ slit width, which covers $1.9 - 2.3$ μm wavelength. We had to use $HK500$ grism for Ch1 due to the unfortunate failure of MOIRCS. $HK500$ grism is $R \sim 500$ with $0''.8$ slit width, which covers $1.3 - 2.3$ μm. Mask alignment could be only performed for Ch2 for the entire observations and Ch1 could not be used for the first two nights. The total exposure time was $2.7 - 4$ hours for each mask. The seeing size in $K_{\rm s}$ band during the observations was typically $0''.6$, ranging from $0''.4$ to $0''.8$. The telescope was dithered along the slit by $3''.0$ for sky subtraction. Flux standard stars for the VPH-K grism were taken at the end of the observations using some slits in each mask. Flux values are calibrated to their K-band total magnitudes given in Two Micron All Sky Survey point source catalog (Skrutskie et al. 2006). Since acquisitions of the known standard stars were not available for Ch1 during our observations, bright stars in the same slit masks as the targets were observed for calibration with our own MOIRCS K-band images.

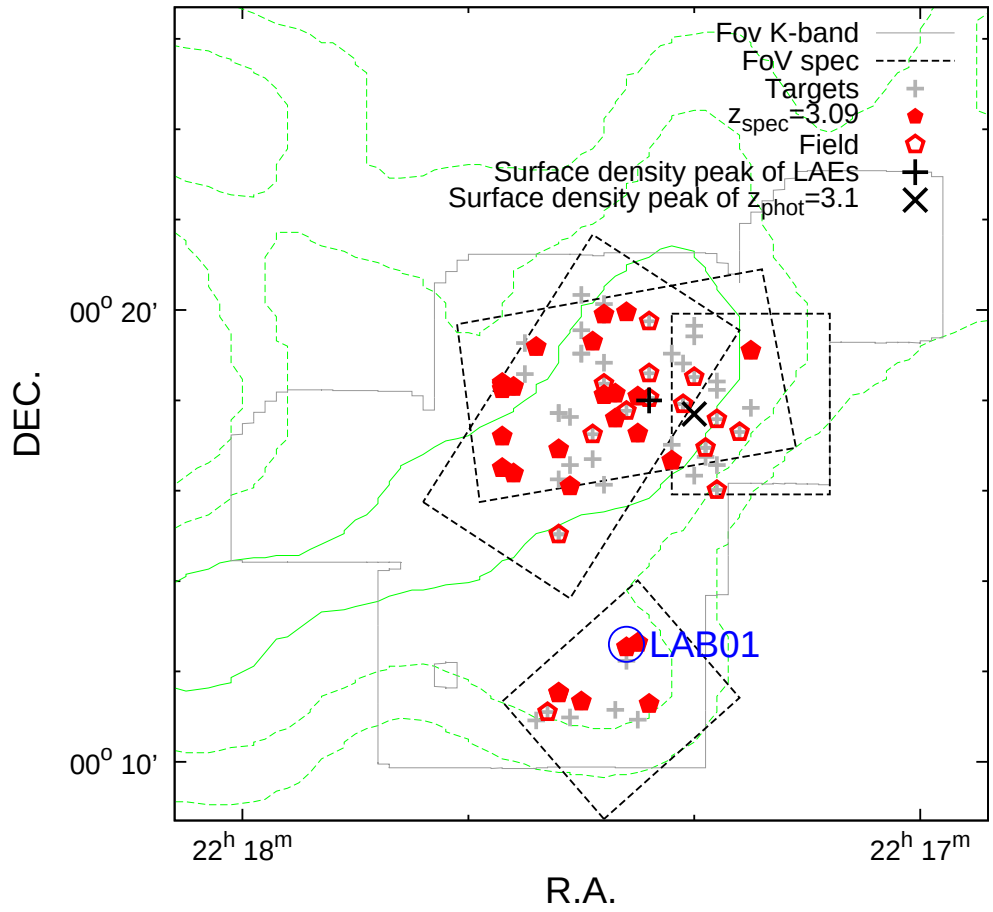

FIG. 6.— Sky coordinates of the targets in the SSA22 field. Boxes with black dashed lines show the allocation of slit masks for spectroscopy. Filled red pentagons are the objects confirmed the redshifts at $z_{\rm spec} = 3.04 - 3.12$ and blank red pentagons are those confirmed to be at $z_{\rm spec} = 2.0 - 3.4$. Gray crosses are the targets observed. Gray solid lines enclose the FoV of the MOIRCS K-band imaging observations. Green contours are the 1, 1.5 and 2σ iso-density regions of the LAEs at $z \approx 3.09$ and black large cross is the surface density peak of the LAEs at $z \approx 3.09$ (Yamada et al. 2012). Black large x-mark is that of the K-selected galaxies at $z_{\rm phot} = 2.6 - 3.6$ (K13). An blue large circle indicates the position of LAB01.

TABLE 3
SUMMARY OF THE OBSERVATION

mask ID	R.A. (J2000.0)	Dec (J2000.0)	P.A.[a] (deg)	UT date	exposure (sec)	seeing[b] (arcsec)	channel	grism	target
SSA22B	22 17 31.7	00 12 40.7	222	2012 Sep 29	14000	0.6	ch1	VPH-K	...[c]
							ch2	VPH-K	12
SSA22A1	22 17 22.6	00 17 55.1	270	2012 Sep 30	16000	0.7	ch1	VPH-K	...[c]
							ch2	VPH-K	12
SSA22D	22 17 26.8	00 18 19.4	280	2012 Oct 27	13000	0.4	ch1	$HK500$	13
							ch2	VPH-K	10
SSA22C	22 17 30.5	00 17 39.8	148	2012 Oct 28	13600	0.5	ch1	$HK500$	11
							ch2	VPH-K	13

[a]Direction of the slits, from north to east
[b]Average PSF sizes in K_s-band during the observations
[c]Ch1 did not work during the observations of September 29 and 30.

TABLE 4
List of the targets

ID	R.A. (h.m.s)	Dec (d.m.s)	K_s[a] (mag)	$J-K$[b] (mag)	grism	mask-ID	$z_{\rm lit}$[c]
J221715.97+001750.6	22 17 15.97	00 17 50.6	23.543	1.29	VPH-K	SSA22A1	...
J221718.02+001735.6	22 17 18.02	00 17 35.6	23.546	1.06	VPH-K	SSA22A1	...
J221719.39+001657.1	22 17 19.39	00 16 57.1	23.249	1.41	VPH-K	SSA22A1	...
J221718.58+001814.6	22 17 18.58	00 18 14.6	23.668	0.58	VPH-K	SSA22A1	...
J221718.27+001826.0	22 17 18.27	00 18 26.0	23.688	1.34	VPH-K	SSA22A1	...
J221716.42+001718.6	22 17 16.42	00 17 18.6	23.051	0.84	VPH-K	SSA22A1	...
J221718.49+001634.0	22 17 18.49	00 16 34.0	22.990	0.92	VPH-K	SSA22A1	...
J221720.10+001620.3	22 17 20.10	00 16 20.3	23.867	1.09	VPH-K	SSA22A1	...
J221721.01+001849.7	22 17 21.01	00 18 49.7	22.933	2.69	VPH-K	SSA22A1	...
J221715.71+00196.2	22 17 15.71	00 19 6.2	>24	...	VPH-K	SSA22A1	3.10150
J221718.61+00161.2	22 17 18.61	00 16 1.2	22.543	2.01	VPH-K	SSA22A1	...
J221719.94+001646.0	22 17 19.94	00 16 46.0	22.156	1.59	VPH-K	SSA22A1	...
J221726.10+001232.3	22 17 26.10	00 12 32.3	22.079	1.32	VPH-K	SSA22B	...
J221725.71+001238.7	22 17 25.71	00 12 38.7	23.648	0.29	VPH-K	SSA22B	...
J221724.85+001117.5	22 17 24.85	00 11 17.5	23.078	0.81	VPH-K	SSA22B	...
J221732.5+001131.2	22 17 32.52	00 11 31.2	23.416	0.38	VPH-K	SSA22B	...
J221732.5+001132.8	22 17 32.46	00 11 32.8	22.979	0.85	VPH-K	SSA22B	3.0860
J221725.12+001056.7	22 17 25.12	00 10 56.7	23.712	1.02	VPH-K	SSA22B	...
J221733.94+00116.5	22 17 33.94	00 11 6.5	22.515	0.99	VPH-K	SSA22B	...
J221734.43+001055.4	22 17 34.43	00 10 55.4	23.825	0.84	VPH-K	SSA22B	...
J221731.55+001059.6	22 17 31.55	00 10 59.6	22.947	0.13	VPH-K	SSA22B	...
J221726.27+001214.9	22 17 26.27	00 12 14.9	...	...	VPH-K	SSA22B	...
J221730.23+001120.7	22 17 30.23	00 11 20.7	20.927	0.75	VPH-K	SSA22B	...
J221727.05+00119.9	22 17 27.05	00 11 9.9	23.098	0.91	VPH-K	SSA22B	...
J221725.4+001717	22 17 25.41	00 17 16.9	21.718	2.36	$HK500$	SSA22C	3.120
					VPH-K	SSA22D	
J221720.85+001831.0	22 17 20.85	00 18 31.0	20.444	1.43	$HK500$	SSA22C	2.840
J221726.34+001957.2	22 17 26.34	00 19 57.2	23.212	1.80	$HK500$	SSA22C	...
J221730.62+001933.8	22 17 30.62	00 19 33.8	23.853	0.78	$HK500$	SSA22C	...
J221730.61+00192.1	22 17 30.61	00 19 2.1	22.750	-0.24	$HK500$	SSA22C	...
					$HK500$	SSA22D	...
J221724.79+00183.7	22 17 24.79	00 18 3.7	22.285	2.46	$HK500$	SSA22C	...
J221727.00+001746.4	22 17 27.00	00 17 46.4	23.225	0.90	$HK500$	SSA22C	...
J221728.51+00187.4	22 17 28.51	00 18 7.4	22.959	0.91	$HK500$	SSA22C	...
J221727.3+001809.5	22 17 27.29	00 18 9.5	22.688	1.19	$HK500$	SSA22C	3.091
J221734.86+001911.8	22 17 34.86	00 19 11.8	23.256	1.15	$HK500$	SSA22C	...
J221728.13+001850.4	22 17 28.13	00 18 50.4	20.833	1.02	$HK500$	SSA22C	...
J221737.29+001823.2	22 17 37.29	00 18 23.2	22.503	2.80	VPH-K	SSA22C	...
J221736.80+001818.2	22 17 36.80	00 18 18.2	23.129	1.60	VPH-K	SSA22C	...
J221737.00+001820.4	22 17 37.00	00 18 20.4	22.798	0.36	VPH-K	SSA22C	...
J221732.43+001743.8	22 17 32.43	00 17 43.8	23.332	1.41	VPH-K	SSA22C	...
					$HK500$	SSA22D	...
J221731.83+001738.2	22 17 31.83	00 17 38.2	23.831	1.23	VPH-K	SSA22C	...
J221732.01+001655.5	22 17 32.01	00 16 55.5	22.220	2.57	VPH-K	SSA22C	...
					$HK500$	SSA22D	...
J221736.64+001623.5	22 17 36.64	00 16 23.5	20.447	0.47	VPH-K	SSA22C	3.084

ID	R.A. (h.m.s)	Dec (d.m.s)	K_s[a] (mag)	$J-K$[b] (mag)	grism	mask-ID	$z_{\rm lit}$[c]
J221731.80+00166.3	22 17 31.80	00 16 6.3	23.009	1.70	VPH-K	SSA22C	...
J221737.11+001712.4	22 17 37.11	00 17 12.4	23.482	1.09	VPH-K	SSA22C	...
J221728.47+00168.1	22 17 28.47	00 16 8.1	23.585	0.04	VPH-K	SSA22C	...
J221732.19+00152.3	22 17 32.19	00 15 2.3	22.769	1.82	VPH-K	SSA22C	...
J221729.10+001642.6	22 17 29.10	00 16 42.6	...	...	VPH-K	SSA22C	...
J221737.29+001630.7	22 17 37.29	00 16 30.7	22.037	2.35	VPH-K	SSA22C	...
J221737.25+001816.0	22 17 37.25	00 18 16.0	21.551	2.80	$HK500$	SSA22D	...
J221727.81+001736.6	22 17 27.81	00 17 36.6	23.690	1.83	$HK500$	SSA22D	3.0922
J221729.61+001918.6	22 17 29.61	00 19 18.6	23.564	1.75	$HK500$	SSA22D	3.102
J221728.65+00208.0	22 17 28.65	00 20 8.0	23.397	0.64	$HK500$	SSA22D	...
J221728.53+00189.3	22 17 28.53	00 18 9.3	21.838	-0.13	$HK500$	SSA22D	...
J221728.35+001954.4	22 17 28.35	00 19 54.4	22.556	0.55	$HK500$	SSA22D	...
J221728.54+001822.2	22 17 28.54	00 18 22.2	22.957	0.45	$HK500$	SSA22D	...
J221731.44+001634.7	22 17 31.44	00 16 34.7	22.965	1.89	$HK500$	SSA22D	...
GDDS SA22-0630	22 17 32.35	00 16 15.9	20.644	0.86	$HK500$	SSA22D	0.753
J221729.74+001715.2	22 17 29.74	00 17 15.2	22.702	0.51	$HK500$	SSA22D	...
J221725.17+00185.7	22 17 25.17	00 18 5.7	22.726	2.16	VPH-K	SSA22D	...
J221722.01+00192.1	22 17 22.01	00 19 2.1	21.517	0.33	VPH-K	SSA22D	...
J221720.84+001925.2	22 17 20.84	00 19 25.2	23.568	0.96	VPH-K	SSA22D	...
J221722.26+00171.3	22 17 22.26	00 17 1.3	23.601	1.39	VPH-K	SSA22D	...
J221722.27+001640.0	22 17 22.27	00 16 40.1	20.465	0.30	VPH-K	SSA22D	3.353
J221721.92+001755.5	22 17 21.92	00 17 55.5	22.930	0.85	VPH-K	SSA22D	...
J221724.32+001945.1	22 17 24.32	00 19 45.1	22.620	-0.30	VPH-K	SSA22D	...
J221720.10+001939.4	22 17 20.10	00 19 39.4	22.352	3.04	VPH-K	SSA22D	...
J221724.65+001836.5	22 17 24.65	00 18 36.5	21.933	0.55	VPH-K	SSA22D	...

[a]Total magnitude, MAG_AUTO by SEXTRACTOR, in MOIRCS K-band.
[b]$J-K$ color in $1''.1$ aperture centered at coordinate on K-band images.
[c]Spectroscopic redshifts in the literatures; Yamada et al. (2012); Steidel et al. (2003); Lehmer et al. (2009b); Pettini et al. (2001). $z_{\rm spec}$ in the blackets are those of the other components in the same Lyα halos.

2.2. Data Reduction

The data reduction was performed by using IRAF scripts for Subaru/MOIRCS MOS data (MCSMDP) following its standard manner (e.g., Yoshikawa et al. 2010). Note that, the order-sorting filter was not used during the observation at September 29 and 30. We correct the contributions of the second order spectra. The errors from this procedure are $0.4-0.7\%$ of the flux values.

The spectral resolution with $HK500$ grism is 40Å for $0''.8$ slit and those with the VPH-K grism is 9Å and 11Å for $0''.7$ slit and $0''.8$ slit at 2.05 μm, respectively. The spectral coverages correspond to the redshifted range $z=2.9-3.6$ for the VPH-K grism and $z=1.9-3.6$ for $HK500$ grism excluding $z=2.7-2.9$ where the spectra are buried by strong atomospheric absorption.

Figure 7 are the examples of the obtained spectra. The spectrum of the full objects confirmed are shown in Appendix. The flux errors (gray shaded areas) in left figure is the 1σ Poisson errors of the sky spectra at each wavelength before A-B subtraction. The bottom panels are the two-dementional spectra of each object.

The efficiency of the VPH-K grism is the highest at $\sim$2.05 μm and almost uniform for our slit arrangements although it much depends on the wavelength and position of the slit.

Furthermore, since the crowded OH airglow emission lines are well resolved, the S/N ratios of the obtained spectra with the VPH-K grism are comparable to or higher at $\sim$2.05 μm while it is lower in other wavelength than those with the $HK500$ grism.

Emission lines are detected by visual inspection on the two-dimensional spectra. To obtain the one dimensional spectra, the two-dimensional spectra were integrated along the slit direction within the appropriate aperture giving the largest S/N for the detected emission lines. We use SPECFIT in IRAF (Kriss 1994), to measure the flux values and central wavelength of the emission lines from the one dimensional spectra, which fits multiple emission lines and continuum emission simultaneously. The emission lines are fitted to Gaussian profiles and the continuum spectra which are assumed to be a linear function of wavelength. The errors of the flux values are the errors of the flux values of best-fit models. The obtained flux values are listed in Table 2.2.

One object, J221737.3+001816.0 is confirmed to be at $z \sim 3.1$ from its Balmer/4000Å breaks. The spectrum of this object is shown in the right panel of Figure 7. The flux are stacked over the wavelength ranges indicated with the horizontal bars. The spectrum is obtained discretely due to the crowded OH airglow emission lines and/or atomospheric absorptions but there are significant breaks consistent with the Balmer/4000Å breaks at $z = 3.0 - 3.15$.

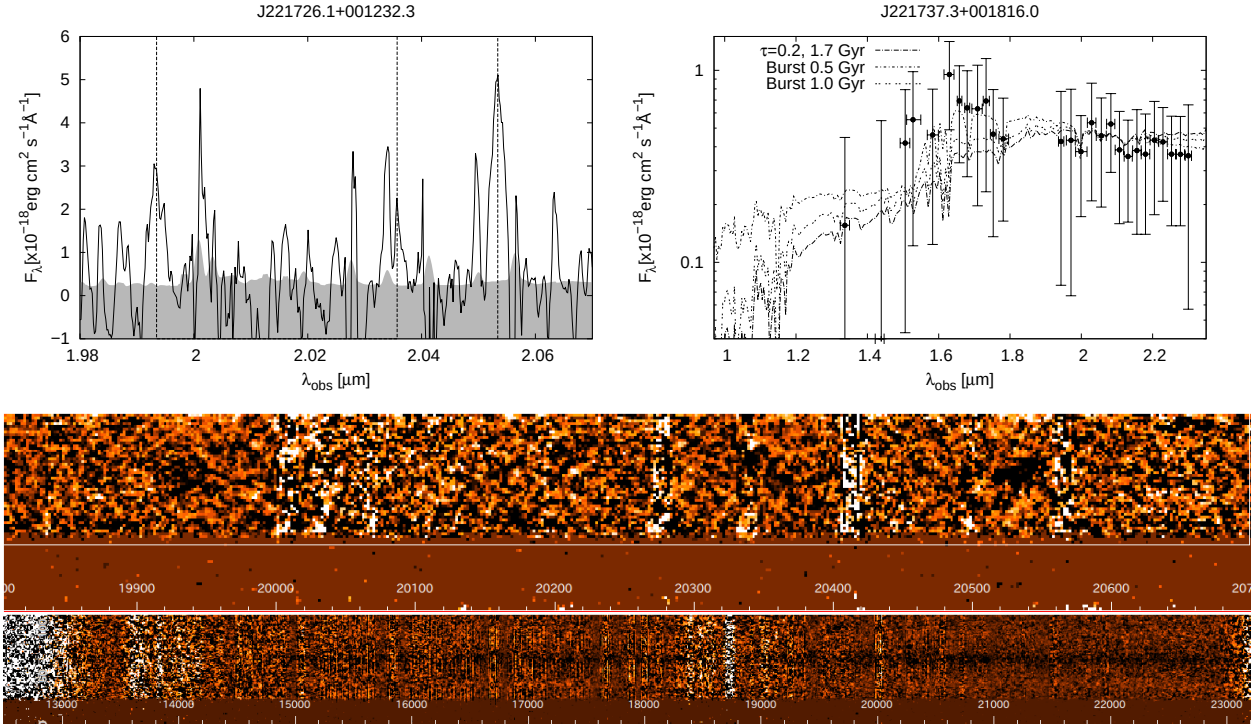

FIG. 7.— Examples of the obtained spectra. (*left*) Black solid line is the obtained spectrum and the gray shaded region is 1σ background noise, which is the Poisson noise of sky background. Dashed lines indicate the position of $[O_{III}]\lambda 5007, 4959$ and Hβ or Hα and $[N_{II}]$ emission lines. (*right*) Stacked spectrum of a continuum source J221737.3+001816.0. Black filled circles are stacked flux values at the range of vertical bars. We plot the best-fit SED model obtained with the broad-band photometric data (SFR $\propto \exp(-t/\tau)$ with $\tau = 0.2$, age = 1.7 Gyr) and also the SED models of single burst star-formation with ages = 0.5 and 1 Gyr. Middle and bottom panels are the 2D spectra of the objects in left and right top panels.

TABLE 4
List of the objects obtained the redshift

ID	K_s[a] (mag)	$J-K$[b] (mag)	$z_{\rm lit}$[c]	line	$z_{\rm spec}$	Flux (10^{-17} ergs/s/cm^2)	$M_{\rm star}$ (10^{10} $M_\odot$)	note
J221718.0+001735.6	23.5	1.1	...	[OIII] 5007	3.1423	12.4 ± 0.6	1.5	...
J221719.4+001657.1	23.2	1.4	...	[OIII] 5007	3.3082	5.8 ± 0.3	$0.2^{+0.4}_{-0.1}$	...
				[OIII] 4959	3.3063	4.1 ± 0.5		
J221716.4+001718.6	23.1	0.8	...	[OIII] 5007	3.3552	5.8 ± 0.4	1.3	...
J221715.7+001906.2	> 24	...	3.1015	[OIII] 5007	3.1008	2.0 ± 0.3	0.1	...
J221726.1+001232.3	22.1	1.3	...	[OIII] 5007	3.1000	13.8 ± 1.4	$6.9^{+0.2}_{-0.0}$	LAB01[d]
				[OIII] 4959	3.1028	7.1 ± 1.5		
				Hβ	3.1018	8.6 ± 0.9		
J221725.7+001238.7	23.6	0.3	...	[OIII] 5007	3.1007;	2.0 ± 0.3	$0.3^{+0.1}_{-0.2}$	LAB01[d]
				[OIII] 4959	3.1053;	2.0 ± 0.4		
J221724.9+001117.5	23.1	0.8	...	[OIII] 5007	3.0689	4.2 ± 0.4	$2.5^{+0.0}_{-0.0}$	LAB16[d]
J221732.5+001131.2	23.4	0.4	(3.086)	[OIII] 5007	3.0680	1.7 ± 0.3	2.0	LAB30[d]
J221732.5+001132.8	23.0	0.9	(3.086)	[OIII] 5007	3.0687	0.7 ± 0.2	0.6	LAB30[d]
J221733.9+001106.5	22.5	1.0	...	[OIII] 5007	2.8596	3.9 ± 0.4	$3.9^{+10.6}_{-3.5}$	...
J221730.2+001120.7	20.9	0.8	...	[OIII] 5007	3.0667	3.8 ± 0.3	2.8	...
J221720.8+001831.0	20.4	1.4	2.840	[OIII] 5007	2.9054	31.9 ± 1.6	67.7	....
J221726.3+001957.2	23.2	1.8	...	[OIII] 5007	3.0431	11.5 ± 1.2	2.2	...
J221724.8+001803.7	22.3	2.5	...	[OIII] 5007	3.3868	3.8 ± 1.9	$18.1^{+4.9}_{-3.5}$	...
J221727.0+001746.4	23.2	0.9	...	[OIII] 5007	3.3235	4.9 ± 0.5	0.1	...
J221728.5+001807.4	23.0	0.9	...	[OII] 3726	3.4281	9.1 ± 2.2	2.8	...
J221727.3+001809.5	22.7	1.2	3.091	[OIII] 5007	3.0861	10.3 ± 2.3	0.2	...
(SSA 22a MD46)				[OIII] 4959	3.0860	9.2 ± 3.7		
				Hβ	3.0857	5.6 ± 1.8		
J221734.9+001911.8	23.3	1.2	...	[OIII] 5007	3.0609	6.8 ± 1.3	0.1	...
J221737.3+001823.2	22.5	2.8	...	[OIII] 5007	3.0851	19.1 ± 0.7	$6.0^{+5.5}_{-1.8}$	Az14[e]
				[OIII] 4959	3.0851	5.9 ± 0.6		
				Hβ	3.0863	2.9 ± 0.3		
				[OIII] 5007	3.0926	6.5 ± 0.8		
				[OIII] 4959	3.0926	2.9 ± 0.3		
J221736.8+001818.2	23.1	1.6	...	[OIII] 5007	3.0854	2.8 ± 0.4	6.5	Az14[e]
J221737.0+001820.4	22.8	0.4	...	Hα	2.0786	3.6 ± 1.0	0.5	Az14[e]
J221732.0+001655.5	22.2	2.6	(3.094)	[OIII] 5007	3.0909	2.8 ± 0.7	8.7	LAB12[d]
				[OIII] 5007	3.1153	2.7 ± 2.0		
J221736.5+001622.6	20.4	0.5	3.084	[OIII] 5007	3.0945;	2.1 ± 3.5	25.6	...
J221731.8+001606.3	23.0	1.7	...	[OIII] 5007	3.0981	11.3 ± 0.8	$1.4^{+6.8}_{-1.0}$	...
				Hβ	3.1004	3.4 ± 0.4		
J221737.1+001712.4	23.5	1.1	...	[OIII] 5007	3.0899	7.2 ± 0.9	$3.0^{+13.4}_{-2.9}$	...
J221732.2+001502.3	22.8	1.8	...	Hα	2.3252	8.7 ± 1.7	$7.3^{+3.7}_{-6.6}$	...
				[NII] λ6584	2.3268	5.5 ± 0.7		
J221737.3+001630.7	22.0	2.4	...	[OIII] 5007	3.0888	6.1 ± 0.8	$6.8^{+0.0}_{-0.7}$	...
J221727.8+001736.6	23.7	1.8	3.0922	[OIII] 5007	3.0916	4.0 ± 2.2	2.0	...
J221729.6+001918.6	23.6	1.8	3.102	[OIII] 4959	3.1021	3.2 ± 2.5	0.3	...
J221728.3+001954.4	22.6	0.6	...	[OIII] 5007	3.1019	6.1 ± 1.6	$1.1^{+0.6}_{-0.1}$	...
				[OIII] 4959	3.1006	2.5 ± 1.1		
				Hβ	3.1028	8.2 ± 1.8		
J221728.5+001822.2	23.0	0.5	...	[OIII] 5007	3.3148	7.8 ± 0.6	0.2	...
J221729.7+001715.2	22.7	0.5	...	[OIII] 5007	3.1390	4.2 ± 3.9	3.5	...
J221725.4+001716.9	21.7	2.4	3.120	Hβ	3.0482	5.6 ± 0.6	$9.6^{+1.1}_{-0.0}$	...
J221725.2+001805.7	22.7	2.2	...	[OIII] 5007	3.0973	1.7 ± 0.4	14.7	Az99[e]

ID	K_s[a] (mag)	$J-K$[b] (mag)	$z_{\rm lit}$[c]	line	$z_{\rm spec}$	Flux (10^{-17} ergs/s/cm^2)	$M_{\rm star}$ (10^{10} $M_\odot$)	note
J221722.3+001640.1	20.5	0.3	3.353	[O III] 5007	3.3544	39.0 ± 1.4	1.3	
				[O III] 4959	3.3539	22.7 ± 2.4		
				Hβ	3.3593	12.6 ± 1.0		
J221721.9+001755.5	22.9	0.9	...	[O III] 5007	3.4075	11.3 ± 0.4	0.2	...
				[O III] 4959	3.4074	4.2 ± 0.5		
				Hβ	3.4096	3.2 ± 0.3		
J221724.3+001945.1	22.6	-0.3	...	[O III] 5007	3.1211	2.4 ± 0.4	0.2	...
J221724.6+001836.5	21.9	0.6	...	[O III] 5007	3.0847	2.3 ± 0.5	0.02	...
J221737.3+001816.0	21.6	2.8	...	continuum	3.1	...	21.0	Az14[e]

[a]Total magnitude, MAG_AUTO by SEXTRACTOR, in MOIRCS K-band.
[b]$J-K$ color in $1''.1$ aperture centered at coordinate on K-band images.
[c]Spectroscopic redshifts in the literatures.
[d]LABs in Matsuda et al. (2004).
[e]ASTE/AzTEC 1.1-mm sources in Umehata et al. submitted.
[f]Fitted with the emission line profile with double peaks.

2.3. Results

2.3.1. *The protocluster memberships*

Table 2.2 is the list of the 39 galaxies whose redshifts we obtained. The distribution of the spectroscopic redshifts is shown in Figure 8. [O$_{\rm III}$] λ5007 is difficult to observe at the redshift at $z = 3 - 3.03$ and $z = 2.7 - 2.95$ (gray shaded region) due to crowded OH airglow emission. There is a very clear redshift spike at $z \approx 3.09$ where 24 out of the 39 galaxies are the protocluster members at $z_{\rm spec} = 3.04 - 3.12$.

As we have reported in the previous section, there are 1.7 times many galaxies with $z_{\rm phot} = 2.6 - 3.6$ and $K_{\rm AB} < 24$ in the SSA22 field of those in the general field. The fraction of the protocluster galaxies among the targets is expected to be $0.7/1.7 \sim 40\%$. Actually, $36\pm12\%$ of the whole targets are the protocluster galaxies. Therefore most of the protocluster galaxies among the targets may be confirmed their redshifts. Although the sensitivity would not be enough for some objects. The sensitivity of the observations corresponds to the SFR of several 10 M$_\odot$yr^{-1}, depends on the degree of the extinction, assuming the Hα to Hβ, [O$_{\rm III}$] ratio and Hα luminosity to SFR relations of local star-forming galaxies (Kennicutt 1998). Balmer/4000Åbreaks are detectable for only some bright objects with $K_{\rm AB} < 22$ by using $HK500$ grism.

11 of the 39 galaxies are known to be at $z_{\rm spec} = 2.8 - 3.4$ from the previous optical (Table 2.2, Steidel et al. 2003; Lehmer et al. 2009b; Yamada et al. 2012) and/or NIR (Pettini et al. 2001) spectroscopic observations. Our spectroscopic redshifts are agree well with those in literatures. The redshift offset of the object J221725.4+001716.9 with $z_{\rm H\beta} = 3.0482$ ($z_{\rm lit} = 3.120$) is the largest.

Figure 9 is the comparison of spectroscopic redshifts and photometric redshifts of the galaxies. Except for some outliers, the error distribution is nearly Gaussian distribution around zero. Excluding the objects with $|\Delta z|/(1+z_{\rm spec}) > 0.5$ where $\Delta z = z_{\rm phot} - z_{\rm spec}$, The standard deviation of $\Delta z/(1 + z_{\rm spec})$ are 0.09 for the galaxies at $z_{\rm sepc} = 3.04 - 3.12$, 0.03 for those at $z_{\rm spec} = 2.5 - 3$ and 0.17 for those at $z_{\rm sepc} = 3.3 - 3.4$.

In Kubo et al. (2013), we also measured other photometric redshifts of 33 protocluster galaxies with archival spectroscopic redshifts, which were measured by optical spectroscopic observations. The standard deviation was $< \Delta z/(1 + z_{\rm spec}) >= 0.07$, excluding the galaxies with $|\Delta z|/(1 + z_{\rm spec}) > 0.5$. The number of galaxies with redshifts mistaken catastrophic were three while that of our NIR spectroscopic observation was five out of 23. As we will describe in §3.3.3, since they are faint in optical, the SED fitting of our sample are not well as that of the optically confirmed protocluster members.

The stellar mass values listed in Table 2.2 are estimated based on the SED fitting. The precise descriptions of this procedure are given in §3.3.3. The stellar mass of the protocluster galaxies in our sample is ranging from $10^{9.5}$ to 10^{11} M$_\odot$, larger than those of the typical LBGs at $z \sim 3$ (Shapley et al. 2001; Papovich et al. 2001).

There are already many protocluster galaxies spectroscopically identified in rest-frame UV wavelength, like LBGs and LAEs. Our sample are typically faint in rest-frame UV; only five out of the 24 are detected in the existing V-band image (at $V = 26.5$ at 5σ limit); Lyα emissions are detected in the narrow-band image for Lyα emission at $3.06 < z_{\rm spec} <$

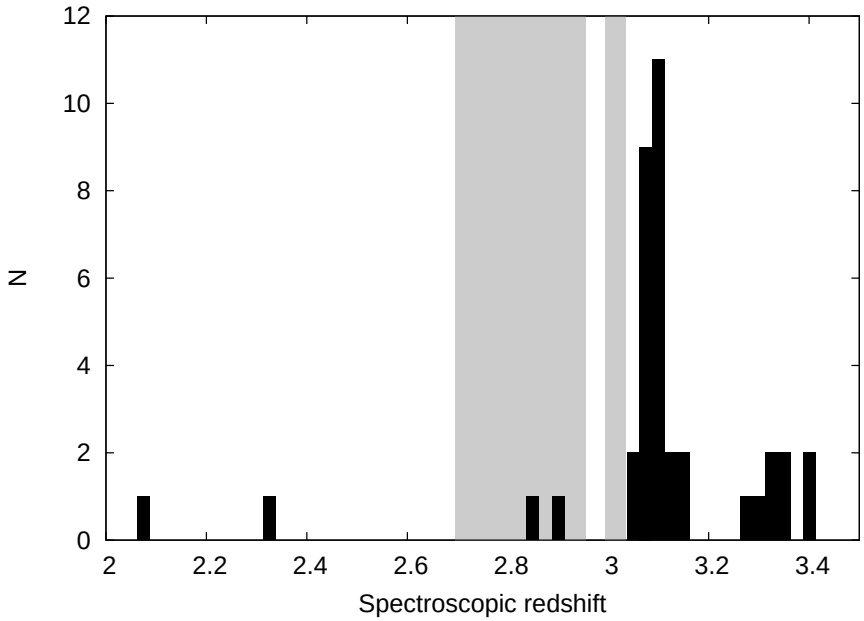

FIG. 8.— The spectroscopic redshift distribution of the galaxies. Black histogram is the spectroscopic redshift distribution of the objects confirmed by this observation. Gray shaded region is at wavelength where sensitivity drops so much because of atomospheric absorption and significant OH airglow emission lines. There is very clear redshift spike at $z = 3.09$.

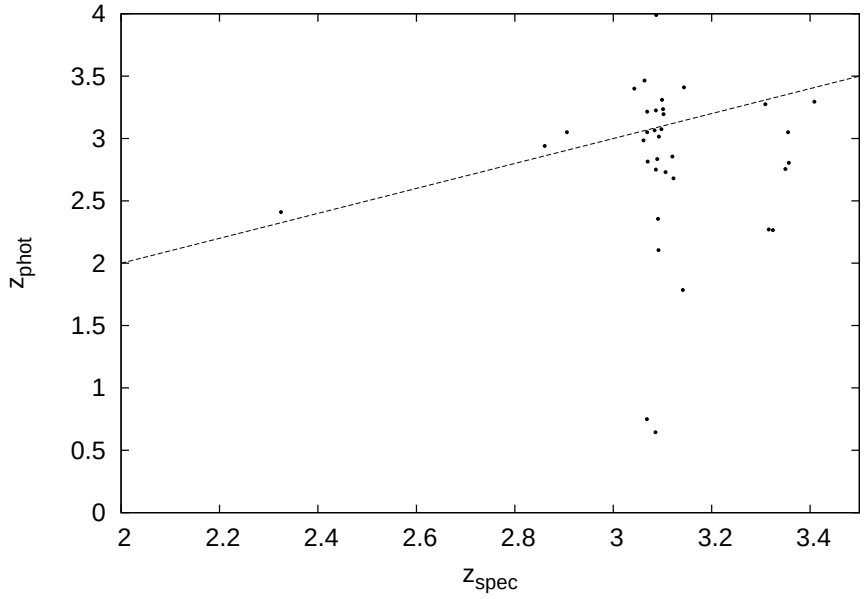

FIG. 9.— The comparison of the spectroscopic redshifts v.s. photometric redshifts of the objects confirmed by this observation. The dashed line is the line with equal $z_{\rm phot}$ and $z_{\rm spec}$.

3.12 ($NB497$; Hayashino et al. 2004) above 4σ significance for eight out of the 22 galaxies at $3.06 < z_{\rm spec} < 3.12$. From these above, we emphasize that we identified the different populations of the protocluster galaxies from those previously studied.

We summarised the results of some unique targets in Table 4; DRGs; HEROS; *Spitzer* MIPS 24 μm sources (Webb et al. 2009); *Chandra* X-ray sources (Lehmer et al. 2009b); LAEs (Hayashino et al. 2004). Many of them are the members of the protocluster.

Note that the 24 μm sources may be both dusty starburst galaxies and/or obscured AGNs (e.g., Daddi et al. 2007). Actually, four out of the 18 of the 24 μm sources are also detected by *Chandra*. On the other hand, one of the 24 μm sources are likely to be the counterpart of the ASTE/AzTEC 1.1-mm sources, AzTEC 99, supporting that dusty starburst also contribute to the 24 μm sources.

We also observed the counterparts of four LABs and three ASTE/AzTEC 1.1-mm sources. More than one counterparts at $z_{\rm spec} \approx 3.09$ are identified for each object excluding one AzTEC source (AzTEC01 in Umehata et al. submitted). The presence of multiple counterparts for many LABs and SMGs in the SSA22 field were reported in Uchimoto et al. (2012). Such objects are likely to be the hierarchical multiple mergers at the early-phase of the formation history of massive early-type galaxies predicted in the cosmological numerical simulations (e.g., Meza et al. 2003; Naab et al. 2007). Detailed description of them are written in Chapter 3.

TABLE 4
Summary of the targets

Classification	$N_{\rm targets}$	$N_{\rm cluster}$[a]	$N_{\rm field}$[b]
All	67	24	15
DRGs ($J-K>1.4$)	21	11	4
HEROs ($J-K>2.1$)	9	6	1
24 μm sources	18	7	5
X-ray sources	14	4	4
LAEs	5(12)[c]	5(11)[c]	0

[a]Number of the galaxies confirmed to be at $3.04 < z_{\rm spec} < 3.12$.
[b]Number of the galaxies confirmed the redshifts, excluding protocluster galaxies.
[c]Number of the LAEs selected with the narrow-band filter $NB497$ which is sensitive to Lyα emission line at $z = 3.062 - 3.125$ (Hayashino et al. 2004; Yamada et al. 2012). The numbers in the brackets includes of the objects which do not satisfy the robust color criterion of the LAEs but show excess in $BV-NB497$-band colors above 4σ significance.

2.3.2. *The emission line properties*

We summarised the emission line properties of the galaxies in Table 5. $r_{[\mathrm{O_{III}}]}$ of the objects are the FWHM of the spatial extent of the [$\mathrm{O_{III}}$] emission line which are deconvolved of the seeing size. When the spatial extents of the emission lines are not well resolved, the r corresponding to seeing size are put as upper limit in the table. Velocity dispersion are calculated for the objects observed with VPH-K grism while its instrumental resolution is 11 Å, well resolve the kinematics of the galaxies with the velocity dispersion $\sigma > 70$km s^{-1}. We calculate the velocity dispersion $\sigma = \mathrm{FWHM}/2.35$, where FWHM is that of the emission line which subtracted of the instrumental resolution.

Figure 10 is the comparison of the emission line properties of our catalog. For comparison, we also plot the velocity dispersions and spatial extents of Hα emission lines of BzK galaxies at $z = 2$ (Erb et al. 2006b) and the velocity dispersion of [$\mathrm{O_{III}}$] emission lines of LBGs at $z = 3$ (Pettini et al. 2001). It was reported in Erb et al. (2006b) that the line widths and spatial extents of the emission lines estimated with Hα and [$\mathrm{O_{III}}$] are not so much different. The stellar mass range of the BzK galaxies is similar to our sample. The LBGs in Pettini et al. (2001) are biased to the bright sample in rest-frame optical. Then the stellar mass range of comparison samples is not so different with our sample.

The average and standard deviation of the velocity dispersion of the all galaxies in our catalog are 128±35 km s^{-1}, that of the protocluster galaxies are 140±30 km s^{-1} and that of the field galaxies are 105±28 km s^{-1}, excluding the objects with $\sigma > 300$ km s^{-1}. Excluding the X-ray detected AGNs in the protocluster, the average and standard deviation of the velocity dispersion of the protocluster galaxies become 121±54 km s^{-1} while 173±58 km s^{-1} for the rejected three AGNs in the protocluster. The average of the velocity dispersion of BzKs is 97 km s^{-1} (Erb et al. 2006b). and that of LBGs at $z = 3$ is 70 km s^{-1} (Pettini et al. 2001). The velocity dispersion of the field galaxies in our catalog is similar to or slightly higher than that of the BzKs but that of the protocluster galaxies is larger. On the other hand, the average velocity dispersions of our samples is much higher than that of the LBGs at similar redshift.

The average of $r_{[\mathrm{O_{III}}]}$ of our catalog is $0''.7$, which corresponds to ~ 5 kpc while that is $0''.7$ (6 kpc) for $r_{\mathrm{H}\alpha}$ of BzKs at $z = 2$ (Erb et al. 2006b). They reported that there are no difference in size measured with [$\mathrm{O_{III}}$] and Hα and the difference of the redshift $z \sim 2$ to $z = 3$ does not significantly affect the results.

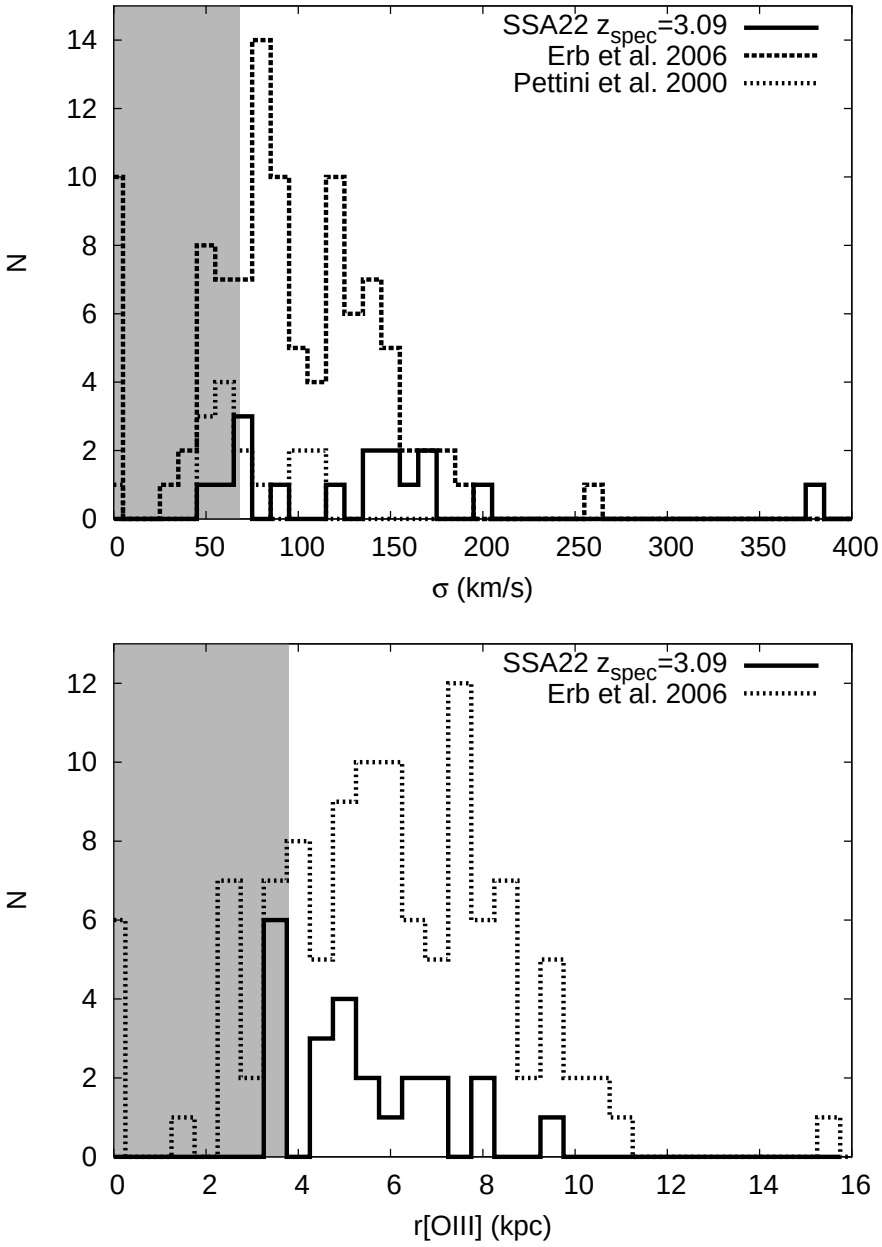

FIG. 10.— Distribution of the spatial extent and velocity dispersion of [O_{III}] emission lines of the proto-cluster galaxies (black solid lines). Dashed lines are those of Erb et al. (2006b) and Pettini et al. (2001). Gray shaded region indicate the limiting size or σ in our observation.

TABLE 5
SUMMARY OF THE σ_v AND r

ID	$z_{\rm spec}$	σ_v[a] (km s^{-1})	$r_{[\rm O\,III]}$[b] (kpc)
J221725.7+001238.7	3.1007	31 ± 22	4.9
J221733.9+001106.5	2.8596	37 ± 21	4.7
J221725.2+001805.7	3.0973	65 ± 31	< 3.8
J221732.5+001131.2	3.0680	70 ± 21	< 3.8
J221724.3+001945.1	3.1211	78 ± 22	< 3.8
J221721.9+001755.5	3.4075	79 ± 6	6.6
J221715.7+001906.2	3.1008	81 ± 10	6.9
J221716.4+001718.6	3.3552	84 ± 9	3.9
J221732.0+001655.5[c]	3.0909	111 ± 43	< 3.8
J221736.8+001818.2	3.0854	114 ± 23	4.8
J221719.4+001657.1	3.3082	123 ± 11	< 3.7
J221724.6+001836.5	3.0847	135 ± 38	5.0
J221726.1+001232.3	3.1000	139 ± 19	3.4
J221724.9+001117.5	3.0689	142 ± 18	8.1
J221731.8+001606.3	3.0981	164 ± 20	5.3
J221737.1+001712.4	3.0899	180 ± 28	4.9
J221737.3+001630.7[c]	3.0888	182 ± 36	9.6
J221722.3+001640.1	3.3544	198 ± 9	6.3
J221730.2+001120.7	3.0667	208 ± 19	3.8
J221737.3+001823.2[c]	3.0851	225 ± 11	4.6
J221718.0+001735.6	3.1423	337 ± 18	12.0
J221732.5+001132.8	3.0687	< 69	1.6

[a]The velocity dispersion of the galaies.
[b]The spatial extent of [O III]λ5007 emission lines.
[c]The objects detected in *Chandra* X-ray

2.3.3. *The SED modeling*

We obtained the best-fit SED models of the galaxies confirmed to study their stellar populations.

For this purpose, we use the fluxes of the objects in $u^{\star}BVRi'z'JHK$ and IRAC 3.6μm, 4.5μm, 5.8μm and 8.0μm bands after correcting for the effects of different PSF sizes. The flux in the optical $u^{\star}BVRi'z'$ bands is measured at the position of them on K-band except for one LAE, SSA221715.7-001906.2 which are not detected in K-band ($K < 24$). The fluxes of this LAE were measured at its position on V-band image. The measured flux values are performed aperture correction. The procedures of the aperture corrections were described in §1.1.2.

Then we performed the SED fitting by using HyperZ code (Bolzonella et al. 2000). We used GALAXEV (Bruzual & Charlot 2003) models with the Chabrier Initial Mass Function (IMF) (Chabrier 2003) as template SED models. Note that we used the Salpeter IMF (Salpeter 1955) in our previous studies (§. 2, Kubo et al. (2013)). We here use Chabrier IMF to compare our results with other studies in which the Chabrier IMF was adopted. The range of the metallicity is from 1/100 to 1 times the solar value. The star formation histories of each template are single burst, constant-rate continuous star formation, and exponentially decaying star formation with timescales of $\tau = 0.1 - 30$ Gyr. We adopt the Calzetti et al. (2000) extinction law with a range of extinctions covering $E(B-V) = 0.0 - 4.0$.

Left panels of Figure 32 are the best-fit SED models of the galaxies confirmed in this study. The objects fitted above 70% confidence levels are shown here. The rest of the galaxies are shown in Appendix. The right panels show the distributions of the confidence levels on $A_{\rm v}$ v.s. Age plane. The degeneracy of the best-fit models are large for some galaxies which are well fitted with both old quiescent models and dusty young (star-forming) models. On the other hand, especially the galaxies well fitted with old quiescent models have quite low degeneracy with dusty young models.

The galaxies whose SED are well fitted for confidence level $> 70\%$ are 13 out of the 34 galaxies while most of the rest-frame UV selected galaxies in archive (§1.2) were well fitted by the similar SED fitting procedures. There are several reasons for these poor fits of our sample.

The poor fits are mainly due to the faintness of the galaxies. They certainly show Lyman break and Balmer/4000Å breaks but their flux values are too faint to be constrained of the SED parameters robustly. In addition, other SED models may be required for some galaxies. Some of them have flat SEDs which may be dominated by the AGN components. The SED models with more complex star-formation histories, e.g., second burst, can be applied (e.g., Papovich et al. 2006) but alowed models become too many. In this work, we will discuss the properties of the galaxies well fitted by the SED fitting procedures described above.

Note that the stellar mass values can change due to the adopted IMF. The low-mass end of the IMFs (below $\sim$1 $M_{\odot}$) are fall off in most IMFs, including the Chabrier IMF, while there is no fall off at the faint end of the Salpeter IMF. Then more faint stars are formed with the Salpeter IMF. It have been reported in many studies that the stellar mass of galaxies are overpredicted if we adopt the Salpeter IMF (e.g., Bell et al. 2003; Erb et al. 2006a; Yoshikawa et al. 2010). It was reported in Erb et al. 2006a that the stellar mass obtained adopting the Salpeter IMF is 1.8 times of that obtained adopting the Chabrier IMF.

With the spectroscopic redshift informations, we can more accurately obtain the best-fit parameters. The range of the permitted parameters are decreased to 20-50% of that obtained from the SED modeling without firm redshifts.

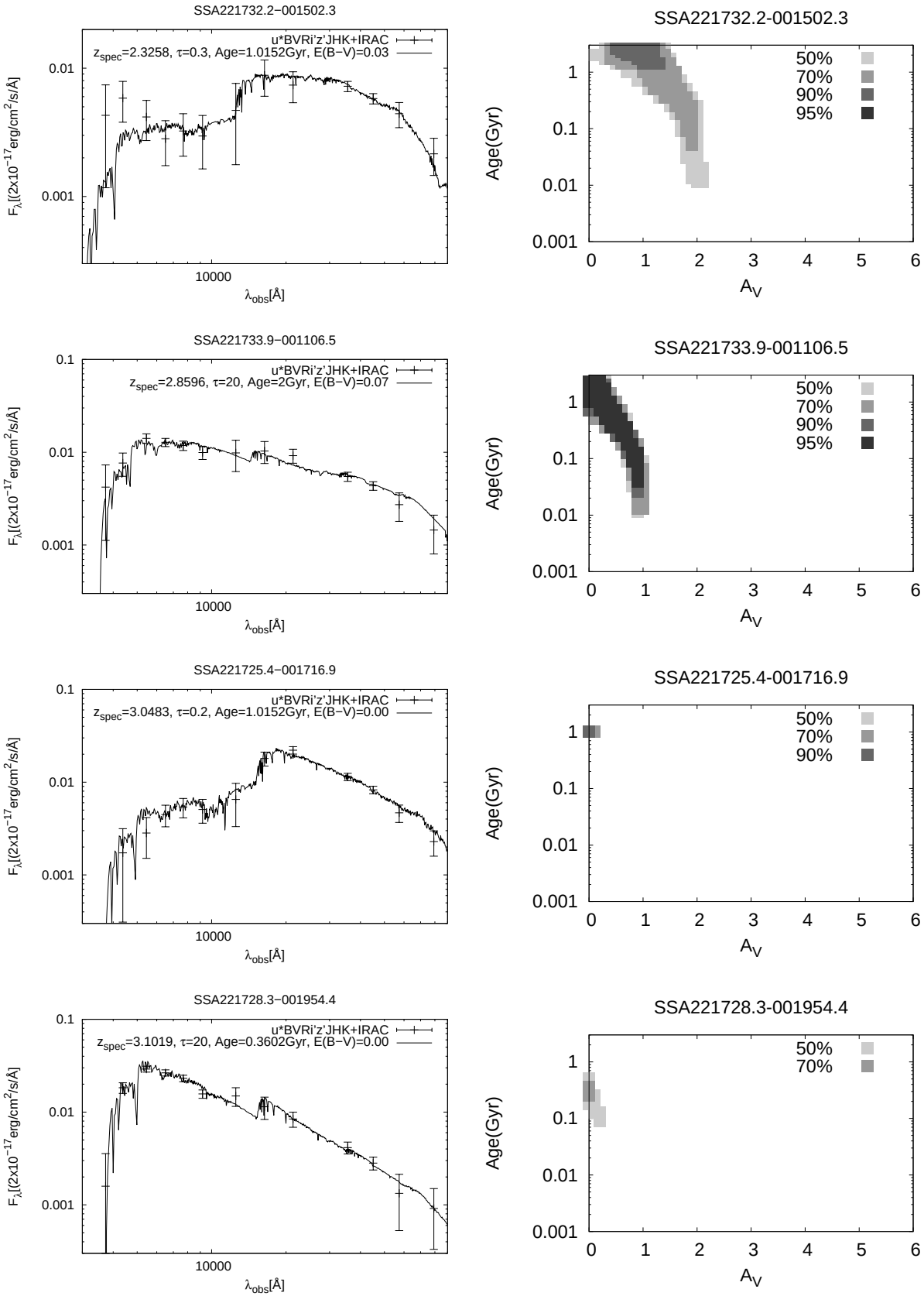

FIG. 11.— The best-fit SED models of the galaxies which are fitted with model SED of galaxies above 70% confidence level. The cross points are the observed points of $u^\star, B, V, R, i', z', J, H, K$, 3.6$\mu$m, 4.5$\mu$m, 5.8$\mu$m and 8.0$\mu$m. The black solid lines are best fit SED models.

3. DISCUSSION

3.1. The Structure of the SSA22 protocluster

To study the formation and evolution of galaxies, the mass of the structure in which they are hosted is very important. It is well known that there are environmental dependence on the properties of the galaxies in the current universe (e.g., Oemler 1974; Dressler 1980; Kauffmann et al. 2004). It is predicted in the biased structure formation scenario in the CDM universe that the galaxies are preferentially formed from the density peaks in the high density region at high redshift (e.g., Kaiser 1984). Then massive galaxies at the cores of massive clusters should have begun formed earlier. In addition, there are also the environmental effects on the galaxy evolution in later ($z \lesssim 1$), e.g., mergers, interactions, tidal and ram-pressure stripping (Gunn & Gott 1972; Dressler & Gunn 1983) are also expected.

From these above, it is needed to compare the clusters of galaxies which will evolve into similar structures in the current universe to study the evolution of galaxies in the protoclusters. However it is hard to measure the robust mass of the protoclusters at $z > 2$ due to the observational limits to date. But we can obtain some suggestions about mass of the structures from indirect methods like the strength of the density excess and the velocity dispersions of the galaxies in the protoclusters.

The SSA22 protocluster is known as a very rare density peak at high redshift. From the narrow-band survey of the LAEs at $z = 3.09$ for 1.38 deg^2 area in the SSA22 field, the SSA22 protocluster is well characterized as a significant density peak at that epoch (Yamada et al. 2012). They reported that the average density of the LAEs at $z = 3.09$ at the peak is 6 times the average density in the general fields. Then this structure is characterized as an extremely rare peak at that epoch, suggesting that this protocluster is very likely to be one of the progenitors of most massive clusters in the current universe.

On the other hand, LAEs at $z = 2 - 3$ are thought to be dominated by star-forming galaxies with small stellar mass (e.g., Gawiser et al. 2006; Finkelstein et al. 2007; Lai et al. 2008). The mass of background dark matter halos are generally measured through the clustering strength of the spatial distributions of the galaxies. The clustering strength of LAEs at $z = 2 - 3$ are weakest among the galaxies found at similar redshift like LBGs and DRGs (e.g., Quadri et al. 2007; Gawiser et al. 2007; Ichikawa et al. 2007) and they are likely to be hosted in the low-mass dark matter halos. Then they would not be good tracers for the mass distributions. To investigate the properties of the structure, the galaxy populations hosted in massive dark matter halos are more appropriate tracers. At $z = 2 - 4$, the red galaxies like DRGs are the most strongly clustered galaxies and the K-band bright massive galaxies also show strong clustering (e.g., Quadri et al. 2007; 2008; Ichikawa et al. 2007). The clustering strength of them correspond to those of the dark matter halos with mass $\sim 10^{12}$ M$_\odot$, which are most massive halos for each individual galaxy.

Here we can study the structure of the SSA22 protocluster with the K-selected galaxies which may be hosted in massive halos by using the deep NIR imaging and spectroscopic data. In this section, we are going to investigate the mass of the SSA22 protocluster from the velocity dispersion and also the density enhancement of the galaxies in the protocluster

by using not only the K-selected galaxies but also the rest-frame optically selected galaxies.

First, we study the dynamical mass of the protocluster by using the velocity dispersion of the galaxies. Figure 12 shows the redshift distributions of the galaxies within 2.1 Mpc (in physical scale), which corresponds to Abell radius, of the central region of the SSA22 protocluster. The center of the aperture is taken slightly westward the surface density peaks of the LAEs at $z \approx 3.09$ (Yamada et al. 2012) and the K-selected galaxies at $z_{\rm phot} \sim 3.1$ (K13) in Figure 6. The numbers of the objects in Figure 12 are 20 for our sample, 75 for the previous other optical observations (Steidel et al. 2003; Lehmer et al. 2009b; Matsuda et al. 2005; Yamada et al. 2012 and also SDSS surveys) and 89 for the combined sample of these two. If the redshifts were obtained from both ours and optical observations, we adopt the redshifts obtained by our observations.

The LAEs at $z = 3.062 - 3.125$ are selected with the narrow-band filter (Hayashino et al. 2004). The selection function for the LBGs and photo-z selected galaxies are uniform at the given redshift range. The typical offset of the redshift obtained by Lyα from the systemic redshift was reported to be a few 100 km s^{-1} in velocity (e.g., Verhamme et al. 2006; Steidel et al. 2010). In our sample, the offset values are a few 100 km s^{-1} excluding outliers with $|\Delta v| > 5000$ km s^{-1}. We ignore the velocity offsets of ours and archival observations in calculating the velocity dispersion as we discuss the structure which is likely to be the analogue of local massive clusters of galaxies with velocity dispersion $\sigma \sim$1000 km s^{-1}. There are no significant bias of the spectroscopic observations around the density peak; Targets in our observations are distribute around and also at south of the density peaks and around LAB01. The archival observations of Steidel et al. 2003 (LBGs) and Lehmer et al. 2009b (*Chandra* X-ray sources) cover the central to south region of the FoV. The archival observations of Matsuda et al. 2005 and Yamada et al. 2012 (LAEs) uniformly covers the MOIRCS FoV.

The velocity distribution of the combined sample shows a Gaussian like profile, which suggest that the core of the protocluster is likely to be an already relaxed system. The dashed lines in Figure 12 are the results of the Gaussian fittings of each velocity distribution. The range of the redshift used in fittings is $3.04 < z < 3.12$. We obtain $\sigma = 605 \pm 134$ km s^{-1} for our sample, $\sigma = 1205 \pm 122$ km s^{-1} for the rest-frame UV selected sample and $\sigma = 1058 \pm 147$ km s^{-1} for the combined sample. The centers of each redshift distribution agree well while those are $z = 3.092$ and 3.088 for our and the combined sample, respectively. It is slightly decrease to $\sigma = 960 \pm 156$ km s^{-1} at $3.06 < z < 3.12$ for the combined sample. Without Gaussian fittings, the velocity dispersion of each sample are 1394 ± 733 km s^{-1} (440 ± 220 km s^{-1} at $3.08 < z < 3.12$, excluding the objects at $z < 3.06$ since there is an interval.), 1102 ± 441 km s^{-1} and 1175 ± 441 km s^{-1}, respectively. These values agree well with the results obtained by using Gaussian fittings. Red histogram in Figure 12 is that for the galaxies with stellar mass $> 10^{10.5}$ M$_\odot$. We obtain 368 ± 121 km s^{-1} for this most massive sample. Although the number of the sample is not large, most massive galaxies have more tight velocity distribution than those of the other samples.

We check the surface and redshift distribution of the galaxies in the protocluster (Figure 13). We plot the galaxies binning with $\Delta z = 0.02$. The galaxies confirmed from our and archival observation are plotted with filled and blank points, respectively. The clustering of the galaxies at $3.08 < z_{\rm spec} < 3.10$ is most significant and this may be the core of the protocluster. They are clustered at the region where the surface number density of the LAEs at $z = 3.09$ is the highest (a green solid contour). The clustering of galaxies at $z = 3.04 - 3.08$

and $z = 3.10-3.12$ are weaker and most of them are likely to be the outskirt of the structure. On the other hand, there are small clustering of galaxies at $z = 3.06 - 3.08$ at slightly north of the density peaks and at $z = 3.10 - 3.12$ at south of the density peaks. These small clusterings can be sub-structures on-going mergers to the core of the protocluster. Then it is conservative to estimate the velocity dispersion excluding these substructures. As a result, we obtain 623 ± 223 km s^{-1} for the combined sample.

We compared our results with numerical simulations of the massive clusters in the ΛCDM universe by Eke et al. (1998). They simulated the evolutions of the radial density profiles and velocity dispersions of the dark matter halos in the massive clusters with halo mass $\sim 10^{15}$ M$_\odot$ and $\sigma_{\rm DM} = 800 - 1000$ km s^{-1} at $z = 0$, the most massive clusters in the current universe. It is predicted that the velocity dispersion of dark matter increases with cosmic time. In their simulations, the velocity dispersions of the massive clusters of galaxies with $\sigma_{\rm DM} = 1000$ km s^{-1} in the current universe are ~ 500 km^{-1} at $z = 3$. The velocity dispersion of the galaxies in the SSA22 protocluster is ~ 1000 km s^{-1}, about two times of the prediction for most massive clusters in the current universe. On the other hand, that obtained excluding the substructures agree well with or slightly larger than those predicted.

The virial mass of the protocluster is given as,

$$M \simeq \alpha \frac{\sigma^2 R}{G}$$

assuming the virial equilibrium. The factor α takes 1/2-5 due to the assumptions of the geometries. Assuming the radius of the cluster core as 2.1 Mpc, the virial mass of the SSA22 protocluster is $\sim 2-15\times10^{14}$ M$_\odot$ (all) and $\sim 0.5-5\times10^{14}$ M$_\odot$ (excluding the substructures).

On the other hand, the protocluster may not be fully virialized at $z = 3$. Then we also estimate the mass of the protocluster from the density excess in the protocluster as $M = \bar{\rho}V(1+\delta_{gal}/b)$ following Steidel et al. (1998) and Venemans et al. (2005), (2007). The $\bar{\rho}$ is the mean density of the universe at that epoch, the V is the comoving volume occupied by the overdensity, the δ_{gal} is the overdensity of the galaxies in the protocluster and b is the bias parameter of the galaxies. In this case, we adopt $\bar{\rho} = 3.5\times10^{10} M_\odot$ Mpc^{-3} and $V \sim 1.5\times10^4$ Mpc^3 (similar size and redshift range as used in the dynamical mass measurements). Note that there are uncertainties on the bias parameters. The bias parameter for the LAEs at $z = 3$ is $b = 3 - 4$ (e.g., Gawiser et al. 2007; Yamada et al. 2012). The bias parameters for the DRGs at $z = 2 - 4$ is measured as $b \sim 5$ and those for the galaxies with $K < 23$ at $2 < z < 4$ is ~ 3 (e.g., Quadri et al. 2007; Ichikawa et al. 2007). Here we assume $b = 3 - 4$ for the LAEs and $b = 3 - 5$ for the K-selected galaxies.

We estimated the overdensity of the K-selected galaxies from the density excess of the galaxies selected based on the photometric redshifts. Since there are 1.7 times many galaxies with $2.6 < z_{\rm phot} < 3.6$ in the SSA22 field, $0.7/1.7 \sim 40\%$ of them should be concentrated at the narrow redshift range $3.04 < z < 3.12$. Then there is the K-selected galaxies roughly $\sim$10 times of the background density in the protocluster. This is also supported from the fraction of the protocluster galaxies among the targets. The overdensity of the LAEs at the density peak of the SSA22 protocluster is 6. After divided with each bias parameter, those become 1.5-2 (LAEs) and 2-3 (K-selected), respectively. The mass of the structures is obtained to be $\sim 1\times10^{15}$ M$_\odot$ (LAEs) and $1-2\times10^{15}$ M$_\odot$ (K-selected), agree well with each other. It is also consistent with the dynamical mass estimated from the velocity dispersion. These values are consistent or higher than those of the protoclusters at $2 < z < 4$ obtained by Venemans et al. (2007).

How is the SSA22 protocluster, with mass $\sim 10^{15}$ $M_\odot$ at $z = 3$, placed in the cosmological models? We compared our results with the evolution of mass function of dark matter halo in the ΛCDM universe simulated by Mo & White (2002). The number density of the dark matter halos with mass $\sim 10^{14}$ $M_\odot$ is *Log* n $/(h^{-1}$ Mpc$)^{-3} = -7$ and mass $\sim 10^{15}$ $M_\odot$ is *Log* n $/(h^{-1}$ Mpc$)^{-3} = -10.5$ at $z = 3$, in the comoving scale (roughly extend the sequence in Mo & White 2002). Therefore the halos with mass $> 10^{14}$ $M_\odot$ at $z = 3$ are very rare density peaks. If their model correctly reproduces the actual number density of the dark matter halos, the SSA22 protocluster is hosted in namely, a halo which can be found from $10^{10.5}$ Mpc^3 survey volume. This means that one such cluster can be found from the survey of the galaxies all over the universe at $z = 3.04 - 3.12$.

The NIR imaging and spectroscopic observations give similar results as those obtained from the optical surveys that the SSA22 protocluster is a very rare density peak at $z = 3$. Although we need further discussion of not only the cosmological model adopted here and also the methods to estimate the mass, but this protocluster is very likely to be the core of one of the most massive clusters in the current universe in the current universe.

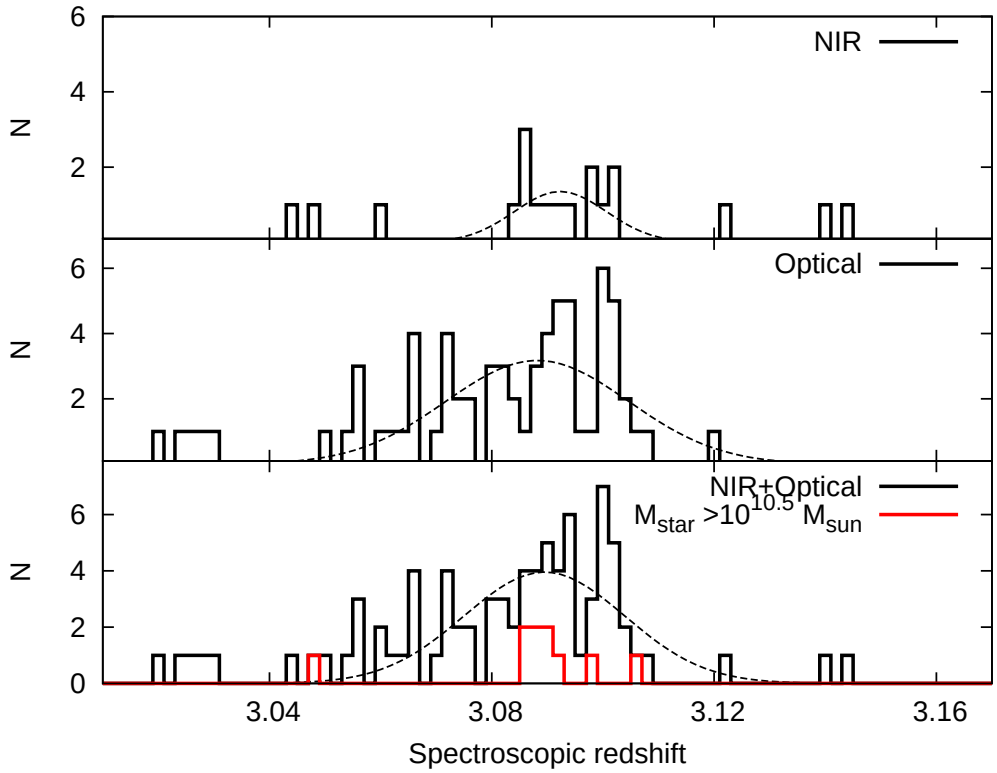

FIG. 12.— The redshift distributions within the central 2.1 Mpc of the protocluster. Black histograms are the redshift distribution of our sample (top), that of the galaxies confirmed the redshifts by optical spectroscopy (middle) and that of the combined sample (bottom). Red solid line in the bottom panel is that of the galaxies with $M_{star} > 10^{10.5}$ $M_{\odot}$. Dashed lines indicate the best-fit Gaussian profiles of each redshift distribution.

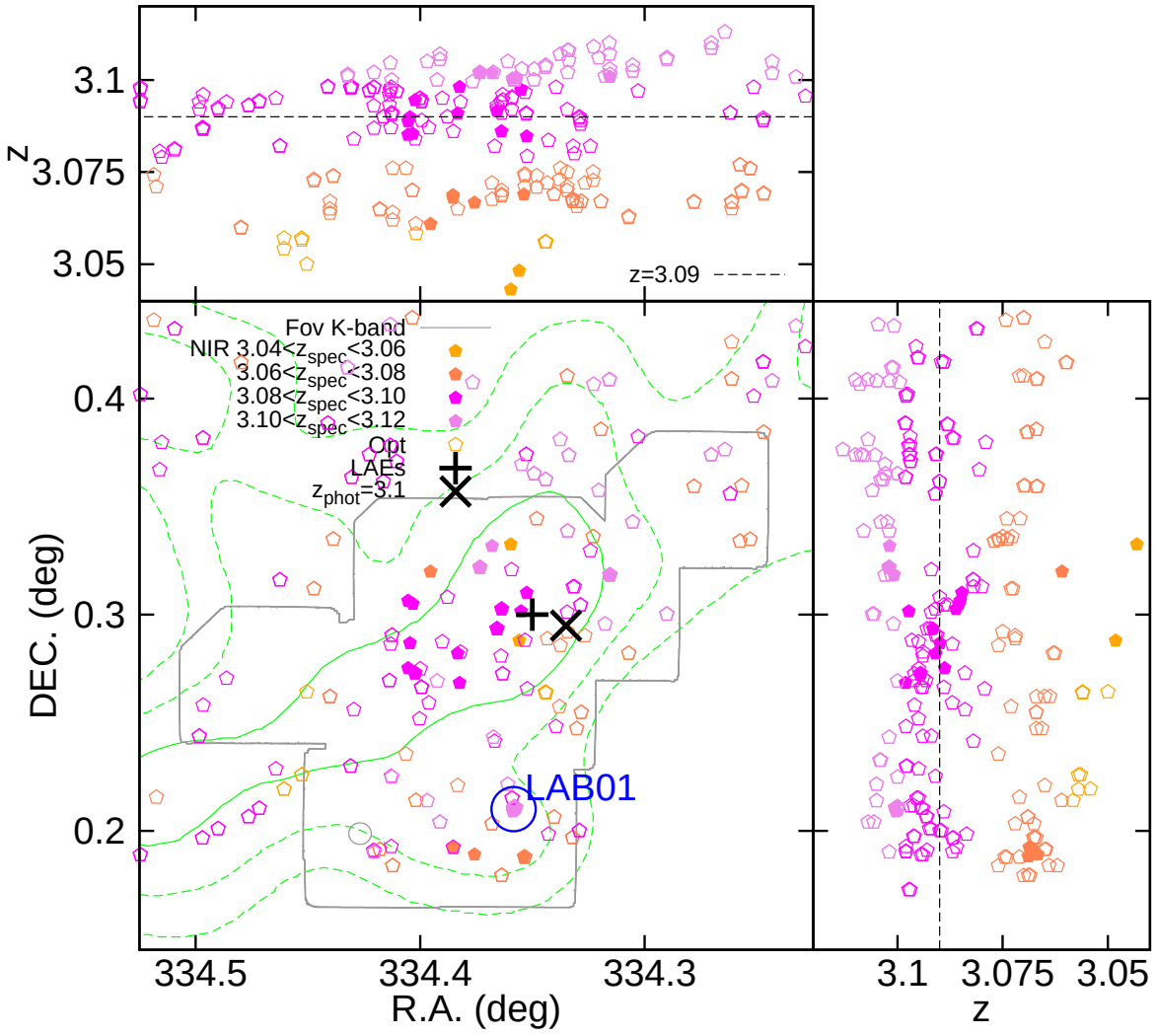

FIG. 13.— The spatial and redshift distribution of the objects. The objects spectroscopically confirmed the redshifts from our observation (NIR) are plotted with filled pentagons and those from archival observation (Optical) are plotted with blank pentagons. The color of the points shows the spectroscopic redshifts of the objects; $z = 3.04 - 3.06$ (orange), $z = 3.06 - 3.08$ (coral), $z = 3.08 - 3.10$ (magenta) and $z = 3.10 - 3.12$ (violet).

3.2. The galaxies in the SSA22 protocluster

As we have shown in the previous section, the SSA22 protocluster is likely to be one of the progenitors of the most massive clusters of galaxies in the current universe. Then the galaxies in the SSA22 protocluster should be the progenitors of the massive early-type galaxies in such environments.

In this section, we are going to discuss the galaxy evolution in the SSA22 protocluster; stellar mass assembly; emission line ratio; stellar population; AGN properties.

3.2.1. *The early formation of massive galaxies*

From the NIR spectroscopic observations, we confirmed many stellar mass selected galaxies in the protocluster. They may not have only large stellar mass but also large dynamical mass; They have larger velocity dispersion than LBGs. The line width and spatial extent of [O$_{\rm III}$] emission line is more similar to the *BzK* galaxies at $z \sim 2$, which are well characterized massive galaxies (§2.3.2). These values indicate the velocity dispersion and spatial extent of the gas and stars of galaxies (e.g., Erb et al. 2006b, since only the central regions of the objects are observable, the dynamical properties of the whole halo cannot be obtained).

There is a significant density excess of these K-selected massive galaxies in the SSA22 protocluster, which supported the early-formation of the stars in the protocluster. Following U12, we compare our results with the central region of Coma cluster, one of the most massive and well studied clusters of galaxies in the current universe. Although our spectroscopic observations is not complete, this may give lower limit on the stellar mass assembled in the SSA22 protocluster at $z = 3$.

Figure 14 is the number count of the galaxies in the SSA22 protocluster plotted against the stellar mass. The K-selected galaxies at $z_{\rm spec} = 3.04 - 3.12$ confirmed the redshifts by ours and archival spectroscopic observations are plotted in the figure. In comparison, we plot the number count of the galaxies with stellar mass $> 10^{10.5}$ M$_\odot$ in the central region of Coma cluster and half of that. This was converted from the luminosity function of the galaxies in the central $0''.8 \times 0''.6$ Mpc of Coma cluster obtained by de Propris et al. (1998), following U12. The galaxies in the protocluster plotted here are scattered at $\sim 1 - 3$ Mpc diameter region on surface but they may be gathered at central region at $z = 0$.

About half of the galaxies with stellar mass $> 10^{10.75}$ M$_\odot$ in Coma cluster was already formed. In U12, they compared the number density of the galaxies in Coma cluster with the galaxies in the SSA22 protocluster with stellar mass $10^{10.5}$ M$_\odot$ selected based on the photometric redshifts. They obtained that the stellar mass distribution of the SSA22 protocluster is similar to a third of the Coma cluster. The difference between our and their results may be due to the field to compare. As it is shown in Figure 12, the actual center of the protocluster may be at center of FoV of MOIRCS but in U12, they compared only south field of the density peak (M6, in U12).

The stellar mass assembly of the clusters of galaxies at $z \lesssim 1.5$ are well studied in other studies. E.g., de Propris et al. (1999), Lin et al. (2006) reported that there are no significant evolutions of the stellar mass function of the massive clusters from $z < 1$. It is also reported that some massive clusters at $z \lesssim 1.5$ show no significant evolutions in the massive ends of

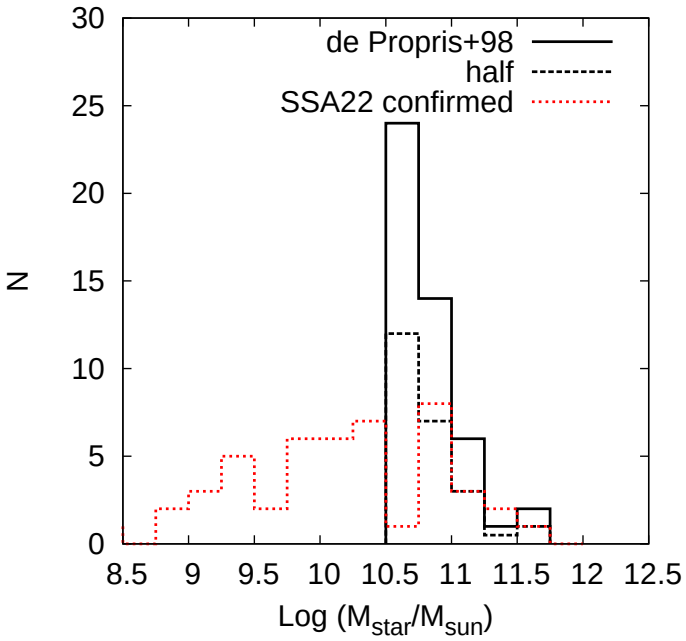

FIG. 14.— Stellar mass distribution of the galaxies in the protocluster. Red dashed line is the stellar mass distribution of the galaxies at $z_{\rm spec} = 3.04 - 3.12$ in the SSA22 protocluster. Black solid line is the stellar mass distribution of the galaxies at the central $0''.8 \times 0''.6$ Mpc region of Coma cluster (de Propris et al. 1998) for the stellar mass as low as $10^{10.5}$ $M_\odot$. Black dashed line is half of that.

stellar mass functions (e.g, Blakeslee et al. 2003; De Propris et al. 2007; Strazzullo et al. 2010). Their results suggest that most of massive galaxies in massive clusters have been formed as early as $z > 2$. We shows that in the SSA22 protocluster, which may be a progenitor of one of the most massive clusters, bulk of the stellar mass have already formed, strongly supporting their results. Further observations of well characterized massive clusters at $z > 1.5$ is needed to obtain further constraints on the stellar mass assembly histories in massive clusters. Note that our spectroscopic observations have not already completely followed up the protocluster galaxies and this is only a lower limit. Further spectroscopic observations are required to constrain the stellar mass assembly in the SSA22 protocluster.

3.2.2. *The emission line ratio*

Figure 15 shows the [O$_{\rm III}$]λ5007/Hβ line flux ratio versus stellar mass diagram of the protocluster as well as field galaxies, following Juneau et al. (2011). Lower limit values of the [O$_{\rm III}$]λ5007/Hβ ratio are plotted for the galaxies with no significant detection of Hβ. Note that the objects whose Hβ emission lines are out of the wavelength coverage are not plotted in the figure. The [O$_{\rm III}$]λ5007/Hβ ratio obtained with $HK500$ grism are not also plotted as they suffer from the contamination by OH airglow lines. We plot the star-forming galaxies and AGNs in the SDSS catalog (using the catalog provided by Tremonti et al. 2004) and the LBGs at $z \sim 3$ (Maiolino et al. 2008; Mannucci et al. 2009) for comparison.

The galaxies in our catalog have large [O$_{\rm III}$]λ5007/Hβ ratio, comparing with the local galaxies, which is similar to the other star-forming galaxies at $z = 2 - 3$. The HEROs distribute at massive end. Two of them are detected in X-ray and similar to local AGNs. One of the counterparts of LAB01 has $Log([{\rm O_{III}}]\lambda5007/{\rm H}\beta) = 0.21^{+0.29}_{-0.06}$, which is lower than those of the typical star-forming galaxies at $z \sim 3$.

The diagnostics of such collisionally excited emission lines give good constraints on the gas-phase metallicity, ionization state of the gas, dust extinction and radiation field of galaxies in the local universe (e.g., Baldwin et al. 1981). The most famous one is the Baldwin, Phillips and Terlevich (BPT) diagram (Baldwin et al. 1981), which allow us to classify AGNs by using [O$_{\rm III}$]λ5007/Hβ and Hα/[N$_{\rm II}$]λ6584 emission line diagnostics.

At high redshift, the available emission lines are very limited. Juneau et al. (2011) tried to classify AGNs by using [O$_{\rm III}$]/Hβ versus stellar mass diagram, called Mass Excitation (MEx) diagram. They successfully classified the AGNs at $0.3 < z < 1$ which have large [O$_{\rm III}$]/Hβ ratio and are hosted in massive galaxies. Star-forming galaxies have typically smaller [O$_{\rm III}$]/Hβ ratio and have wide-spread range of stellar mass. It is hard to classify, however the high redshift galaxies from MEx diagram since star-forming galaxies also have high [O$_{\rm III}$]/Hβ ratio.

In addition to difficulty to obtain emission line ratios ideally, it is also difficult to apply the similar emission line diagnostics in the local universe to the galaxies at high redshift. It is reported that the star-forming galaxies at high redshift typically have higher [O$_{\rm III}$]/Hβ ratios than those in local universe (e.g., Erb et al. 2006a; Maiolino et al. 2008; Mannucci et al. 2009; Yabe et al. 2012; Kewley et al. 2013b). Referring to the theoretical prediction by Kewley et al. (2013a), a harder ionizing radiation field and/or larger electron density move galaxies above normal star-forming abundance sequence on the BPT diagram. Whether a larger ionization parameter raises or lowers the [O$_{\rm III}$]/Hβ line ratio may depend on the metallicity of the galaxies.

If the counterpart of LAB01 has a similar ionizing radiation parameter, ionizing radiation field and electron density as other star-forming galaxies in the protocluster, while this object may have similar or higher SFR (may give similar or harder ionizing radiation field) and electron density of other objects, its chemical enrichment is a plausible reason for lower [O$_{\rm III}$]/Hβ line ratio.

Except for LAB01, we found no significant difference in the [O$_{\rm III}$] λ5007/Hβ line ratios of the protocluster galaxies from those of the field galaxies. On the other hand, Kulas et al. (2013) reported that the metallicity of the protocluster galaxies at $z \sim 2$ show various

values regardless of the stellar mass while field galaxies follow the well established trend in mass-metallicity relation at that epoch. Further spectroscopy for [O$_{\rm II}$]λ3727 emission line is required to constrain its metallicity.

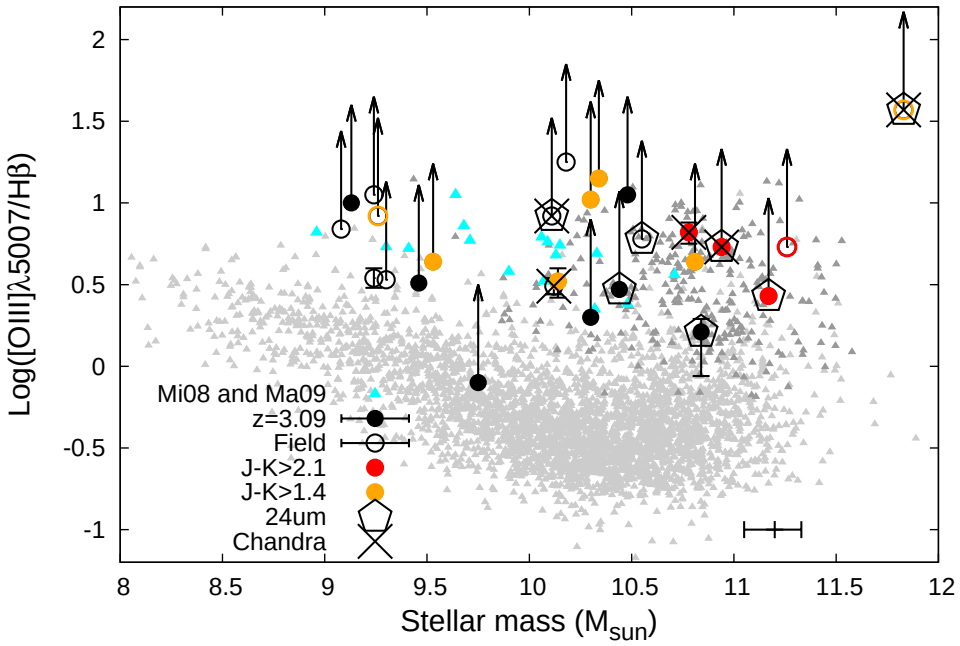

FIG. 15.— [O$_{\rm III}$]/Hβ ratio versus stellar mass of the galaxies. Filled circles are the galaxies at $3.04 < z_{\rm spec} < 3.12$ and blank circles are field galaxies at $2.9 < z_{\rm spec} < 3.4$ in our sample. Black circles are the galaxies with $J-K < 1.4$, orange circles are those with $1.4 \leq J-K < 2.1$ and red circles are those with $J-K \geq 2.1$. Cyan triangles are the comparison samples at $z \sim 3$ (Maiolino et al. 2008 and Mannucci et al. 2009). Light gray points are SDSS galaxies. Dark gray points are SDSS galaxies which classified as AGNs (Tremonti et al. 2004).

3.2.3. *The stellar populations of the protocluster galaxies*

Significant fraction of the DRGs and HEROs in the SSA22 field are certainly the members of the protocluster. It supports the our previous photometric studies in which we reported the density enhancement of the DRGs and HEROs in the SSA22 field (U12; K13). We also reported that there are a notable number of the quiescent DRGs with $z_{\rm phot} \sim 3.1$ in the SSA22 field while there are no such galaxies in the general field. The fraction of the quiescent galaxies in the SSA22 protocluster can be up to 50% of the massive galaxies with $M_{\rm star} > 10^{11}$ $M_\odot$ (K13).

In the meanwhile, what are the origins of the red galaxies which are spectroscopically identified as the protocluster members? We here investigate the properties of these red galaxies based on the SED fittings described in § 3.3.3. First of all, as we discussed in § 3.3.3, the contributions of the [O$_{\rm III}$] emission lines to the $J-K$ colors are negligible. Then the density excess of the DRGs and HEROs may be actually due to their red continuum.

Interestingly, the reddest galaxies in the protocluster ($J-K > 2.4$) have the SEDs dominated by old stellar populations. Figure 16 are the best-fit SEDs and provability distributions of the five protocluster galaxies with $J-K > 2.4$. All of them are well fitted with the models with old stellar populations. Four out of the five galaxies with $J-K > 2.4$ are fitted with the models with quiescent star-formation ($\tau = 0.2-0.3$, $1-1.7$ Gyr old and sSFR < 0.2 Gyr^{-1}) with $> 65\%$ confidence level. The rest one is the object confirmed with the Balmer/4000Å breaks described in §2. The confidence level of its best-fit SED is low due to its very faint rest-frame UV spectra but the degeneracy with dusty starburst models is quite small; it has red rest-frame UV to optical color but blue optical to NIR color which are not expected for dusty starburst galaxies. Their stellar mass values range from $10^{10.8}$ to $10^{11.3}$ $M_\odot$. From these above, although the spectroscopic observations are still limited, there are already a remarkable number of the galaxies similar to local massive early-type galaxies in the SSA22 protocluster at $z = 3$.

Note that the definition of the quiescent galaxies are slightly different from those we selected by using two color diagram Figure 4, in which we adopted the conservative selection criteria to avoid the contamination of the dusty starburst galaxies. The stellar mass measurements are also different while we adopt the Chabrier IMF here.

The four quiescent galaxies confirmed with [O$_{\rm III}$] λ5007 are also detected in X-ray, which must be responsible to their [O$_{\rm III}$] λ5007 emission. There are no AGN features in their rest-frame UV to NIR SEDs, as they may be buried in the stellar light, as is often the case for the AGNs at high redshift (e.g., Yamada et al. 2009). It is also supported from the MEx diagram in which they have similar distribution as local AGNs. Number of the whole quiescent galaxies we found from the color diagram (Figure 4) with 10^{11} $M_\odot$ at $2.6 < z_{\rm phot} < 3.6$ was 9. But the selection criteria is not the same. Instead, the number of the galaxies with $J-K > 2.4$ (all of them have $2 < z_{\rm phot} < 4$) in the SSA22 field is 11 and the AGNs take at least a third of the reddest galaxies in the protocluster. On the other hand, four out of 11 AGNs in the SSA22 protocluster shows the SEDs of quiescent galaxies. Then there may significant contribution of the AGNs to the quiescent galaxies in the SSA22 protocluster. It suggests that the AGNs may quench the star-formation to form such massive quiescent galaxies at high redshift. The high fraction of the AGNs in the cluster of quiescent galaxies at $z = 1.61$ was also reported in Tanaka et al. (2013). It was also reported that the candidate

quiescent galaxies at $z > 4$ found by Straatman et al. (2013) are detected in Herschel, which may be responsible to the obscured AGNs. We are going to discuss the AGNs in details in the next section.

Such massive quiescent galaxies are found even at $z > 2$ by recent deep NIR imaging and sometimes spectroscopic observations (e.g., Daddi et al. 2005; van Dokkum et al. 2008; Gobat et al. 2012; Straatman et al. 2013). The association of the clusters of quiescent galaxies in the protocluster at up to $z \sim 2$ are also reported (Zirm et al. 2012; Strazzullo et al. 2013). It may be for the first time to show that such massive quiescent galaxies certainly hosted in the protocluster at the redshift as high as $z = 3$. Our results also support our previous results from the imaging observations that there are significant density excess of the quiescent galaxies in the SSA22 protocluster.

Four out of the six quiescent galaxies associate the LABs or an SMG. It suggests that they will experience further major mergers.

There are also other six DRGs with $1.4 < J - K < 2.4$ in the protocluster. Due to their faint spectra, confidence levels of their best-fit SEDs are not enough high and the degeneracy of the models are too large to obtain their robust SED parameters. But they have redder colors than those of typical LBGs, suggesting more obscured star-formation and/or older stellar populations of them. At least, one of them may be a heavily dust obscured galaxy while it is detected in the 24 μm and also located within the beam size of an 1.1-mm source, AzTEC 99. Such IR luminous galaxies may be dusty starburst galaxies with SFR several $100 - 1000$ $M_\odot$ yr^{-1}, supporting active formation of the galaxies in the SSA22 protocluster.

Figure 17 and 18 are the color diagrams of the protocluster galaxies.

Figure 17 shows the $J - K$ colors of the K-selected galaxies in the SSA22 field. The objects plotted with blue open circles are the K-selected galaxies with $2.6 < z_{\rm best} < 3.6$ and with red filled circles are the protocluster galaxies with $3.04 < z_{\rm spec} < 3.12$. We indicate the expected colors for the galaxies on passive evolution which were formed by single burst at $z_{\rm f} = 4$ and 5 with solid and dashed lines. There are a number of the galaxies with $2.6 < z_{\rm best} < 3.6$ which have the colors consistent with these models while not so many such red galaxies are seen in the general field (e.g., Kodama et al. 2007). They may be the nascent red sequence although the color-magnitude relation is not so tight as local relation while they may be still young and there may be also the degeneracies with the red galaxies due to dusty starburst. The quiescent galaxies described above have reddest colors among the protocluster galaxies and their formation epoch given from the diagram is $z_{\rm f} \gtrsim 6$, consistent with those obtained from the SED fittings.

Figure 18 is the two color diagram similar to Figure 4 but for the galaxies confirmed to be the members of the protocluster. With this diagram, we can avoid the degeneracy of the red colors from old ages and dusty starbursts, which can not be separated from the $J - K$ color diagram. It is clearly seen that we probed the protocluster galaxies with much different colors as those confirmed from the optical spectroscopic observations in archive.

The quiescent galaxies described in this section have the colors consistent with single burst model with 0.5-1 Gyr while some of them are slightly out of the color criteria described in §1.1.4 (That was conservative selection to avoid the contaminations). Since they are better fitted with exponentially decay models ($\tau = 0.2 - 0.3$) with the age 1-1.7 Gyr, they show bluer colors than those expected for the single burst model with the age 1-1.7 Gyr. Note that two quiescent galaxies confirmed in our observations (two X-ray detected HEROs below the

single burst sequence) were not plotted in Figure 4 since they have the photometric redshifts slightly out of the selection criteria, $2.6 < z_{\rm phot} < 3.6$.

The counterparts of AzTEC99 detected in $24_m u$m shows very red colors in both $i' - K$ and $K - [4.5]$, supporting that this object is a dusty starburst galaxy. DRGs have the redder colors than those of normal star-forming galaxies in the protocluster. They show the colors similar to those of the dusty star-forming galaxies. Most of the 24 μm detected objects also show red colors.

From these above, we conclude that it is just the formation epoch of the galaxies in the SSA22 protocluster while there is already some massive quiescent galaxies. The quiescent galaxies may be formed stars at > 1.5 Gyr and passively evolving. Then bulk of the star of them may be formed at $z > 4$, suggesting the prolonged peak of star-formation activities.

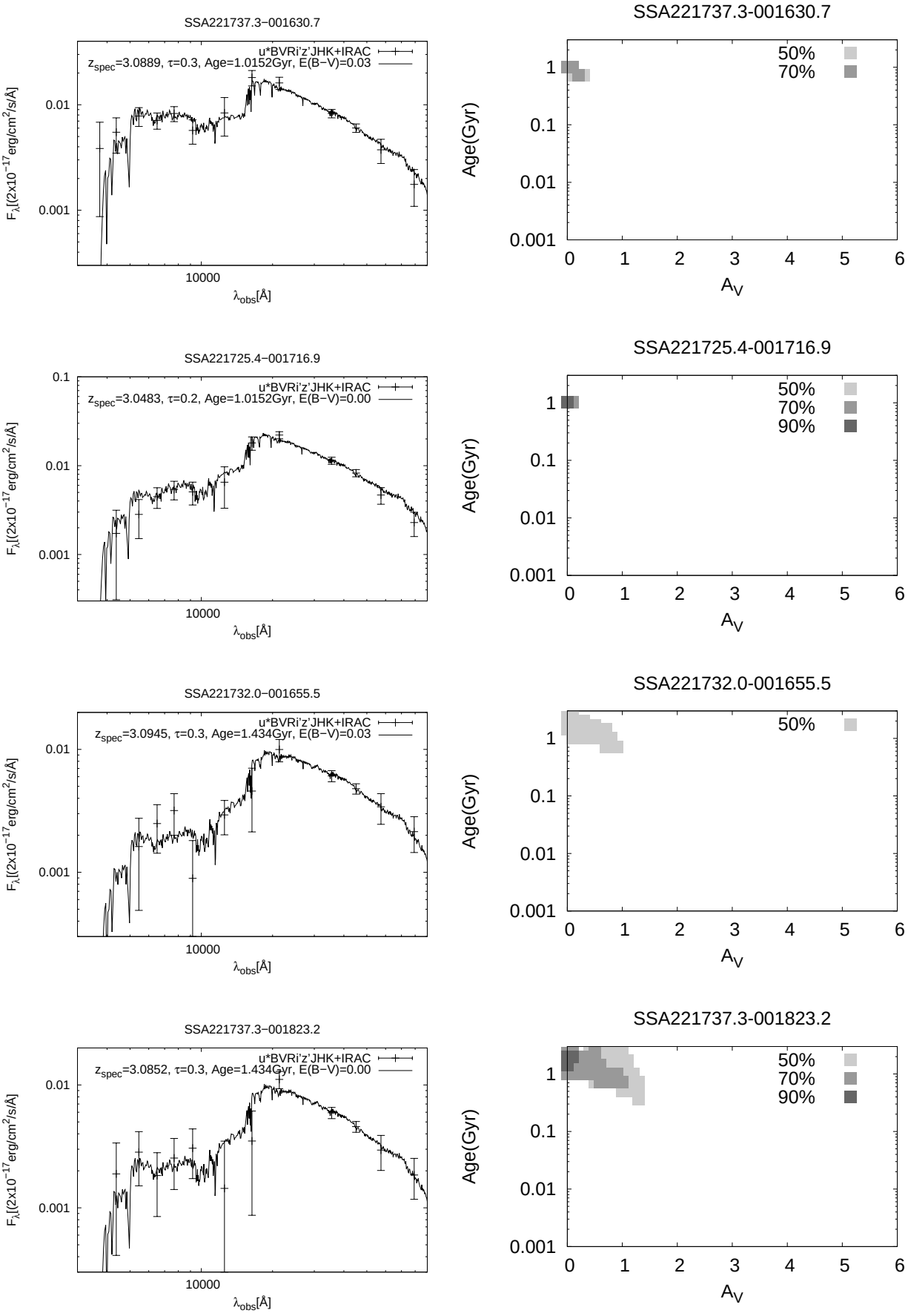

FIG. 16.— *Continued.*

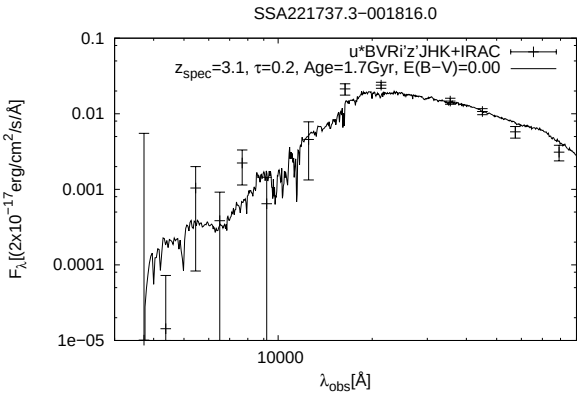

FIG. 16.— The best fit SED of the protocluster galaxies with $J - K > 2.4$.

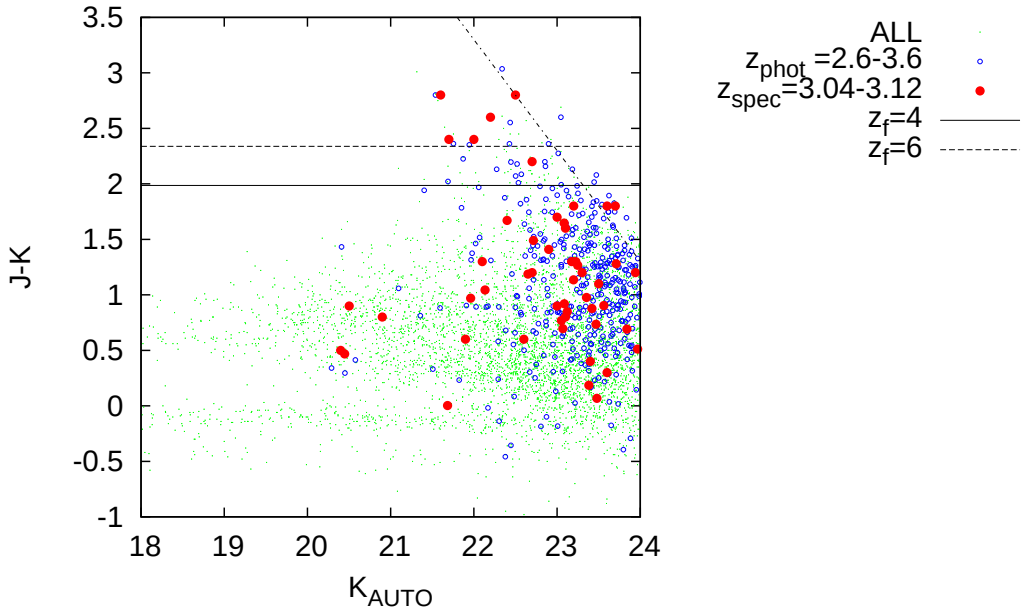

FIG. 17.— $J-K$ color diagram of the galaxies in the SSA22 field. X-axis of the color diagram is the K-band total magnitude (MAG_AUTO) of the galaxies. Red filled circles are the objects confirmed as the protocluster members. The blue unfilled circles are the objects with $2.6 < z_{\rm phot} < 3.6$. The green dots are the whole objects detected in K-band in the SSA22 field. Tilt line is the limit for $J-K$ colors defined from the detection limit of J-band (We plot median limit $J = 25.3$ ($at2\sigma$) while detection limit are $J = 25.7-25.2$ ($at2\sigma$), not uniform in the FoV of MOIRCS.). The solid and dashed horizontal lines indicate the $J-K$ colors expected for the galaxies formed with single burst at $z_{\rm f} = 4$ and $z_{\rm f} = 6$.

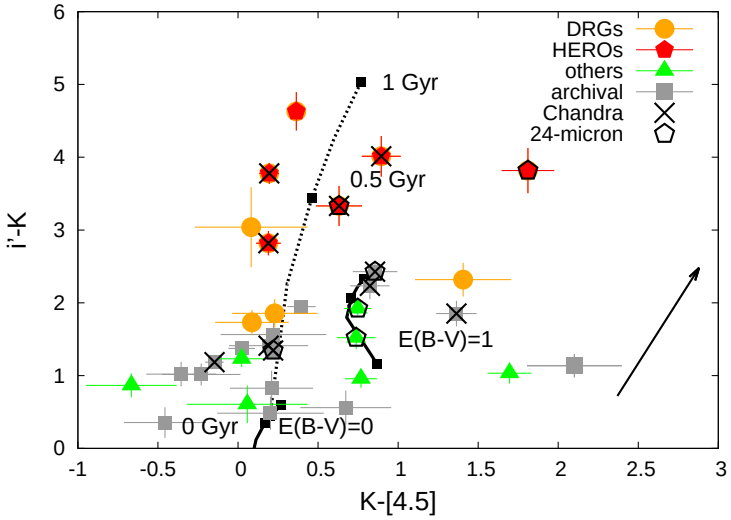

FIG. 18.— $i'-K$ v.s. $K-[4.5\mu{\rm m}]$ diagram of the galaxies confirmed as the protocluster members. The red pentagons are HEROs, the orange circles are DRGs and green triangles are other objects confirmed the redshifts to be at $z = 3.04-3.12$ from our NIR spectroscopic observations. The gray squares are the objects confirmed the redshifts to be at $z = 3.04-3.12$ from the archival optical spectroscopic observations. The objects detected in K and 4.5 μm are plotted here. The black pentagons are the objects detected in 24 μm and the black crosses are those detected in *Chandra* X-ray. The models plotted here are similar to Figure 4

3.2.4. *The AGNs in the protocluster*

The overdensities of the X-ray detected LBGs, LAEs (Lehmer et al. 2009b) and the K-selected galaxies at $2.6 < z_{\rm phot} < 3.6$ (K13) have also been reported in the SSA22 field. The density enhancement of AGNs may be originated in two; overdensity of the massive galaxies and enhanced AGN activities.

First case is strongly supported from several clues. It is reported in Lehmer et al. (2009b) at the SSA22 protocluster field and also Digby-North et al. (2010) at the z=2.3 protocluster field that the LBGs and LAEs in the protoclusters are more massive than the field galaxies at same redshift. It is also supported by this study. As we reviewed in Table § 1.3 (K13), there are more many K-band detected, namely massive LAEs in the SSA22 protocluster. As we discussed in § 3.1 in this chapter, there are significant density excess of the K-selected, namely stellar mass selected galaxies in the SSA22 protocluster. Figure 22 is the surface and redshift distributions of the AGNs in the SSA22 protocluster. Similar to the distribution of the galaxies in Figure 13, AGNs also clustered at eastward the center and at $z \approx 3.09$. Supporting the density excess of AGNs associating with the massive galaxies formed at the core of the protocluster.

There are some but weak clues supporting the second case; We have also reported that there are more MIR luminous and optically luminous AGNs, which are dusty but very energetic AGNs among the protocluster galaxies selected from the photometric redshifts in the SSA22 protocluster (§ 1.4 of this chapter and see also K13), although the number is small, which supports the latter scenario. The fraction of AGNs among the galaxies with stellar mass $> 10^{11}$ $M_\odot$ is $\sim$ 50% (3/6) adopting the Chabrier IMF and $\sim$ 50% (8/17) adopting the Salpeter IMF while it is reported 30% for the galaxies with stellar mass $> 10^{11}$ $M_\odot$ at $2 < z_{\rm phot} < 4$ in Yamada et al. (2009). The fraction of the AGNs is higher but there remain large uncertainties since the spectroscopic observations are not complete, the emission lines used to confirm the redshifts (Lyα and [O_{III}]) can be enhanced by AGN activities and sample can be biased to AGNs. Further observations are needed to settle this issue.

On the other hand, the properties of the AGNs in the protocluster are also interesting to study their roles in the galaxy formation since the AGNs feedback have become very essential in formation of massive early-type galaxies in the recent semi-analytic simulations (e.g., Croton et al. 2006; Bower et al. 2006).

Thanks to the deep X-ray observations by *Chandra* and the several spectroscopic surveys, various type of the AGNs were confirmed in the SSA22 protocluster. The depth of the *Chandra* data corresponds to $\sim 10^{43}$ erg s^{-1}. Then the AGNs with moderate luminosity are detectable. The eight X-ray sources detected by *Chandra* were confirmed from the archival observations and three such are newly confirmed from our observations. The AGNs at $z_{\rm spec} \sim 3$ in archival data in the SSA22 field are, the LBGs and LAEs matched with the *Chandra* source catalog or the objects confirmed from the spectroscopic surveys like SDSS and VVDS. Then the bright AGNs with flat and featureless SEDs, which are missed from the selection based on the photometric redshifts, are also included in our sample.

Figure 19 shows the observed and best-fit SEDs of the AGNs confirmed to be the protocluster members by archival observations. The best-fit SEDs of the AGNs in the protocluster confirmed from our observations are shown as top four objects of Figure 32. The SED mod-

eling are performed with similar templates as we described above. All the AGNs are bright objects with $K_{\rm AB} = 20.5 - 23$ and with small errors on their observed flux values.

The SEDs of them are the composites of the stellar and AGN components. There are significant Lyman break (and also Balmer/4000Åbreaks) in the spectra of the stellar components. The rest-frame UV to IR SEDs of the several type QSOs are shown in Polletta et al. (2007). At the wavelength plotted here, which correspond to rest-frame UV to NIR, type 1 QSOs show flat SEDs where F_λ decrease with the wavelength. Type 1 QSOs also show strong Lyα emission line. If the objects are similar to type 2 QSOs, they have the SEDs more similar to galaxies but show excess at the wavelength $> 5.8\mu$m.

The objects confirmed by our observations (Figure 16) and those plotted in the top panel of Figure 19 have the SEDs dominated by the stellar components. The SEDs of the objects with blue and red symbols show rise at longer wavelength. There are no significant AGN feature in the SEDs of the galaxies plotted in Figure 16 and green symbols in top panel of Figure 19 while the SEDs of the objects blue and red show rise at longer wavelength. The objects plotted with blue and red are well fitted with the SEDs of the star-forming galaxies. On the other hand, the SEDs of the objects plotted in the bottom panel of Figure 19 are dominated by the AGN components. They are similar to the SEDs of type 1 QSOs since they have flat SEDs and significant Lyα emissions are detected for all of them. Since they are also bright in rest-frame UV, the equivalent width of the Lyα emission line are not so large ($\sim 30 - 150$Å) although they have strong Lyα emission lines.

Figure 20 shows the X-ray luminosity at 2-10 keV v.s. stellar mass distribution of the AGNs and Figure 21 shows the specific AGN activities of them following Yamada et al. (2009). The X-ray luminosity at 2-10 keV was obtained from the hard-band flux (2-8 keV) adopting the relation $f_\nu \sim -0.7$ to obtain the K-correction factor. When an object is not detected in hard-band, we use full-band flux value (for one object). Since the hard-band flux is not suffering from the heavy dust attenuation, this value may be closer to the intrinsic X-ray luminosity values. The detection limit at hard band corresponds to $\sim 1 \times 10^{43}$ erg s^{-1} for the objects at $z = 3.09$. We classify the objects as quiescent, star-forming galaxies and AGNs.

The horizontal lines in Figure 21 indicate the specific AGN activities in the case of $R_{\rm edd} = 0.01, 0.1$ and 1, following Yamada et al. (2009); Assuming the bolometric to at 2-10 keV fraction of the X-ray emission, ϵ_X, the ratio of the bolometric to the Eddington luminosity of the AGN, $R_{\rm edd}$ and the observed X-ray luminosity can be connected to the black hole mass as

$$L_X = 4\pi G m_p c M_{\rm BH} \epsilon_X R_{\rm edd}$$
$$= 2 \times 10^{43} (M_{\rm BH}/10^8 M_\odot)(\epsilon_X/0.01)(R_{\rm edd}/0.1) ergs^{-1}$$

Adopting $\epsilon_{\rm X} = 0.01$ and local value of $\rm M_{BH}/M_{sph} = 0.002$, we can obtain the specific AGN activity values at given $R_{\rm edd}$.

Since it is difficult to obtain the stellar mass of the AGNs whose SEDs are dominated by the AGN components (blue triangles), we plot such AGNs at stellar mass 10^{11} $\rm M_\odot$, which is most massive at that epoch. The $L_{\rm X}/\rm M_{star}$ values of them are nearly upper limit values. On the other hand, even for the AGN components are dominant, the SEDs of them are not completely flat and slightly raise at 1-2μm wavelength (Figure 19). There may be the stellar components which are not dominant but as significant as the AGN components with brightness of several 10^{-18-19} erg cm^{-2} s^{-1} Å^{-1} at $1 - 2\mu$m, which corresponds to the stellar mass of several 10^{10} to 10^{11} $\rm M_\odot$.

The AGNs whose SEDs are dominated by the stellar components have lower X-ray luminosity than the AGNs without dominant stellar components. The quiescent galaxies show X-ray luminosities as low as local bright Seyfert galaxies while those of SFGs are higher. The X-ray luminosities divided by the stellar masses are the specific AGN activities (Figure 21). For the AGNs with dominant stellar components, more massive galaxies have smaller AGN activities. The specific AGN activities of the quiescent galaxies are also smaller. Their specific AGN activities corresponds to the Eddington ratio $R_{\rm edd} = 0.1$, similar to or slightly higher than local massive galaxies. The SFGs and AGNs have larger specific AGN activities.

It sounds strange that the quiescent galaxies are the most massive galaxies at that epoch but have lower X-ray activities, assuming the local correlation of the mass of super massive black hole (SMBH) with the stellar mass of bulge. Similar trend of the stellar mass to AGN activity was reported in Yamada et al. (2009) from larger sample with deeper *Chandra* data. The properties of the host galaxies and the strength of the AGNs are studied in several studies. It is reported that the host galaxies of the X-ray sources at $z \sim 1$ have inactive star formation activities (Mullaney et al. 2012; Rosario et al. 2012; Rosario et al. 2013). The age of the stellar population of host galaxies is also reported to be correlate with the AGN activities. Yamada et al. (2009) reported that the higher AGN activities in the host galaxies with young stellar populations. Jones et al. (2013) reported that the galaxies with larger D(4000), which is the indicator of the age of galaxies, have lower AGN activities at $z = 1-2$.

Two scenarios can be considered to explain the lower activities of the massive galaxies; the mass of SMBHs are independent of the stellar mass of the host galaxies; the massive galaxies have relatively lower AGN activity. The former scenario is not favored since there is no AGNs with small stellar mass. Then we favor second scenario in which relative mass accretion rate decreases for massive galaxies. In this scenario, the AGN become active with stellar mass growth, come around the peak AGN activity and eventually come down to local luminosity. Since massive quiescent galaxies in the SSA22 protocluster have relatively weak AGN activities, which is similar to or slightly higher than local massive galaxies, they are likely to be the final phase in this scenario.

This supports the formation of massive quiescent galaxies thorough quenching of the starburst by AGN feed-back. The feedback from AGNs can eject gas from host galaxies to shut down star-formation activities and also keep quiescent preventing gas cooling and accretion. Then the galaxies move and keep on the red sequence via this process. By introducing the AGN feedback, the formation of bright galaxies are restricted and actual luminosity function of the galaxies is well reproduced in the cosmological numerical simulations (e.g., Croton et al. 2006). It is also effective to form massive quiescent galaxies early, as found in the SSA22 protocluster. The contribution of the AGN feed-back to form massive quiescent galaxies at high redshift is also suggested in Straatman et al. (2013), in which they reported the presence of dust obscured AGNs among the candidate quiescent galaxies at $z \sim 4$.

It may also happen that the correlation of decline of the AGN activities and star-formations are due to the exhauted of gas. It may be not likely the case for our sample since most of the quiescent galaxies we identified may be one of the counterparts of LABs and SMGs. There should be a plenty of gas remaining around them, although we need more high resolution imaging and also spectroscopy of the gas around them.

3.3. Conclusion

From both the density enhancement and the dynamical mass obtained by the NIR spectroscopic and imaging observations, the SSA22 protocluster is well characterized as the plausible progenitor of most massive clusters in the current universe as it was also suggested from the optical observations. There is no such protoclusters at $z > 2$ which characterized better than this protocluster.

Large stellar mass, about half of the center of Coma cluster, is already formed in the SSA22 protocluster. We also confirmed the presence of massive quiescent galaxies in the SSA22 protocluster. This may be for the first time to confirm the association of massive quiescent galaxies with the protocluster at $z > 3$, which may be the progenitors of the massive early-type galaxies in the current massive clusters. The formation of galaxies still active while there are also dusty starburst galaxies confirmed in the protocluster. These support the rapid formation of massive galaxies in such high density region predicted by the cosmological numerical simulations.

Most of massive quiescent galaxies confirmed are AGNs with similar X-ray luminosity as local massive galaxies. They show relatively lower activities than the other AGNs in the protocluster. This suggests the contribution of the early formation of massive quiescent galaxies via quenching of the star-formation activities by AGN feedback.

On the other hand, we also spectroscopically confirmed the multiple stellar components of the LABs and SMGs. They may be multiple mergers of the stellar components at early-phase of the formation of massive early-type galaxies, predicted in the cosmological numerical simulations.

In the next Chapter, we finally discuss these objects with multiple stellar components to study the formation scenario of massive early-type galaxies.

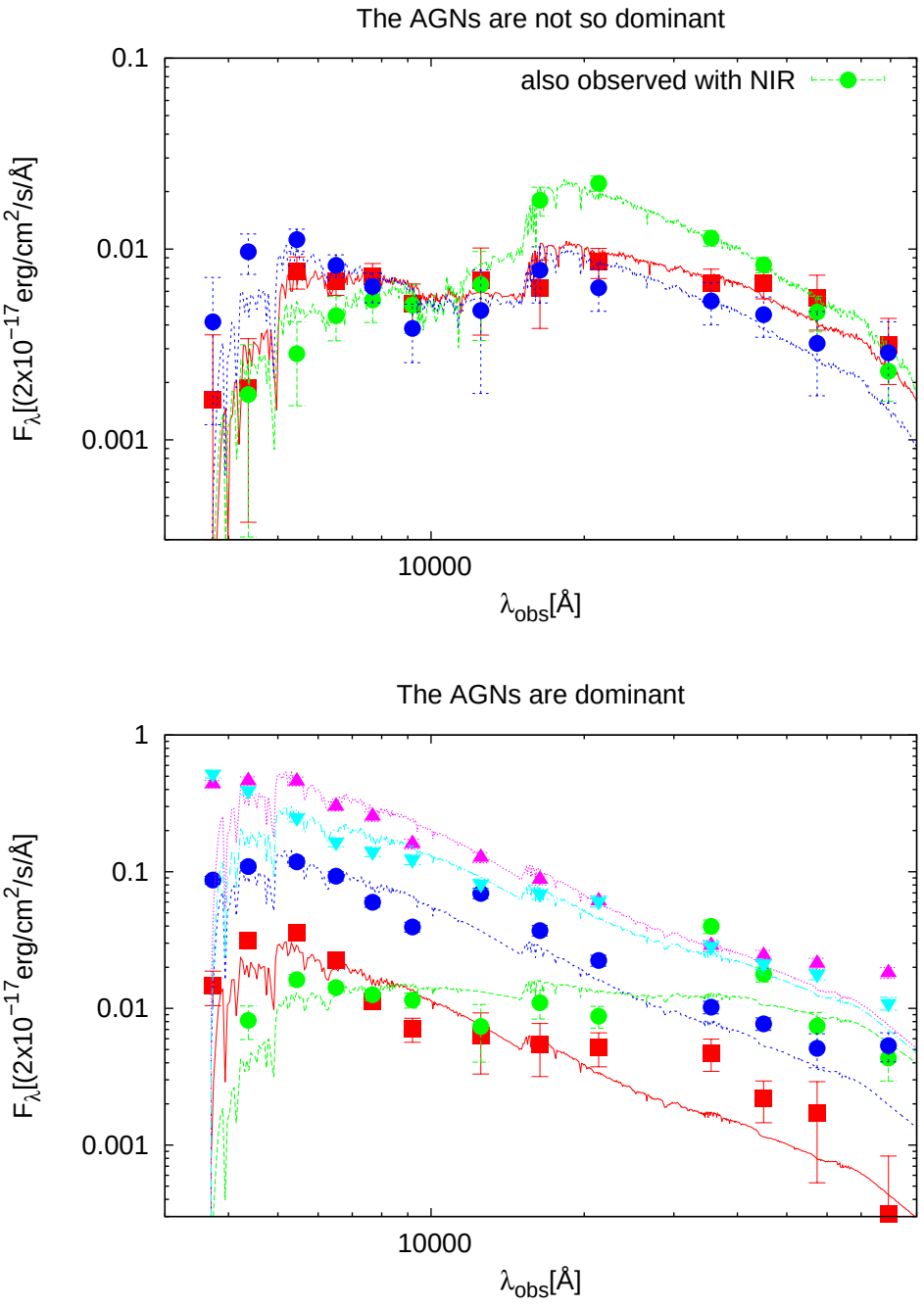

FIG. 19.— The SEDs of the AGNs in the protocluster. The points are the observed flux values and the lines are best-fit SED models of each galaxies. Only the SED models for galaxies (Bruzual & Charlot 2003) are assumed. The objects in top panel are the AGNs well fitted with the SED models of the galaxies. The object plotted with green line is the AGN also obtained the redshift from our NIR spectroscopic observations. In the bottom panel, we plot the AGNs whose SEDs are dominated by the AGN components and not well fitted with the template SED of the galaxies.

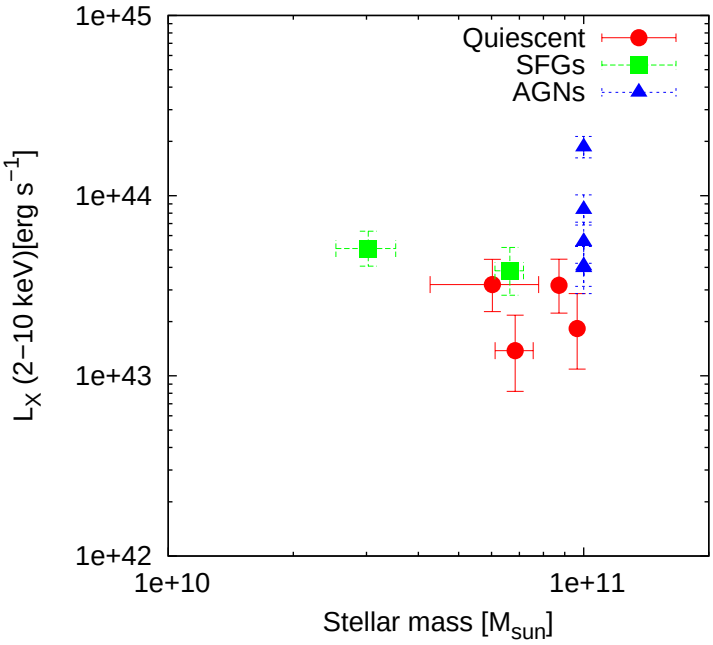

FIG. 20.— X-ray luminosity at 2-10 keV v.s. stellar mass of the AGNs in the protocluster. Red filled circles are the AGNs with the SEDs dominated by stellar components of quiescent galaxies. Green filled squares are those with the SEDs dominated by stellar components of star-forming galaxies. Blue filled triangles are those with the SEDs dominated by AGN components. Since it is difficult to measure the stellar mass of the objects with the SEDs dominated by AGN components, we plot them at stellar mass 10^{11} $M_{\odot}$.

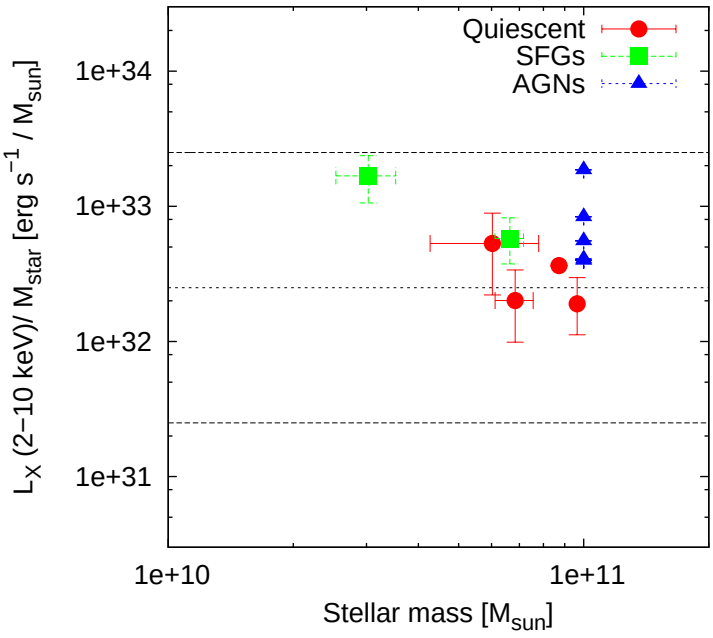

FIG. 21.— Specific X-ray activity (X-ray luminosity divided by the host stellar mass) v.s. stellar mass of the AGNs in the protocluster. The points are same as Figure 20. The dotted line indicates the specific AGN activity in the case of $M_{BH}/M_{star} = 0.002$, $\epsilon_X = 0.01$, and $R_{edd} = 0.1$. The upper and lower dashed lines are those for $R_{edd} = 1$ and 0.01, respectively (following Yamada et al. 2009).

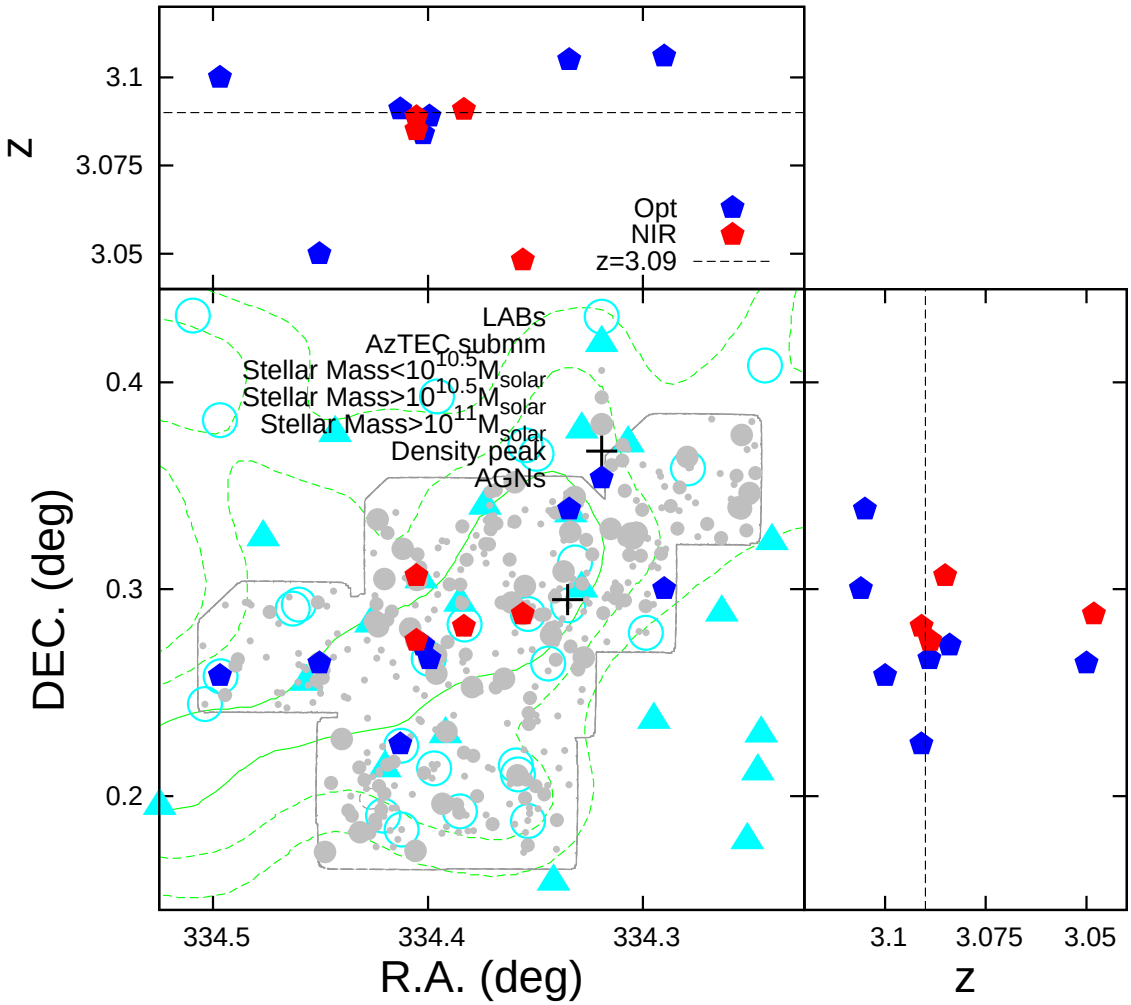

FIG. 22.— The sky distribution of the AGNs at $z = 3.09$ in the SSA22 field. The AGNs confirmed from the NIR spectroscopic observations are shown with red filled pentagons and the AGNs confirmed by the optical spectroscopic (archival) observations are shown with blue filled pentagons. The redshift distribution of them is shown in right and top panels. The gray points are the distribution of the K-selected galaxies with $2.6 < z_{\rm best} < 3.6$.

Chap.3. MULTIPLE MERGING GALAXIES

1. MULTIPLE MERGING GALAXIES

In this section we are going to discuss the objects which are likely to be massive early-type galaxies on-going formation, namely "multiple merging galaxies".

To begin with, we review the formation scenarios of elliptical galaxies in theory.

The classically proposed formation scenario of elliptical galaxies is monolithic collapse of gas cloud (Eggen et al. 1962). In this scenario, the stars of galaxies formed intense starburst at high redshift ($z \gtrsim 5$) and passively evolve. The massive spheroids are formed, the tight fundamental relations of elliptical galaxies e.g., color magnitude relations and the evolutions of these relations with redshift are also well explained by this scenario (e.g., Kodama et al. 1998).

On the other hand, major mergers of gas rich disk galaxies can also form massive elliptical galaxies (Toomre & Toomre 1972). This scenario is supported from several observational clues; The mergers and interactions of the galaxies are frequent at high redshift, suggesting that there are notable contributions of mergers to the galaxy formations. It is also observed that elliptical galaxies become bluer with the morphological disturbance. The signs of recent star formation activities of them at local and high redshift are also reported. In the cosmological numerical simulations of the structure formation in the CDM universe, massive galaxies are naturally formed via a number of mergers. However, it is also reported that the observed starburst of galaxies due to mergers are insufficient to form the whole stellar mass of elliptical galaxies in the current universe.

The actual formation scenario should not only be responsible to the formation the galaxies with the observed properties of individual massive early-type galaxies but also their number density and those evolution. These are well reproduced in the recent semi-analytic simulations (e.g., the simulations based on Millennium simulation; Springel et al. 2005). In such cosmological numerical simulations, elliptical galaxies are not only formed thorough hierarchical mergers but also in situ disk instabilities (e.g., Croton et al. 2006; De Lucia et al. 2006). It is reported in De Lucia et al. 2006 that the ratio of of the elliptical, spiral and lens galaxies become more close to the observed values if the formation of elliptical galaxies via disk instabilities are also included.

The galaxy formation via disk instability is generally proposed as the formation scenario of disks and bulges of late-type galaxies. Clumps are formed from the fragmentation of gaseous disk due to gravitational instabilities supported by accretion of cold gas and fall into the central bulge (e.g., Noguchi 1999). The clumps are destroyed to form the disks during in-fall, or if survive, merged with the central bulge. This process have been proposed as a formation scenario of clumpy disk galaxies (e.g., Cowie et al. 1995; Elmegreen et al. 2004; Bournaud et al. 2007) and clump clusters (e.g., Elmegreen & Elmegreen 2005) observed at $z > 1$. The sizes of clump clusters, which are thought to be early-phase of clumpy disk galaxies, are $\lesssim 20$ kpc, not so different from those of small LABs. If clumps survived are dominant, it may require continuing accretion of cold gas (e.g., Dekel et al. 2009b), the spheroids are formed. In this mode, the clumps merge into the central bulge with the timescale $\lesssim 0.5$ Gyr. Gas rich major mergers of clumps occur and can produce compact ellipticals, which are observed at $z > 2$ (e.g., Daddi et al. 2005; Trujillo et al. 2006; van Dokkum et al. 2008). Massive galaxies with $\sim 10^{11}$ $M_\odot$ can be also formed as early as $z > 2$

in this scenario by the process so-called cold accretion; Such massive galaxies are hosted in the massive dark matter halo with mass $> 10^{12}$ $M_\odot$ above the mass threshold for virial shock heating and cold gas are heated before accretion into the inner galaxies (e.g., Birnboim & Dekel 2003; Dekel & Birnboim 2006). But it is suggested by Dekel & Birnboim (2006) that the filamentary streams of cold gas from the cosmic web can penetrate into the central at $z > 2$ and effectively form stars.

Hierarchical multiple mergers of galaxies are also proposed as the formation scenario of massive early-type galaxies. In this scenario, the stellar mass of the galaxies are formed early in a number of galaxies and merge into one object (assemble) in later. Mergers of stellar components in this mode are more dry than the mergers of the stellar components in disk instability mode. Then the galaxies similar to normal ellipticals may be formed by this process. Referring to the cosmological numerical simulation by De Lucia et al. (2006), the peak of the formation epoch of the stars of elliptical galaxies is at $z \sim 2$ and assembled even at $z < 1$ (These epoch vary in each simulation but the trend is same). Therefore even though number density of elliptical galaxies increases till z$\sim$ 1, as it have been observed, they have old stellar populations. It is also predicted in De Lucia et al. (2006) that the disk instability mode is effective for the galaxies with stellar mass $\lesssim 10^{11.5}$ $M_\odot$ while the most massive galaxies with stellar mass $\sim 10^{12}$ $M_\odot$, like BCGs, are more likely to be formed via hierarchical mergers.

We need more discussion about the merger histories in hierarchical merger scenario in detail. In the simulation of De Lucia & Blaizot (2007), they predict that about 80% of the stellar mass of the BCGs are formed at $z = 3$ but the assembly of the stellar mass proceed at $z \sim 0.5$ via dry major or minor mergers. Stott et al. (2010) reported that there is no significant growth of the stellar mass of the BCGs at last 9-10 Gyr ($z \sim 1 - 1.5$). The bluer colors with increasing radius, some bluer cores (Bildfell et al. 2008) and some recent star formation in BCGs (Kaviraj et al. 2008; Pipino et al. 2009) are also reported, supporting the recent star-formation activities and/or mergers of bluer stellar components. Then the simple dry major and minor mergers in later may not be appropriate formation histories. Further discussions are also needed for the epoch of their assembly. Although based on similar hierarchical merger scenario, the BCGs are formed more early in the simulation of Ruszkowski & Springel (2009). Further observational constraints of merger histories at high redshift are required to constrain the actual formation histories of massive ellipticals.

Although there are difference in detail, the early-phase of both formation histories may be observed as the small cluster of multiple stellar components (clumps or galaxies) which are dynamically bounded. With the recent deep and high resolution NIR imaging data taken by the IR cameras on 8 m class telescopes or HST, we can now directly study them. Multiple stellar components of LABs and SMGs (e.g., Prescott et al. 2012; U12; Umehata et al. submitted) are very likely to be the candidates of such objects.

In the SSA22 protocluster, U12 found that most of the LABs host multiple stellar components in their Lyα halos by using deep K-band imaging data. They reported that the 40% of the LABs in the SSA22 protocluster are detected of more than two counterparts with $z_{\rm phot} \sim 3.1$ in K-band. They also reported that there are surface number density excess of the DRGs, HEROs and K-selected galaxies with $z_{\rm phot} \sim 3.1$ adjacent the LABs and ASTE/AzTEC 1.1 mm sources in the SSA22 protocluster. Note that even though stellar components are not detected with MOIRCS K-band imaging data, the stellar components of the LABs are detected with the existing deeper *HST* WFC3 $F160W$-band images (for

example, LAB35 in later). Multiple stellar components are also found in the beam sizes of the ASTE/AzTEC 1.1 mm sub-mm sources in the SSA22 field, from *Spitzer* IRAC imaging data and some of them have $z_{\rm phot} \sim 3$ (Umehata et al. submitted).

We conducted the NIR spectroscopic observations of some of the counterparts of the LABs and SMGs and confirmed more than one stellar components in almost all of them. Since Lyα emission are resonant scatter lines, the nebular emission lines like Hα and [O$_{\rm III}$] are more suitable to confirm the redshifts of the stellar components. We are going to discuss about the properties of these objects with multiple stellar components.

2. THE MULTIPLE COUNTERPARTS OF THE LABS AND SMGS IN THE SSA22 PROTOCLUSTER

2.1. The spectroscopically confirmed counterparts

We spectroscopically confirmed more than one counterparts for three LABs and two SMGs.

Figure 23, 24, 25 and 26 show the K-band images of the LABs and SMGs whose stellar components are confirmed by our NIR spectroscopic observations. We show *HST* WFC3 $F160W$-band image of LAB35 which we confirmed the redshift of a neighborhood. Here we describe the properties of each object.

LAB12:

We confirmed the redshift of the object **A** in Figure 23 at $z_{[\mathrm{OIII}]\lambda5007} = 3.0909$. This object have the color $J - K = 2.6$ and its SED is well fitted with that of a quiescent galaxy (§ 3.2.3 in Chapter 2). This object is also detected in 24 μm and X-ray, suggesting the presence of an dust-obscured AGN. The object marked B is a LBG which was confirmed to be at $z = 3.094$ by Steidel et al. (2003).

LAB16:

The object marked **A** is confirmed to be at $z_{[\mathrm{OIII}]\lambda5007} = 3.0689$. This object is likely to be at the void of the Lyα halo. There are other two objects with $z_{\mathrm{phot}} \sim 3.1$.

LAB30:

Two objects are observed in a same slit and confirmed to be at $z_{[\mathrm{OIII}]\lambda5007} = 3.0680$ and 3.0687. The redshift was also obtained from the optical spectroscopy at the center of the Lyα halo as $z = 3.086$ by Steidel et al. (2003), is redshifted to the systemic redshift by 1000 km $^{-1}$ from the stellar components.

LAB35:

We show *HST* WFC3 *F160W*-band image instead of the MOIRCS K-band image. We confirmed the object **A** at $z_{\mathrm{H}\beta} = 3.0482$ ($z_{\mathrm{Ly}\alpha} = 3.120$ by Lehmer et al. 2009b) which is located near LAB35 and itself surrounded by extended Lyα emission which may be slightly smaller than the criterion of LABs. This object have red color $J - K = 2.4$ and well fitted with the SED of a quiescent galaxy. We fit the *F160W*-band image with a Sérsic model (Sersic 1968) using GALFIT software (Peng et al. 2002) in K13. We obtained Sérsic profile parameters of $r_e = 0.91 \pm 0.03$ kpc and $n = 4.51 \pm 0.51$. Such a profile is "de Vaucouleurs like" and significantly compact, resembling the red compact massive galaxies observed at $z > 2$ in other recent papers (e.g., van Dokkum et al. 2008; Kriek et al. 2009; Gobat et al. 2012). The object marked **B** is confirmed to be at $z = 3.028$, may not associate with object **B**. There is also an DRG with $z_{\mathrm{phot}} \sim 3.1$ marked with a red circle.

AzTEC99:

There are some stellar components detected in the beam size $\sim 30''.0$ of ASTE/AzTEC 1.1 mm. The beam size means the uncertainty of the positions of the sources. The object

marked with circle was confirmed to be at $z_{[\mathrm{OIII}]\lambda5007} = 3.0973$ from our observation. It have red color $J - K = 2.2$, detected in 24 μm and its SED is fitted with that of a dusty star-forming galaxy (§ 3.2.3 in Chapter 2). The bright object at right top of the figure are also detected in 24 μm. Since the right top bright object is likely to be a local object, the object we confirmed are more likely to be responsible for the sub-mm source.

LAB01:

LAB01 is known as one of the largest LABs (Steidel et al. 2000). The spatial extent of Lyα emission of this object is $\sim$ 150 kpc. There are six plausible K-band counterparts in LAB01 (U12) which are marked with circles in Figure 25.

We observed the objects marked as **A** and **B** and confirmed them to be at $z_{[\mathrm{OIII}]\lambda5007} = 3.1000$ and $z_{[\mathrm{OIII}]\lambda5007} = 3.1007$. The object **A** and R3 are the 24 μm sources (Webb et al. 2009). The object **A** have red color $J-K = 1.3$ and its SED is well fitted with that of a dusty starburst galaxy. $[\mathrm{O_{III}}]\lambda5007/\mathrm{H}\beta$ ratio of this object is lower than the star-forming galaxies at high redshift (§ 3.2.2 in Chapter 2). On the other hand, the object **B** is a most luminous source in rest-frame UV of LAB01. The objects marked C11 and C15 was performed the NIR spectroscopy by McLinden et al. 2013. The redshift of C11 is $z_{[\mathrm{OIII}]\lambda5007} = 3.1002$ and C15 is $z_{[\mathrm{OIII}]\lambda5007} = 3.0983$. The redshift of R3 is $z = 3.097$, which was obtained with SAURON rest-frame UV spatial spectroscopy by Weijmans et al. (2010). They obtained the redshift by fitting both Lyα emission line and absorption feature, which may be similar to the systemic redshift.

AzTEC14:

We observed the objects **A**, **B** and **C** with the VPH-K grism and the object **D** with $HK500$ grism. The objects **A** and **B** are confirmed to be at $z_{[\mathrm{OIII}]\lambda5007} = 3.0851$, 3.0926 and 3.0854. As seen in Figure 27, the object **A** have the $[\mathrm{O_{III}}]\lambda5007$ emission line with clear double peaks, suggesting the presence of out-flow or a merger event. The object **C** is at $z_{\mathrm{H}\alpha} = 2.0786$. The object **D** is confirmed to be at $z = 3.0 - 3.15$ from its Balmer/4000Å breaks. The objects **A** and **D** have very red colors $J - K = 2.8$ and their SEDs are well fitted with that of the quiescent galaxies (§ 3.4.3). The object **A** is detected in X-ray and its $[\mathrm{O_{III}}]\lambda5007/\mathrm{H}\beta$ ratio is similar to local AGNs. The object F is a LBG confirmed to be at $z = 3.086$ by optical spectroscopy (Steidel et al. 2003). The objects marked with circles have the photometric redshift $\sim$ 3.1.

From the IRAM PdB 1.4 GHz observation with more high resolution by Umehata et al. submitted, the sub-mm source is found to be the object E. Further spectroscopic follow up observations are needed.

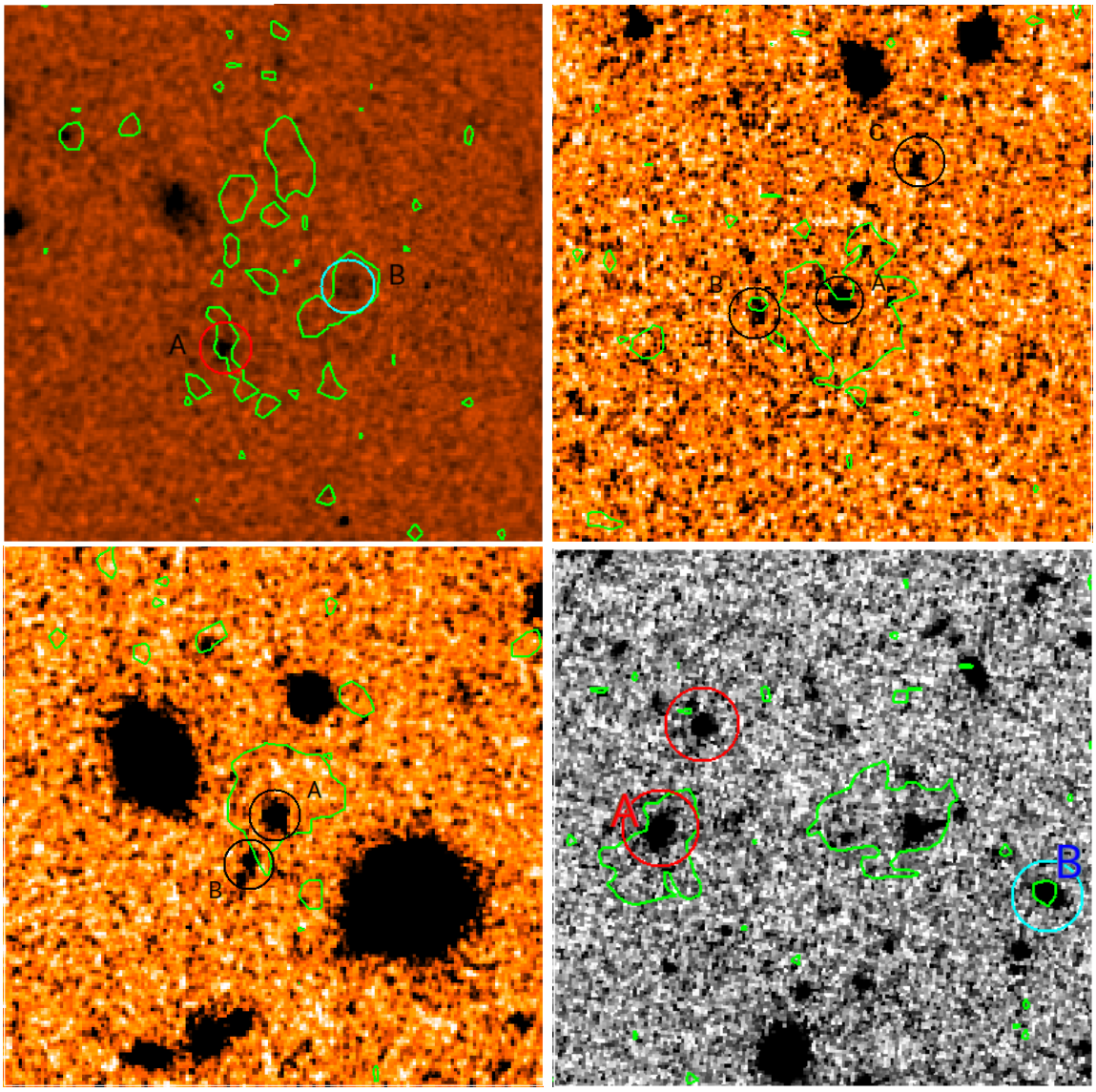

FIG. 23.— The MOIRCS K-band images of LAB12 (*left top*), 16 (*right top*) and 30 (*left bottom*). *right bottom* is the *HST* WFC3 160W-band image of LAB 35. Sizes of each figure are $20'' \times 20''$. Circles are the objects with $z_{\rm phot} \sim 3.1$. Red are the DRGs and cyan are previously confirmed the redshifts from other studies. Green contours are the iso-photal luminosity area of Lyα emission.

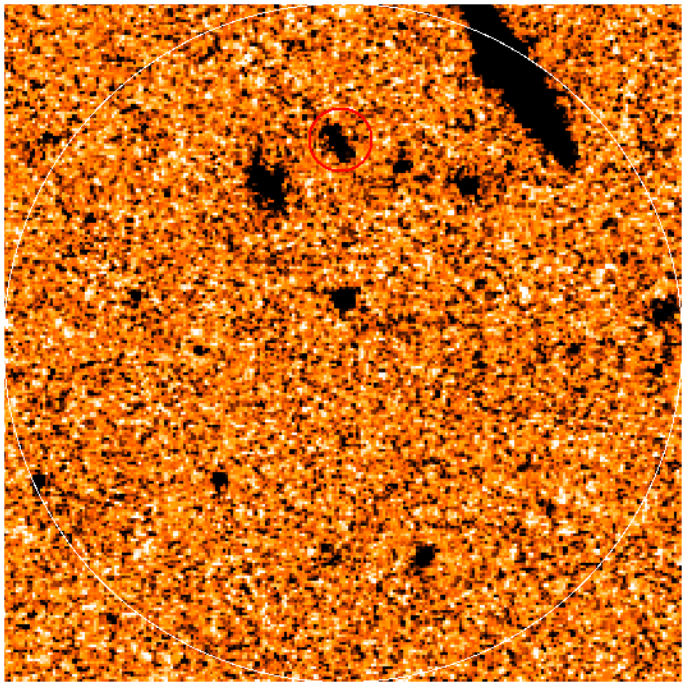

FIG. 24.— MOIRCS K-band images of AzTEC 99. Similar to Figure 23 but the size of the figure is $30'' \times 30''$. Large white circle is the beam size of ASTE/AzTEC $30''.0$.

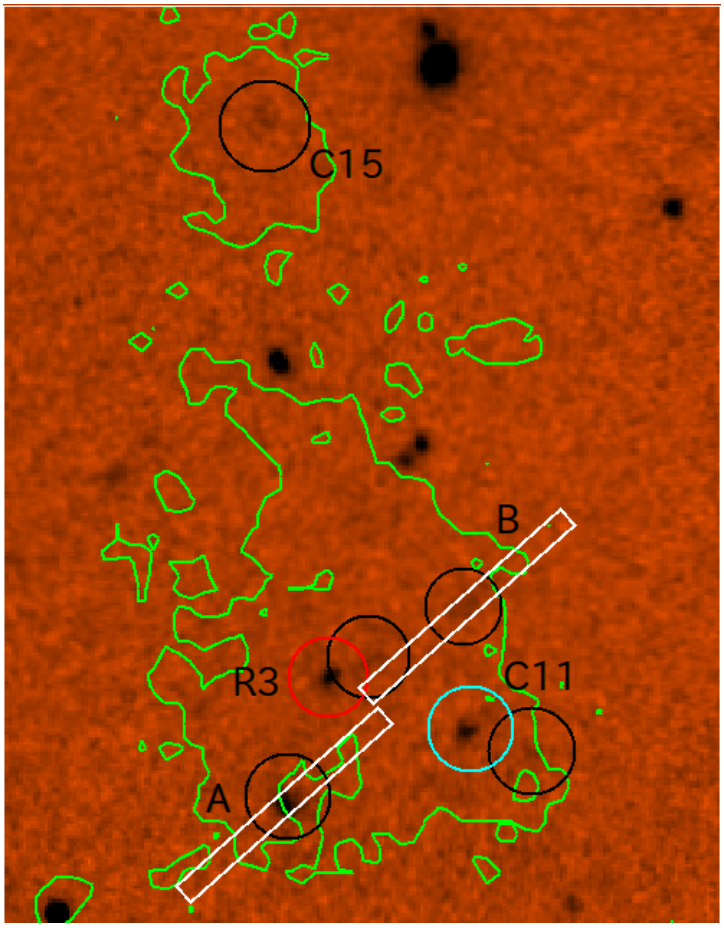

FIG. 25.— MOIRCS K-band images of LAB01 (*top*) the size of the figure is $40'' \times 30''$. White boxes are the slit used in the observations.

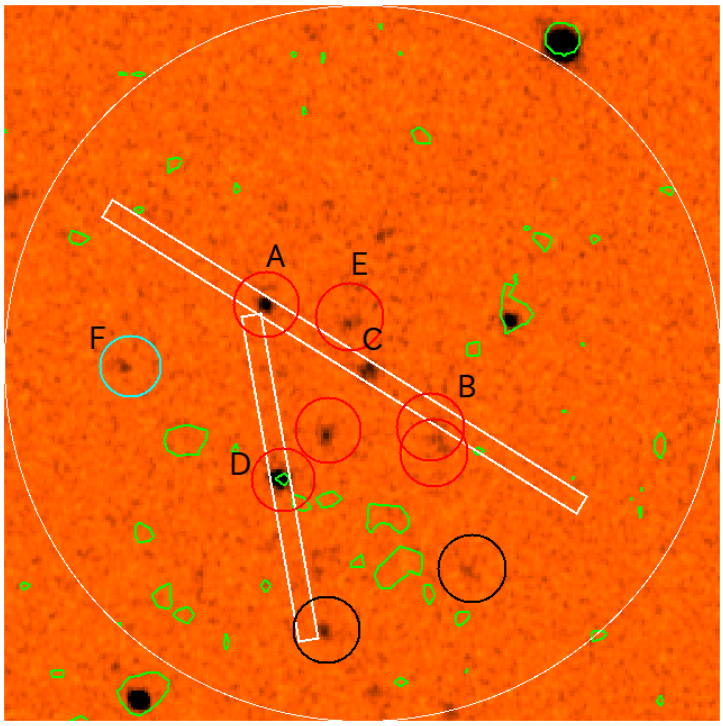

FIG. 26.— MOIRCS K-band images of AzTEC 14 (*bottom*). Similar to Figure 25 but the size of the figure is $30'' \times 30''$.

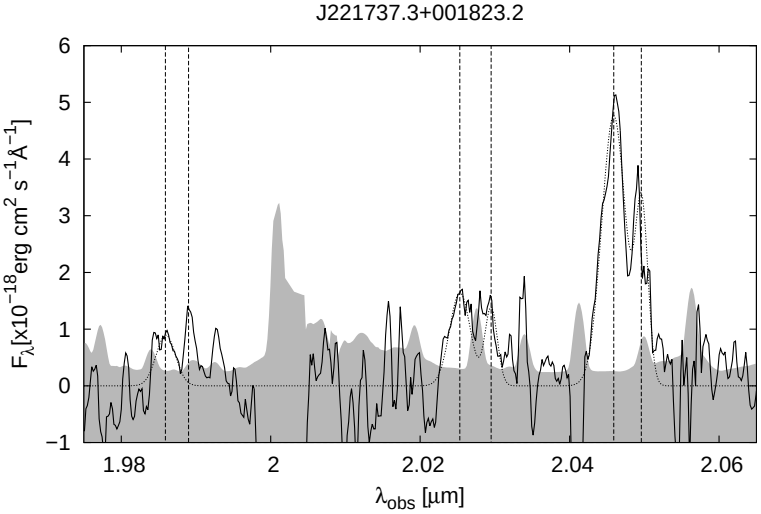

FIG. 27.— The NIR spectra of the object **A** of AzTEC 14. There are clear double peaks at $z_{[\mathrm{OIII}]\lambda5007} = 3.0851$ and 3.0926.

2.2. The dynamical properties

First of all, we should clarify whether these multiple counterparts are gravitationally bounded systems by using the spectroscopically confirmed redshifts.

The escape velocity from an object with mass M and size R (in diameter) is given as $\sqrt{GM/R}$. We assume the total stellar mass of each object, which is the sum of the stellar mass of the stellar components with $z_{\rm best} = 2.6 - 3.6$, as mass M. The sizes of each object are given from the spatial extent of the Lyα halo and the objects, which are lower limits but most of the mass of the systems should be within this sizes.

Then we measure the offset of the velocity from the median redshift ($\Delta z_{\rm median}$, $\Delta v_{\rm median}$) or the redshift of most massive object taking as center ($\Delta v_{\rm center}$). For the purpose, systemic redshifts measured from the nebular emission lines, in this case, [O III] emission line is more robust measure since Lyα emission line is a resonant scattering line, which can be redshifted for several 100 km s^{-1}. The errors of redshifts obtained from the [O III] emission lines are the residual of the Gaussian fitting of the emission lines while the resolutions of the VPH-K grism corresponds to Δv ∼150 km s^{-1} or ∼300 kpc.

LAB01

$\Delta v_{\rm median} = 22 \pm 22$ km s^{-1} (**A**), $\Delta v_{\rm median} = 29 \pm 7$ km s^{-1} (**B**) and $\Delta v_{\rm median} = 7 \pm 7$ km s^{-1} (**C11**) with $z_{\rm median} = 3.1003$ while $\Delta v_{\rm center} = 51 \pm 26$ km s^{-1} (**B**) and $\Delta v_{\rm center} = 14 \pm 26$ km s^{-1} (**C11**) taking the object **A** at $z_{\rm [OIII]} = 3.1000 \pm 0.0003$ as a center. We rejected the object C15, which is too separated from LAB01 to consider as a counterpart of LAB01. The redshift range of the objects corresponds to ≈ 110 kpc in physical scale, which is similar to the extent of Lyα halo on the sphere. The spatial extent of Lyα emission of LAB01 is ≈ 150 kpc. The total stellar mass of the system is $\sim 2 \times 10^{11}$ M$_\odot$. And the escape velocity obtained to be ∼80 km s^{-1}. They are likely to be gravitationally bound system.

AzTEC 14

$\Delta v_{\rm median} = 29 \pm 7$ km s^{-1} (**A**), $\Delta v_{\rm median} = 521 \pm 22$ km s^{-1} (**A**, second component), $\Delta v_{\rm median} = 7 \pm 22$ km s^{-1} (**B**) and $\Delta v_{\rm median} = 36 \pm 73$ km s^{-1} (**F**) with $z_{\rm median} = 3.0855$ while $\Delta v_{\rm median} = 551 \pm 23$ km s^{-1} (**A**, second component), $\Delta v_{\rm center} = 22 \pm 23$ km s^{-1} (**B**) and $\Delta v_{\rm center} = 66 \pm 74$ km s^{-1} (**F**) taking the object **A** at $z_{\rm [OIII]} = 3.0851 \pm 0.0001$ as a center. The spatial extent of Az14 is similar to LAB01. The total stellar mass of the system is $\sim 4 \times 10^{11}$ M$_\odot$. And the escape velocity obtained to be ∼110 km s^{-1}. The redshift separation of the double components of the object **A** corresponds to 1200 kpc, too large to regard as the objects bounded in a same system. This component may be the back-ground object or more plausibly, suffering from strong outflow of a central AGN. It can also happen that this component is an object which first close to but now fry off from the system, similar to some members of Stephan's Quitent, a compact group of galaxies in the local universe, reported by Renaud et al. (2010). The redshift range of the objects corresponds to ≈ 140 kpc in physical scale which is comparable to the distribution of the objects on the sphere. Note that since the redshift of the object **F** was obtained by archival rest-frame UV spectroscopy, it can be redshifted for a few 100 km s^{-1}.

LAB12

$\Delta v_{\rm median} = 114 \pm 29$ km s^{-1} (**A**) and $\Delta v_{\rm median} = 114 \pm 73$ km s^{-1} (**B**) with $z_{\rm median} = 3.0925$ while $\Delta v_{\rm center} = 227 \pm 79$ km s^{-1} (**B**) taking the object **A** at $z_{\rm [OIII]} = 3.0909 \pm 0.0004$ as a center. The spatial extent of the Lyα halo of LAB12 is roughly 30 kpc. The redshift offset of the two objects corresponds to $\approx$480 kpc in physical scale. The total stellar mass of the system is $\sim 1.5 \times 10^{11}$ M$_\odot$. And the escape velocity obtained to be $\sim$150 km s^{-1}. Note that since the redshift of the object **B** was obtained by archival rest-frame UV spectroscopy, it can be redshifted for a few 100 km s^{-1}.

LAB30

$\Delta v_{\rm median} = 26 \pm 22$ km s^{-1} (**A**) and $\Delta v_{\rm median} = 26 \pm 29$ km s^{-1} (**B**) with $z_{\rm median} = 3.0684$ while $\Delta v_{\rm center} = 51 \pm 37$ km s^{-1} (**B**) taking the object **A** at $z_{\rm [OIII]} = 3.0680 \pm 0.0003$ as a center. The spatial extent of Lyα halo of LAB30 is roughly 50 kpc. The redshift offset of the two objects corresponds to $\approx$60 kpc in physical scale. The total stellar mass of the system is $\sim 3 \times 10^{10}$ M$_\odot$. And the escape velocity obtained to be $\sim$50 km s^{-1}.

The stellar components of almost all of the objects are with very small velocity offsets which are smaller than the escape velocities of each system.

These velocity offset values are similar to those of the compact groups of galaxies ($\lesssim$ 100 kpc) in the local universe, which have not already been settled to the dynamical equilibrium (e.g., Tully 1987; Karachentsev 2000; Sulentic et al. 2001; Renaud et al. 2010). It was reported in Renaud et al. (2010), in which the dynamical evolution of the galaxies in Stephan's Quintet (Stephan 1877) was simulated, that not all the galaxies in this system are likely to be merge into one object while some objects may fry off. Aceves (2001) reported from numerical simulations of triplet galaxies that only 10% of the triplet are going to merge into one object in $\sim$6 Gyr, comparable to the time between $z = 3$ to $z = 1$. The situation of our multiple galaxies may be not the same as these simulations but we need to treat them carefully.

Precise analysis of the dynamical properties is not available to date but at least, the multiple counterparts of the LABs and SMGs are gravitationally bounded. This may be for the first time to identify the dynamically bounded multiple stellar components at $z > 3$ from the rest-frame optical spectroscopic observations. From these above, we treat the objects with multiple stellar components which are on-going multiple interaction and mergers.

2.3. The properties of the counterparts

Suppose that the photo-z and color selected counterparts of the LABs and the SMGs are also likely to associate with them, we are going to investigate the properties of the stellar components assuming them to be at $z \approx 3.09$.

Figure 28 shows the stellar mass v.s. SFR distributions of the stellar components of the LABs and SMGs. SFRs are estimated from the extinction corrected rest-frame UV luminosity using the reddening estimated from the SED fitting procedure. There is 24 μm (and also Herschel) data but the depth is insufficient to constrain the SFR < 1000 $M_\odot$ yr^{-1}. The LABs and SMGs with more than two K-band counterparts with $z_{\rm phot} \sim 3.1$ are plotted in the figure.

The lack of the low-mass counterparts in the SMGs may be due to the dust obscuration since the stellar mass depends on both K-band flux value and the SEDs of the galaxies. Especially the strongly dust obscured galaxies and old quiescent galaxies are missed since they have large stellar mass to V-band luminosity ratios. Then the galaxies with stellar mass smaller than $10^{10.5}$ $M_\odot$ can be missed from the figure.

The stellar mass ratio of the first and second massive stellar components in each object are on average 2:3. There would be at least one major merger in each object. There are more massive stellar components in the SMGs. Total stellar mass of the detected counterparts are also higher for the SMGs.

Figure 29 shows the specific SFR v.s. stellar mass distribution of the counterparts of the LABs and SMGs in the SSA22 field. The specific SFR is the SFR divided by the stellar mass, which indicate the current star-formation activity of the galaxies. The most massive galaxies of the SMGs have low-sSFR, they are likely to be dominated by old stellar populations. In the previous section, we also confirmed the quiescent galaxies in LAB12 (and near LAB35) while the Lyα emission of LAB12 (and also LAB35) is detected only sparsely.

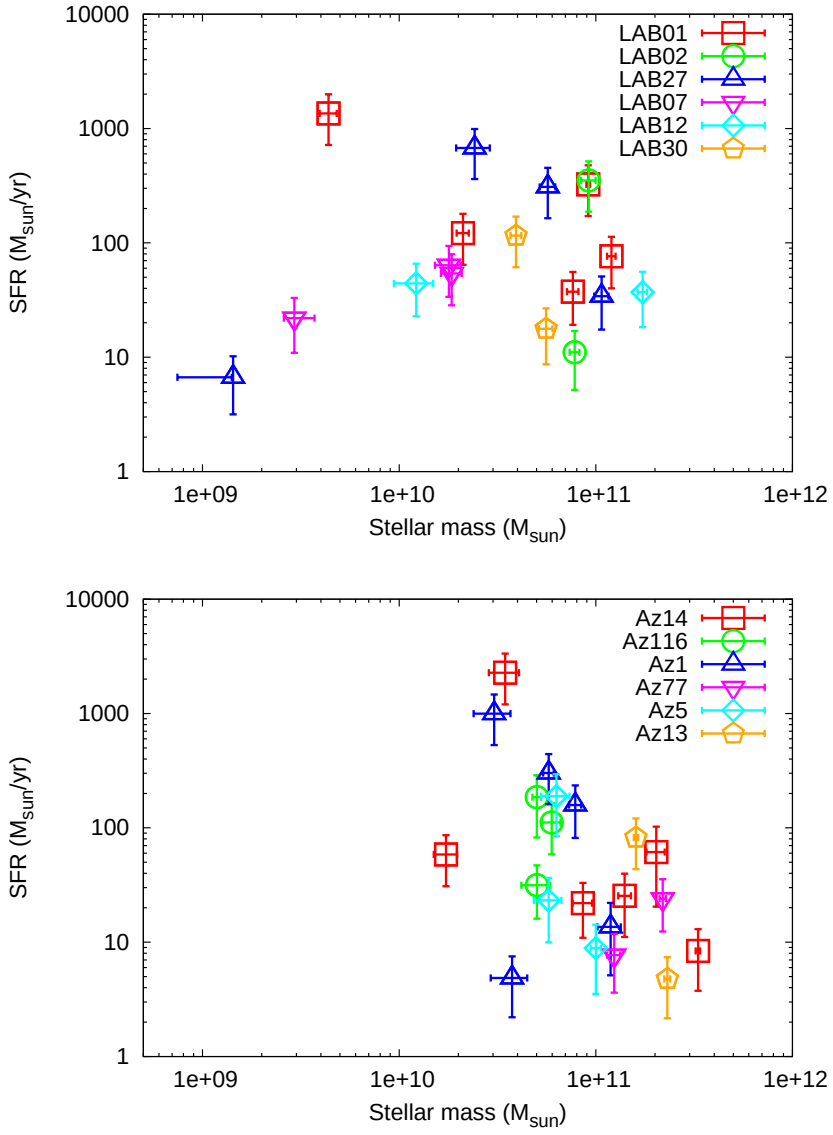

FIG. 28.— Stellar mass v.s. SFR distributions of the stellar components of the LABs (*top*) and SMGs (*bottom*). This is the preliminary results estimated based on the Salpeter IMF.

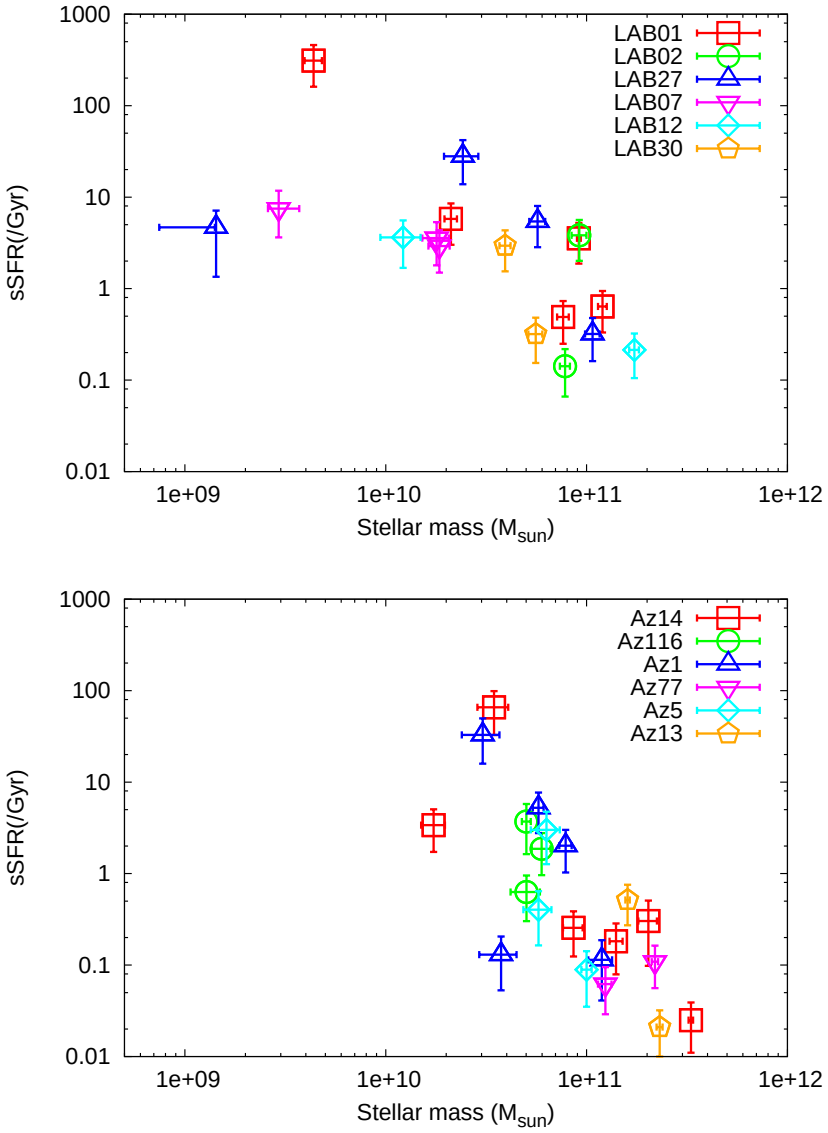

FIG. 29.— Stellar mass v.s. specific SFR distributions of the stellar components of the LABs (*top*) and SMGs (*bottom*).

3. DISCUSSION

Reminding the § 1 of this chapter, the multiple merging galaxies are likely to be the early-phase of formation histories of massive elliptical galaxies thorough two process; disk instability and multiple hierarchical mergers. The stellar components of the multiple merging galaxies in the SSA22 protocluster have various properties. Do they have the properties consistent with these scenarios?

AzTEC 14 is very likely to be the case of hierarchical multiple mergers. There are two massive and quiescent objects with the ages $\sim$ 1.5 Gyr. It is not likely the case for the disk instability scenario in which stellar components merge into the central object in relatively short timescale < 0.5 Gyr and old stellar components may not remain except for a central object. The total stellar mass of this object is already $4{\times}10^{11}$ $M_{\odot}$ (It become $6{\times}10^{11}$ $M_{\odot}$ assuming the Salpeter IMF). Even though this object is one of the progenitors of most massive galaxies in clusters of galaxies in the current universe, namely brightest cluster galaxies with stellar mass $1-2\times10^{12}$ $M_{\odot}$ (e.g., Stott et al. 2010), bulk of the stellar mass of this object are likely to be formed in each stellar component. The merger induced starburst may be not so dominant for this object. From these above, the properties of the stellar components of AzTEC 14 are consistent with those in the hierarchical multiple merger scenario predicted in the cosmological numerical simulations. Some objects, especially SMGs also host multiple quiescent stellar components and are likely to be hierarchical multiple mergers too.

It is difficult to separate the disk instability and young hierarchical multiple mergers from the ages of the stellar components. This scenario may be plausible for some LABs since they have younger stellar components. It beyonds our scope since they may be distinguishable with the analysis of motions of the stellar components and gas. Further observations e.g., using ALMA, are required to constrain these properties.

On the other hand, the disk instability mode can effectively form massive and passively evolving galaxies even at high redshift. Then they can be responsible for the formation of massive quiescent stellar components already exist in some LABs and SMGs. Certainly, one of the counterparts of LAB35 with the stellar population dominated by old stellar population shows the structure similar to compact ellipticals (K13). In this picture, compact massive ellipticals are observed at high redshift but they experience a number of mergers in later and become normal elliptical galaxies observed in the local universe.

There are other interesting implications from the multiple merging galaxies; the difference between LABs and SMGs.

It is also important results that the SMGs and LABs are similar in hosting multiple stellar components, spatial extent and at the same redshift (when Lyα emission line must be detectable in the existing narrow-band data) but the SMGs show no significant Lyα emission. Then the multiple merging galaxies will be good targets to study the mysterious origin of the Lyα emission of large LABs like LAB01. The difference of the evolution stage of the system may take part for these differences, since the SMGs have older and more quiescent stellar components. This is also supported from that the LABs with massive quiescent stellar components (LAB35 and LAB12) show weaker Lyα emission.

4. CONCLUTION

We have studied the multiple stellar components of the LABs and SMGs in the SSA22 field, which are likely to be the early-phase of formation history of massive early-type galaxies predicted from the cosmological numerical simulations.

From the NIR spectroscopic observations, we confirmed the redshifts of these stellar components. Their velocity offsets are much smaller than the escape velocities. Then they are likely to be dynamically bounded systems.

We consider two scenarios for multiple mergers of stellar components; the in situ clump mergers of disk instabilities and hierarchical multiple mergers of galaxies. Some of the multiple merging galaxies have more than two massive and old stellar components, which are responsible for the hierarchical multiple merger scenario. In this case, bulk of the stars are likely to be formed in each stellar component and merger induced starburst may not be so dominant.

This may be for the first time to identify the multiple merging objects at high redshift and investigate the stellar populations of such many objects. It should note that since there are many LABs and SMGs detected of significant multiple stellar components in the SSA22 protocluster, they may be frequent mode of massive galaxy formation in the protocluster.

Our study is only the first step for these newly found objects. We need further studies of them, e.g., environmental dependence, sizes and ISM properties. Larger sample of LABs obtained by Hyper-Suprime-Cam surveys and ALMA observations of each multiple mergers will enable us to answer these questions.

Chap.4. Summary

Summary

We studied the formation histories of massive early-type galaxies by using the deep NIR imaging and spectroscopic data of the protocluster at $z = 3.09$ in the SSA22 field.

The SSA22 protocluster is well characterized as one of the progenitors of most massive clusters in the current universe.

We investigated the properties of the galaxies in this protocluster. A large stellar mass, about half of the center of Coma cluster have already been formed. There are already some massive quiescent galaxies formed in the protocluster. This may be for the first time to confirm the associations of such a cluster of massive quiescent galaxies with the protocluster at $z > 3$. Most of massive quiescent galaxies confirmed are AGNs with similar or slightly higher X-ray luminosity as local massive galaxies. They show relatively lower activities than the other AGNs in the protocluster. This suggests that quenching of star-formation activities via AGN feedback is plausible mechanism for the early formation of massive quiescent galaxies.

We also studied the LABs and SMGs with multiple stellar components in the SSA22 protocluster, which may be early-phase of formation history of massive early-type galaxies, predicted by the cosmological numerical simulations. We spectroscopically confirmed them as dynamically bounded systems, maybe for the first time. Properties of some of them are well fitted with hierarchical merging scenario predicted in the cosmological numerical simulations.

From these above, we showed how early massive early-type galaxies appear and found some hints for their formation histories (e.g., AGNs and hierarchical multiple mergers), in most massive clusters in the current universe. Future studies are required to confirm these pictures.

Acknowledgememt

First of all, I would like to thank Prof. Toru Yamada for giving continuous grateful educations from when I was an undergraduate student to now.

I would like to thank to the collaborators of my first (and second) paper and MOIRCS team, Dr. Yuka K. Uchimoto, Masaru Kajisawa, Takashi Ichikawa, Yuichi Matsuda, Masayuki Akiyama, Tomoki Hayashino, Masayuki Konishi, Tetsuo Nishimura, Koji Omata, Ryuji Suzuki, Ichi Tanaka, Chihiro Tokoku, Tomohiro Yoshikawa, David. M. Alexander, Giovanni. G. Fazio, Ja-Sheng. Huang and Bret. D. Lehmer for not only providing useful data and also a plenty of advices.

I would also like to thank to Dr. Yoichi Tamura and Hideki Umehata, the ASTE/AzTEC observers of the SSA22 field for providing the updated source catalog and valuable discussions.

I would like to thank the Subaru Telescope staff for many help and support for the observations. There was sudden accidents just before my observations but I can obtain very useful data owing to their great efforts. I would also like to thank for the developers of the VPH-K grism, Dr. Noboru Ebizuka, Kashiko Kodate and so on.

I would also like to thank the staffs and students of Astronomical Institute of Tohoku university.

This study is based on data collected at Subaru Telescope, which is operated by the National Astronomical Observatory of Japan. Our studies owe a lot deal to the archival Subaru MOIRCS (Uchimoto et al. (2012)), Suprime-Cam (Matsuda et al. 2004), *Spitzer* IRAC & MIPS data taken in Webb et al. (2009), *Chandra* data taken in Lehmer et al. (2009a) and ASTE/AzTEC source catalog (Umehata et al. submitted). I thank to all the collaborators for providing wonderful data. This work was supported by Global COE Program "Weaving Science Web beyond Particle-Matter Hierarchy", MEXT, Japan.

Funding for the SDSS and SDSS-II has been provided by the Alfred P. Sloan Foundation, the Participating Institutions, the National Science Foundation, the U.S. Department of Energy, the National Aeronautics and Space Administration, the Japanese Monbukagakusho, the Max Planck Society, and the Higher Education Funding Council for England. The SDSS Web Site is http://www.sdss.org/. The SDSS is managed by the Astrophysical Research Consortium for the Participating Institutions. The Participating Institutions are the American Museum of Natural History, Astrophysical Institute Potsdam, University of Basel, University of Cambridge, Case Western Reserve University, University of Chicago, Drexel University, Fermilab, the Institute for Advanced Study, the Japan Participation Group, Johns Hopkins University, the Joint Institute for Nuclear Astrophysics, the Kavli Institute for Particle Astrophysics and Cosmology, the Korean Scientist Group, the Chinese Academy of Sciences, Los Alamos National Laboratory, the Max-Planck-Institute for Astronomy, the Max-Planck-Institute for Astrophysics, New Mexico State University, Ohio State University, University of Pittsburgh, University of Portsmouth, Princeton University, the United States Naval Observatory, and the University of Washington.

REFERENCES

Aceves, H. 2001, MNRAS, 326, 1412

Adelberger, K. L., Steidel, C. C., Pettini, M., et al. 2005, ApJ, 619, 697

Baldwin, J. A., Phillips, M. M., & Terlevich, R. 1981, PASP, 93, 5

Bell, E. F., McIntosh, D. H., Katz, N., & Weinberg, M. D. 2003, ApJS, 149, 289

Bertin, E., & Arnouts, S. 1996, A&AS, 117, 393

Bildfell, C., Hoekstra, H., Babul, A., & Mahdavi, A. 2008, MNRAS, 389, 1637

Birnboim, Y., & Dekel, A. 2003, MNRAS, 345, 349

Blakeslee, J. P., Franx, M., Postman, M., et al. 2003, ApJ, 596, L143

Bolzonella, M., Miralles, J.-M., & Pelló, R. 2000, A&A, 363, 476

Bournaud, F., Elmegreen, B. G., & Elmegreen, D. M. 2007, ApJ, 670, 237

Bower, R. G., Benson, A. J., Malbon, R., et al. 2006, MNRAS, 370, 645

Bower, R. G., Lucey, J. R., & Ellis, R. S. 1992, MNRAS, 254, 601

Bruzual, G., & Charlot, S. 2003, MNRAS, 344, 1000

Calzetti, D., Armus, L., Bohlin, R. C., et al. 2000, ApJ, 533, 682

Cassata, P., Giavalisco, M., Guo, Y., et al. 2011, ApJ, 743, 96

Cassata, P., Giavalisco, M., Williams, C. C., et al. 2013, ApJ, 775, 106

Chabrier, G. 2003, PASP, 115, 763

Cowie, L. L., Hu, E. M., & Songaila, A. 1995, AJ, 110, 1576

Croton, D. J., Springel, V., White, S. D. M., et al. 2006, MNRAS, 365, 11

Daddi, E., Röttgering, H. J. A., Labbé, I., et al. 2003, ApJ, 588, 50

Daddi, E., Renzini, A., Pirzkal, N., et al. 2005, ApJ, 626, 680

Daddi, E., Alexander, D. M., Dickinson, M., et al. 2007, ApJ, 670, 173

De Lucia, G., & Blaizot, J. 2007, MNRAS, 375, 2

De Lucia, G., Springel, V., White, S. D. M., Croton, D., & Kauffmann, G. 2006, MNRAS, 366, 499

de Propris, R., Eisenhardt, P. R., Stanford, S. A., & Dickinson, M. 1998, ApJ, 503, L45

de Propris, R., Stanford, S. A., Eisenhardt, P. R., Dickinson, M., & Elston, R. 1999, AJ, 118, 719

De Propris, R., Stanford, S. A., Eisenhardt, P. R., Holden, B. P., & Rosati, P. 2007, AJ, 133, 2209

Dekel, A., & Birnboim, Y. 2006, MNRAS, 368, 2

Dekel, A., Sari, R., & Ceverino, D. 2009a, ApJ, 703, 785

Dekel, A., Birnboim, Y., Engel, G., et al. 2009b, Nature, 457, 451

Digby-North, J. A., Nandra, K., Laird, E. S., et al. 2010, MNRAS, 407, 846

Doherty, M., Tanaka, M., De Breuck, C., et al. 2010, A&A, 509, A83

Dressler, A. 1980, ApJ, 236, 351

Dressler, A., & Gunn, J. E. 1983, ApJ, 270, 7

Ebizuka, N., Ichiyama, K., Yamada, T., et al. 2011, PASJ, 63, 605

Eggen, O. J., Lynden-Bell, D., & Sandage, A. R. 1962, ApJ, 136, 748

Eke, V. R., Navarro, J. F., & Frenk, C. S. 1998, ApJ, 503, 569

Ellis, R. S., Smail, I., Dressler, A., et al. 1997, ApJ, 483, 582
Elmegreen, B. G., & Elmegreen, D. M. 2005, ApJ, 627, 632
Elmegreen, D. M., Elmegreen, B. G., & Hirst, A. C. 2004, ApJ, 604, L21
Erb, D. K., Shapley, A. E., Pettini, M., et al. 2006a, ApJ, 644, 813
Erb, D. K., Steidel, C. C., Shapley, A. E., et al. 2006b, ApJ, 646, 107
Finkelstein, S. L., Rhoads, J. E., Malhotra, S., Pirzkal, N., & Wang, J. 2007, ApJ, 660, 1023
Franx, M., Labbé, I., Rudnick, G., et al. 2003, ApJ, 587, L79
Gawiser, E., van Dokkum, P. G., Gronwall, C., et al. 2006, ApJ, 642, L13
Gawiser, E., Francke, H., Lai, K., et al. 2007, ApJ, 671, 278
Gobat, R., Strazzullo, V., Daddi, E., et al. 2012, ApJ, 759, L44
Gunn, J. E., & Gott, III, J. R. 1972, ApJ, 176, 1
Hayashino, T., Matsuda, Y., Tamura, H., et al. 2004, AJ, 128, 2073
Hopkins, A. M., & Beacom, J. F. 2006, ApJ, 651, 142
Ichikawa, T., Suzuki, R., Tokoku, C., et al. 2007, PASJ, 59, 1081
Jones, T. M., Kriek, M., van Dokkum, P. G., et al. 2013, ArXiv e-prints
Juneau, S., Dickinson, M., Alexander, D. M., & Salim, S. 2011, ApJ, 736, 104
Kaiser, N. 1984, ApJ, 284, L9
Kajisawa, M., Konishi, M., Suzuki, R., et al. 2006, PASJ, 58, 951
Kajisawa, M., Ichikawa, T., Tanaka, I., et al. 2011, PASJ, 63, 379
Karachentsev, I. D. 2000, in Astronomical Society of the Pacific Conference Series, Vol. 209, IAU Colloq. 174: Small Galaxy Groups, ed. M. J. Valtonen & C. Flynn, 1
Kauffmann, G., White, S. D. M., Heckman, T. M., et al. 2004, MNRAS, 353, 713
Kaviraj, S., Khochfar, S., Schawinski, K., et al. 2008, MNRAS, 388, 67
Kennicutt, Jr., R. C. 1998, ARA&A, 36, 189
Kewley, L. J., Dopita, M. A., Leitherer, C., et al. 2013a, ApJ, 774, 100
Kewley, L. J., Maier, C., Yabe, K., et al. 2013b, ApJ, 774, L10
Kodama, T., Arimoto, N., Barger, A. J., & Arag'on-Salamanca, A. 1998, A&A, 334, 99
Kodama, T., Tanaka, I., Kajisawa, M., et al. 2007, MNRAS, 377, 1717
Kormendy, J., & Richstone, D. 1995, ARA&A, 33, 581
Kriek, M., van Dokkum, P. G., Labbé, I., et al. 2009, ApJ, 700, 221
Kriss, G. 1994, Astronomical Data Analysis Software and Systems, 3, 437
Kubo, M., Uchimoto, Y. K., Yamada, T., et al. 2013, ApJ, 778, 170
Kuiper, E., Hatch, N. A., Röttgering, H. J. A., et al. 2010, MNRAS, 405, 969
Kulas, K. R., McLean, I. S., Shapley, A. E., et al. 2013, ApJ, 774, 130
Kurk, J. D., Pentericci, L., Röttgering, H. J. A., & Miley, G. K. 2004, A&A, 428, 793
Labbé, I., Huang, J., Franx, M., et al. 2005, ApJ, 624, L81
Lai, K., Huang, J.-S., Fazio, G., et al. 2008, ApJ, 674, 70
Le Floc'h, E., Papovich, C., Dole, H., et al. 2005, ApJ, 632, 169
Lehmer, B. D., Alexander, D. M., Geach, J. E., et al. 2009a, ApJ, 691, 687
Lehmer, B. D., Alexander, D. M., Chapman, S. C., et al. 2009b, MNRAS, 400, 299
Lin, Y.-T., Mohr, J. J., Gonzalez, A. H., & Stanford, S. A. 2006, ApJ, 650, L99
Magorrian, J., Tremaine, S., Richstone, D., et al. 1998, AJ, 115, 2285
Maiolino, R., Nagao, T., Grazian, A., et al. 2008, A&A, 488, 463

Mannucci, F., Cresci, G., Maiolino, R., et al. 2009, MNRAS, 398, 1915
Matsuda, Y., Yamada, T., Hayashino, T., et al. 2004, AJ, 128, 569
—. 2005, ApJ, 634, L125
Matsuda, Y., Smail, I., Geach, J. E., et al. 2011, MNRAS, 416, 2041
Mawatari, K., Yamada, T., Nakamura, Y., Hayashino, T., & Matsuda, Y. 2012, ApJ, 759, 133
McLinden, E. M., Malhotra, S., Rhoads, J. E., et al. 2013, ApJ, 767, 48
Meza, A., Navarro, J. F., Steinmetz, M., & Eke, V. R. 2003, ApJ, 590, 619
Mo, H. J., & White, S. D. M. 1996, MNRAS, 282, 347
—. 2002, MNRAS, 336, 112
Mullaney, J. R., Pannella, M., Daddi, E., et al. 2012, MNRAS, 419, 95
Naab, T., Johansson, P. H., Ostriker, J. P., & Efstathiou, G. 2007, ApJ, 658, 710
Noguchi, M. 1999, ApJ, 514, 77
Oemler, Jr., A. 1974, ApJ, 194, 1
Ono, Y., Ouchi, M., Shimasaku, K., et al. 2010, ApJ, 724, 1524
Ouchi, M., Shimasaku, K., Akiyama, M., et al. 2008, ApJS, 176, 301
Ouchi, M., Shimasaku, K., Furusawa, H., et al. 2010, ApJ, 723, 869
Overzier, R. A., Shu, X., Zheng, W., et al. 2009, ApJ, 704, 548
Papovich, C., Dickinson, M., & Ferguson, H. C. 2001, ApJ, 559, 620
Papovich, C., Moustakas, L. A., Dickinson, M., et al. 2006, ApJ, 640, 92
Peng, C. Y., Ho, L. C., Impey, C. D., & Rix, H.-W. 2002, AJ, 124, 266
Pettini, M., Shapley, A. E., Steidel, C. C., et al. 2001, ApJ, 554, 981
Pipino, A., Kaviraj, S., Bildfell, C., et al. 2009, MNRAS, 395, 462
Poggianti, B. M., Calvi, R., Bindoni, D., et al. 2013, ApJ, 762, 77
Polletta, M., Tajer, M., Maraschi, L., et al. 2007, ApJ, 663, 81
Prescott, M. K. M., Dey, A., Brodwin, M., et al. 2012, ApJ, 752, 86
Quadri, R., van Dokkum, P., Gawiser, E., et al. 2007, ApJ, 654, 138
Quadri, R. F., Williams, R. J., Lee, K.-S., et al. 2008, ApJ, 685, L1
Renaud, F., Appleton, P. N., & Xu, C. K. 2010, ApJ, 724, 80
Rosario, D. J., Santini, P., Lutz, D., et al. 2012, A&A, 545, A45
Rosario, D. J., Mozena, M., Wuyts, S., et al. 2013, ApJ, 763, 59
Ruszkowski, M., & Springel, V. 2009, ApJ, 696, 1094
Salpeter, E. E. 1955, ApJ, 121, 161
Sersic, J. L. 1968, Atlas de galaxias australes
Shapley, A. E., Steidel, C. C., Adelberger, K. L., et al. 2001, ApJ, 562, 95
Sheth, R. K., & Tormen, G. 1999, MNRAS, 308, 119
Skrutskie, M. F., Cutri, R. M., Stiening, R., et al. 2006, AJ, 131, 1163
Spitler, L. R., Labbé, I., Glazebrook, K., et al. 2012, ApJ, 748, L21
Springel, V., White, S. D. M., Jenkins, A., et al. 2005, Nature, 435, 629
Stanford, S. A., Eisenhardt, P. R., & Dickinson, M. 1998, ApJ, 492, 461
Steidel, C. C., Adelberger, K. L., Dickinson, M., et al. 1998, ApJ, 492, 428
Steidel, C. C., Adelberger, K. L., Shapley, A. E., et al. 2005, ApJ, 626, 44
—. 2000, ApJ, 532, 170

—. 2003, ApJ, 592, 728
Steidel, C. C., Erb, D. K., Shapley, A. E., et al. 2010, ApJ, 717, 289
Stephan, M. 1877, MNRAS, 37, 334
Stetson, P. B. 1987, PASP, 99, 191
Stockton, A., Shih, H.-Y., Larson, K., & Mann, A. W. 2014, ApJ, 780, 134
Stott, J. P., Collins, C. A., Sahlén, M., et al. 2010, ApJ, 718, 23
Straatman, C. M. S., Labbé, I., Spitler, L. R., et al. 2013, ArXiv e-prints
Strazzullo, V., Rosati, P., Pannella, M., et al. 2010, A&A, 524, A17
Strazzullo, V., Gobat, R., Daddi, E., et al. 2013, ApJ, 772, 118
Sulentic, J. W., Rosado, M., Dultzin-Hacyan, D., et al. 2001, AJ, 122, 2993
Tamura, Y., Kohno, K., Nakanishi, K., et al. 2009, Nature, 459, 61
Tamura, Y., Iono, D., Wilner, D. J., et al. 2010, ApJ, 724, 1270
Tanaka, I., Breuck, C. D., Kurk, J. D., et al. 2011, PASJ, 63, 415
Tanaka, M., Finoguenov, A., Mirkazemi, M., et al. 2013, PASJ, 65, 17
Tokunaga, A. T., Simons, D. A., & Vacca, W. D. 2002, PASP, 114, 180
Toomre, A., & Toomre, J. 1972, ApJ, 178, 623
Toshikawa, J., Kashikawa, N., Ota, K., et al. 2012, ApJ, 750, 137
Tremonti, C. A., Heckman, T. M., Kauffmann, G., et al. 2004, ApJ, 613, 898
Trujillo, I., Förster Schreiber, N. M., Rudnick, G., et al. 2006, ApJ, 650, 18
Tully, R. B. 1987, ApJ, 321, 280
Uchimoto, Y. K., Suzuki, R., Tokoku, C., et al. 2008, PASJ, 60, 683
Uchimoto, Y. K., Yamada, T., Kajisawa, M., et al. 2012, ApJ, 750, 116
van Dokkum, P. G., Franx, M., Förster Schreiber, N. M., et al. 2004, ApJ, 611, 703
van Dokkum, P. G., Franx, M., Kriek, M., et al. 2008, ApJ, 677, L5
Venemans, B. P., Röttgering, H. J. A., Miley, G. K., et al. 2005, A&A, 431, 793
—. 2007, A&A, 461, 823
Verhamme, A., Schaerer, D., & Maselli, A. 2006, A&A, 460, 397
Webb, T. M. A., Yamada, T., Huang, J.-S., et al. 2009, ApJ, 692, 1561
Weijmans, A.-M., Bower, R. G., Geach, J. E., et al. 2010, MNRAS, 402, 2245
Yabe, K., Ohta, K., Iwamuro, F., et al. 2012, PASJ, 64, 60
Yamada, T., Nakamura, Y., Matsuda, Y., et al. 2012, AJ, 143, 79
Yamada, T., Kajisawa, M., Akiyama, M., et al. 2009, ApJ, 699, 1354
Yoshikawa, T., Akiyama, M., Kajisawa, M., et al. 2010, ApJ, 718, 112
Zirm, A. W., Toft, S., & Tanaka, M. 2012, ApJ, 744, 181
Zirm, A. W., van der Wel, A., Franx, M., et al. 2007, ApJ, 656, 66

APPENDIX

FIG. 30.— The spectra from the NIR spectroscopic observations

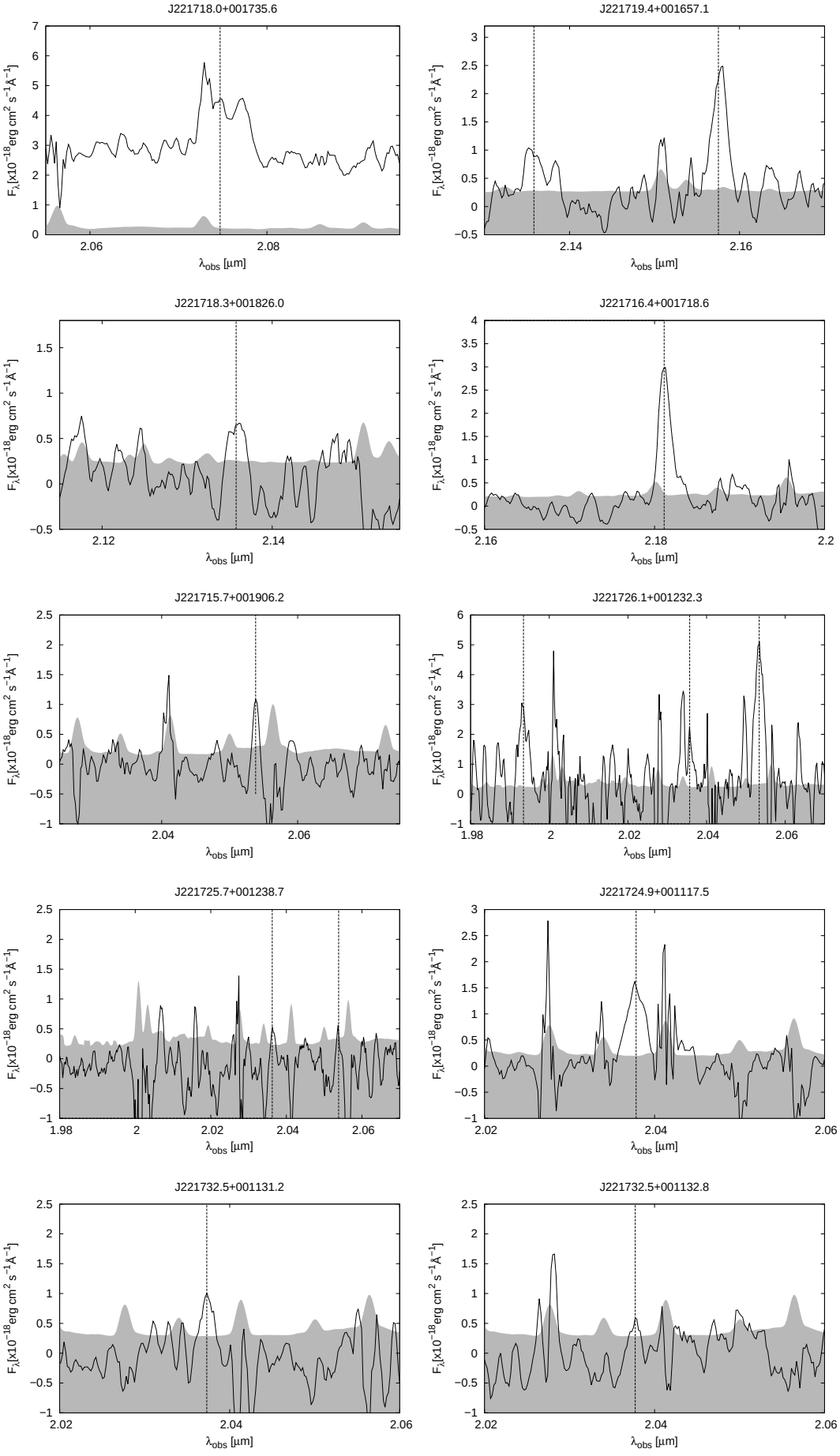

FIG. 31.— *Continued.*

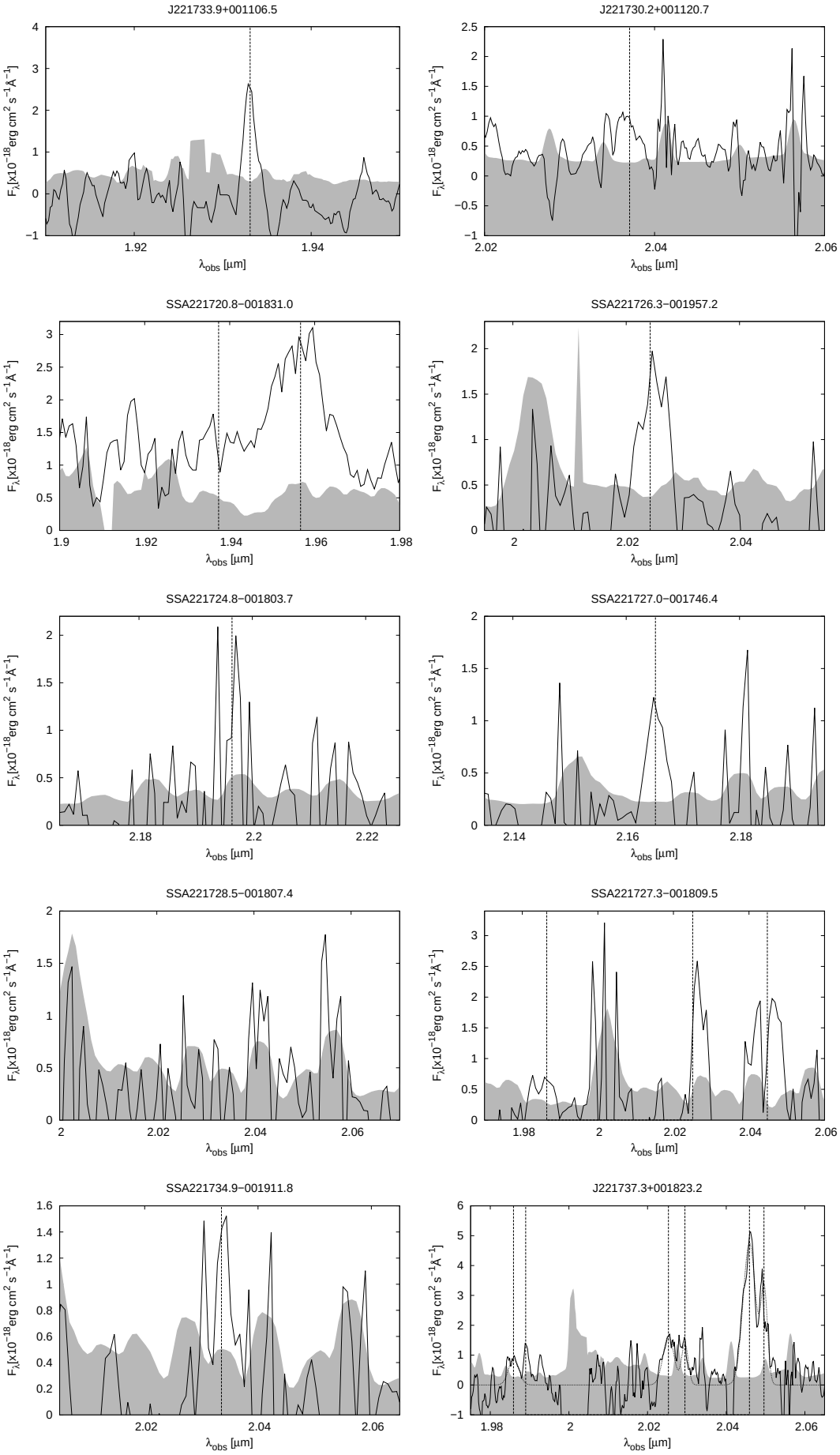

FIG. 31.— *Continued.*

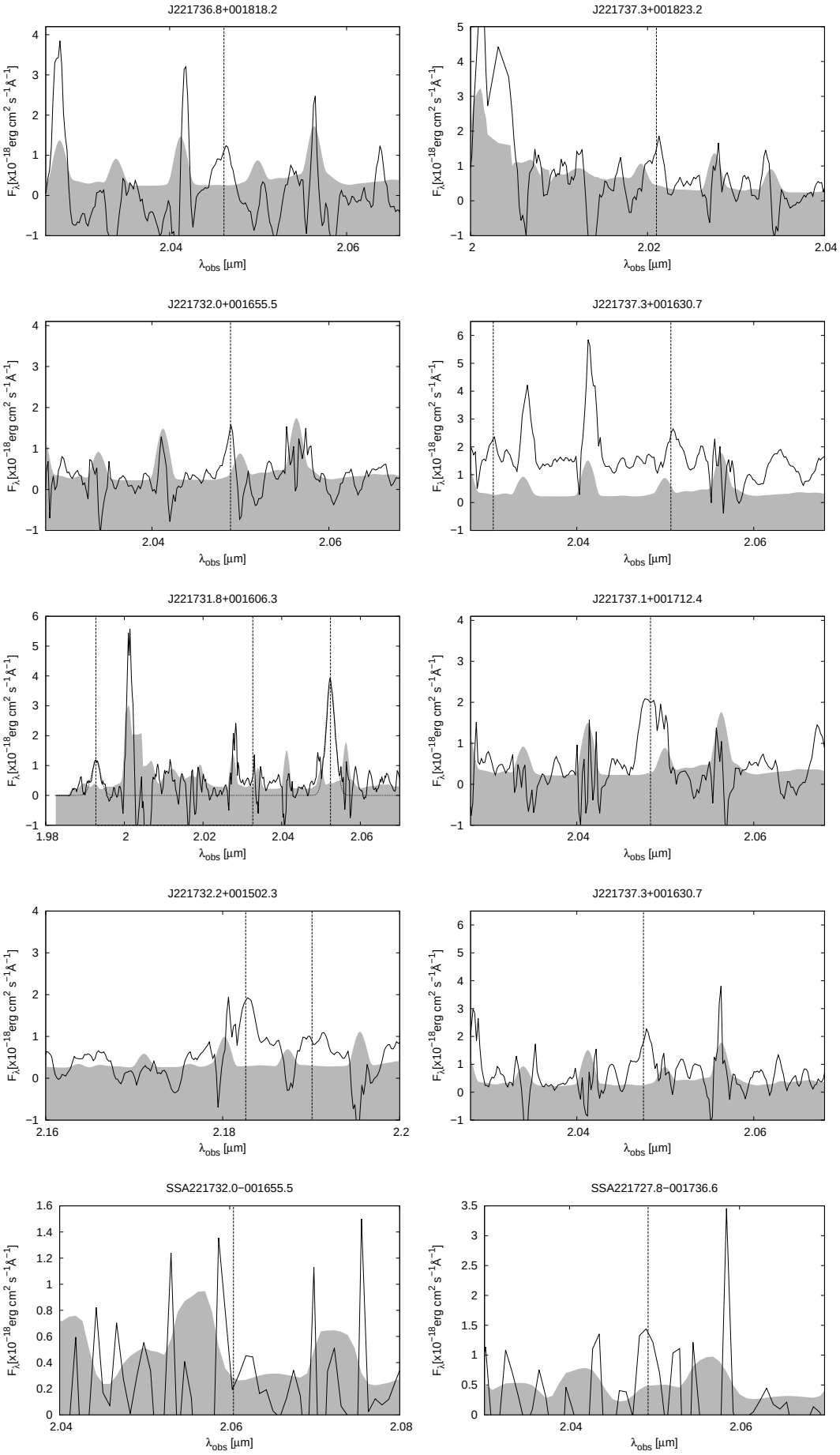

FIG. 31.— *Continued.*

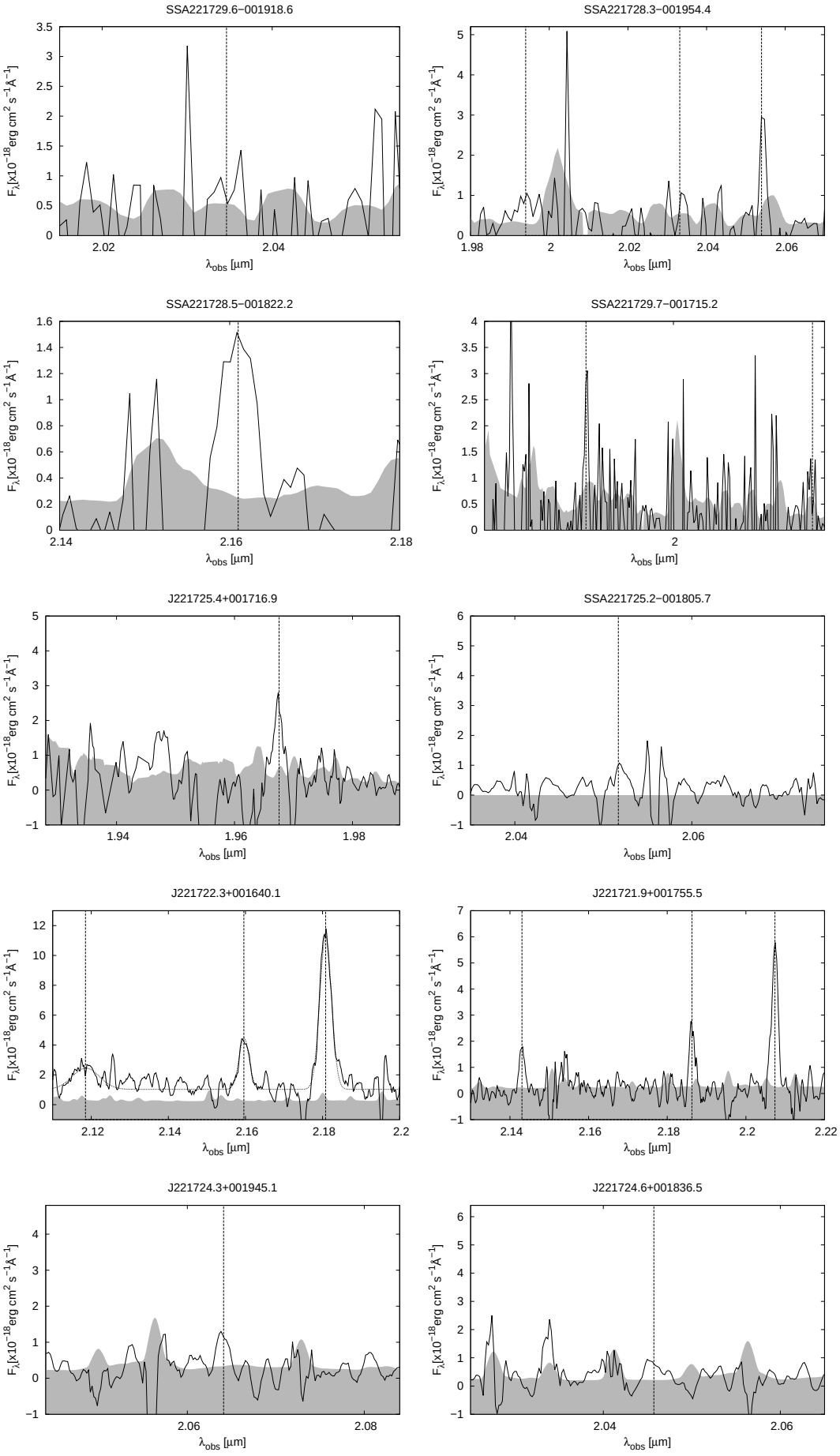

FIG. 31.— Black solid lines are the obtained spectra and the gray shaded region are 1σ background noise, which are the Poisson noise of the background. Dashed lines indicate the position of the emission lines.

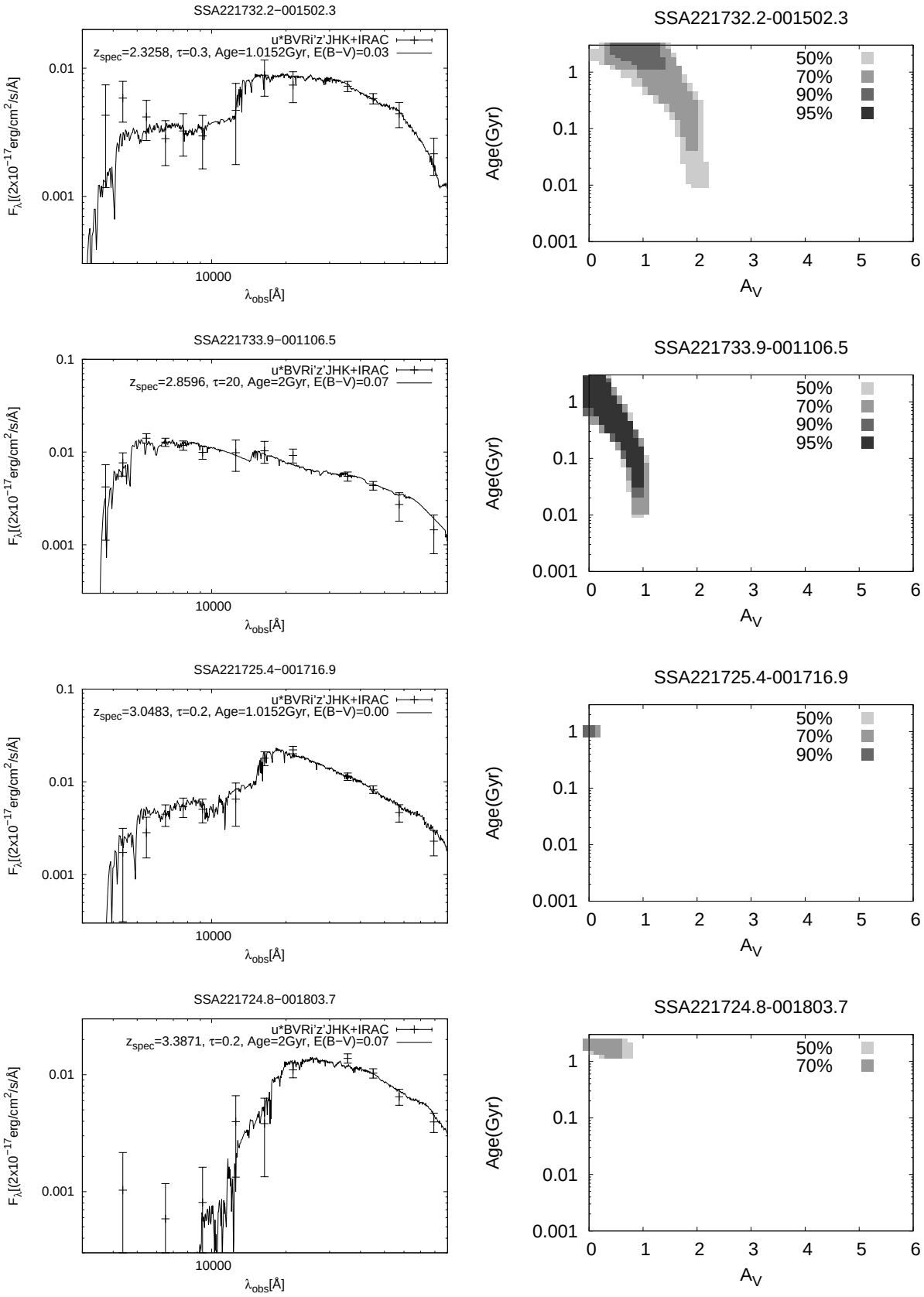

FIG. 32.— *Continued.*

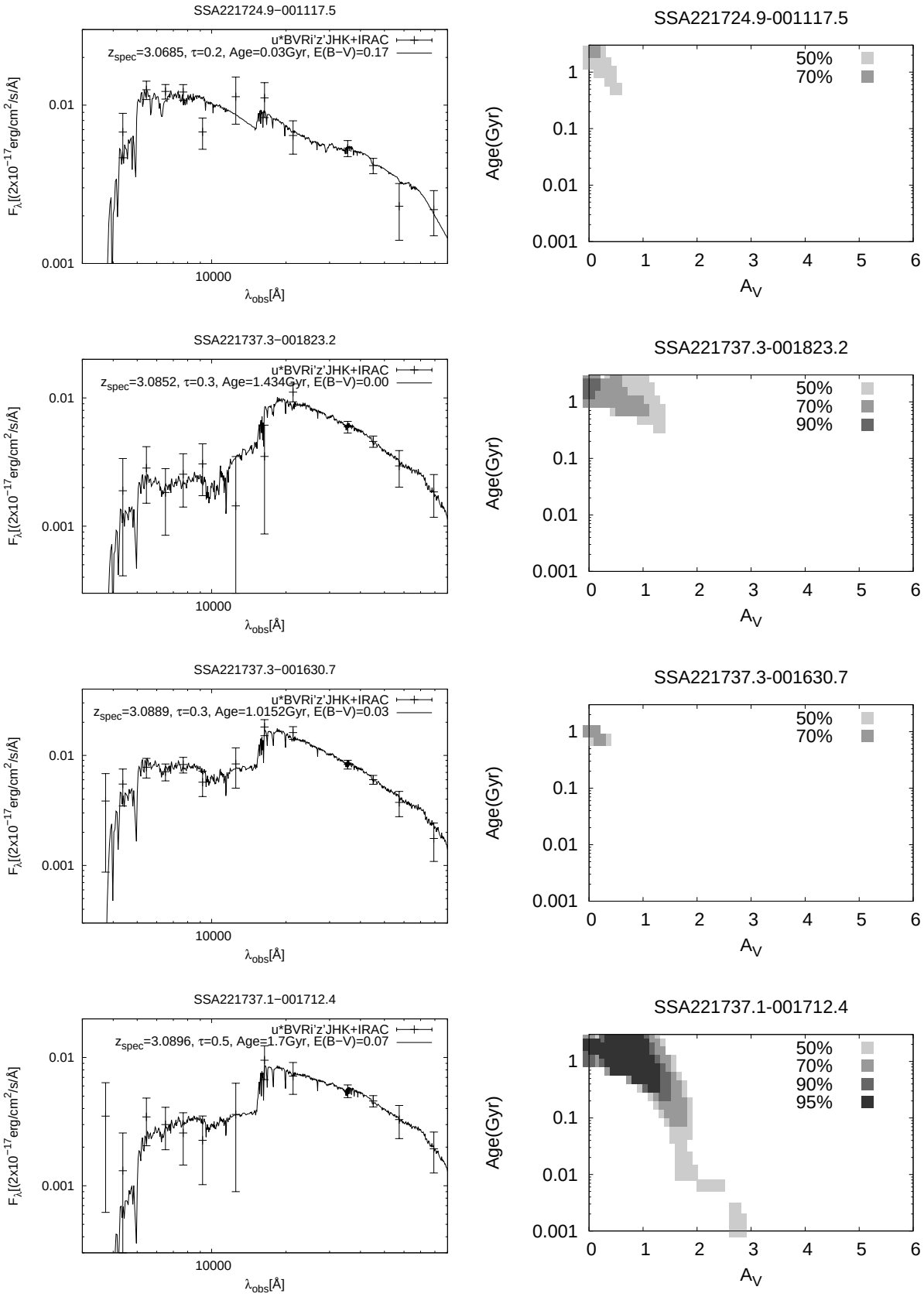

FIG. 32.— *Continued.*

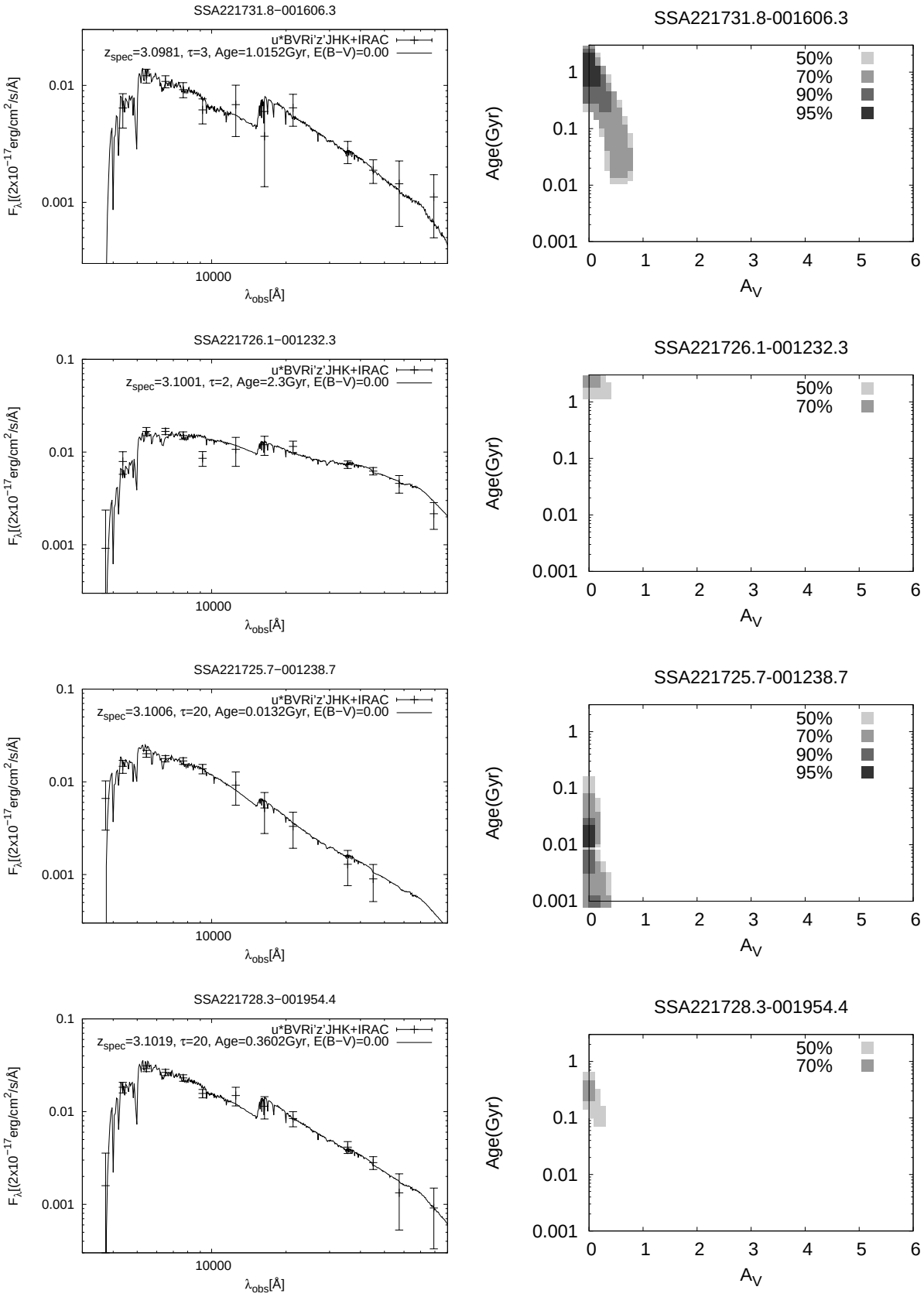

FIG. 32.— *Continued.*

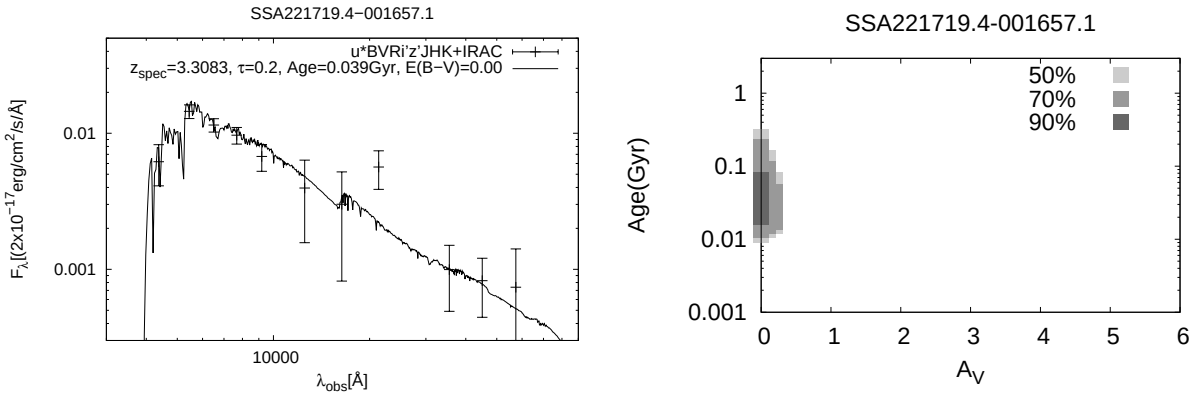

FIG. 32.— The best-fit SED models of the galaxies which are fitted with model SEDs of galaxies with $> 70\%$ confidence level. The cross points are the observed points of $u^\star, B, V, R, i', z', J, H, K$, 3.6$\mu$m, 4.5$\mu$m, 5.8$\mu$m and 8.0$\mu$m. The black solid lines are best fit SED models adopting single component model SEDs of galaxies. The red dashed lines are best fit SED models adopting two component model SEDs. The components are the conbination of two different model SED of galaxies or galaxies and QSOs.

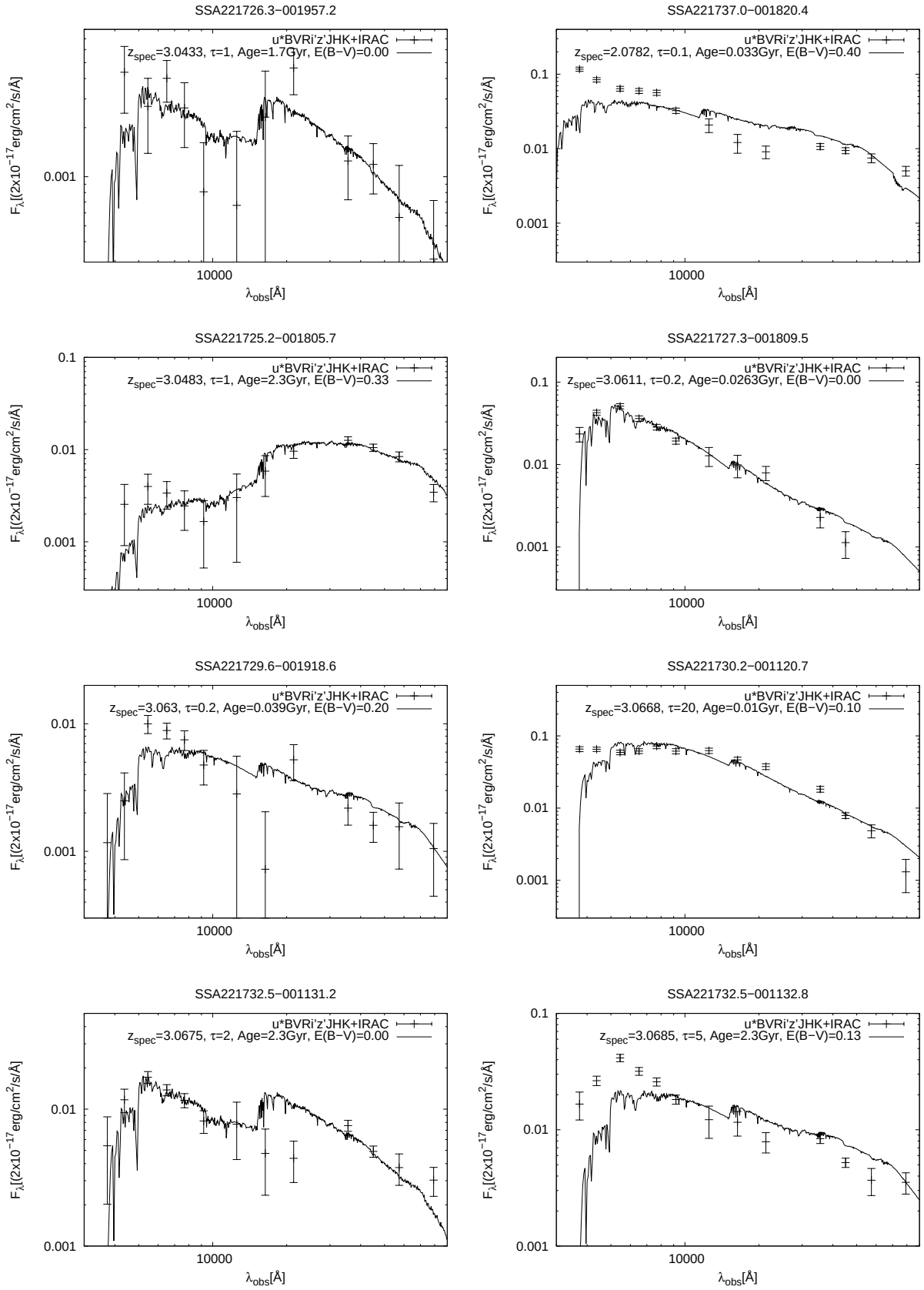

FIG. 33.— *Continued.*

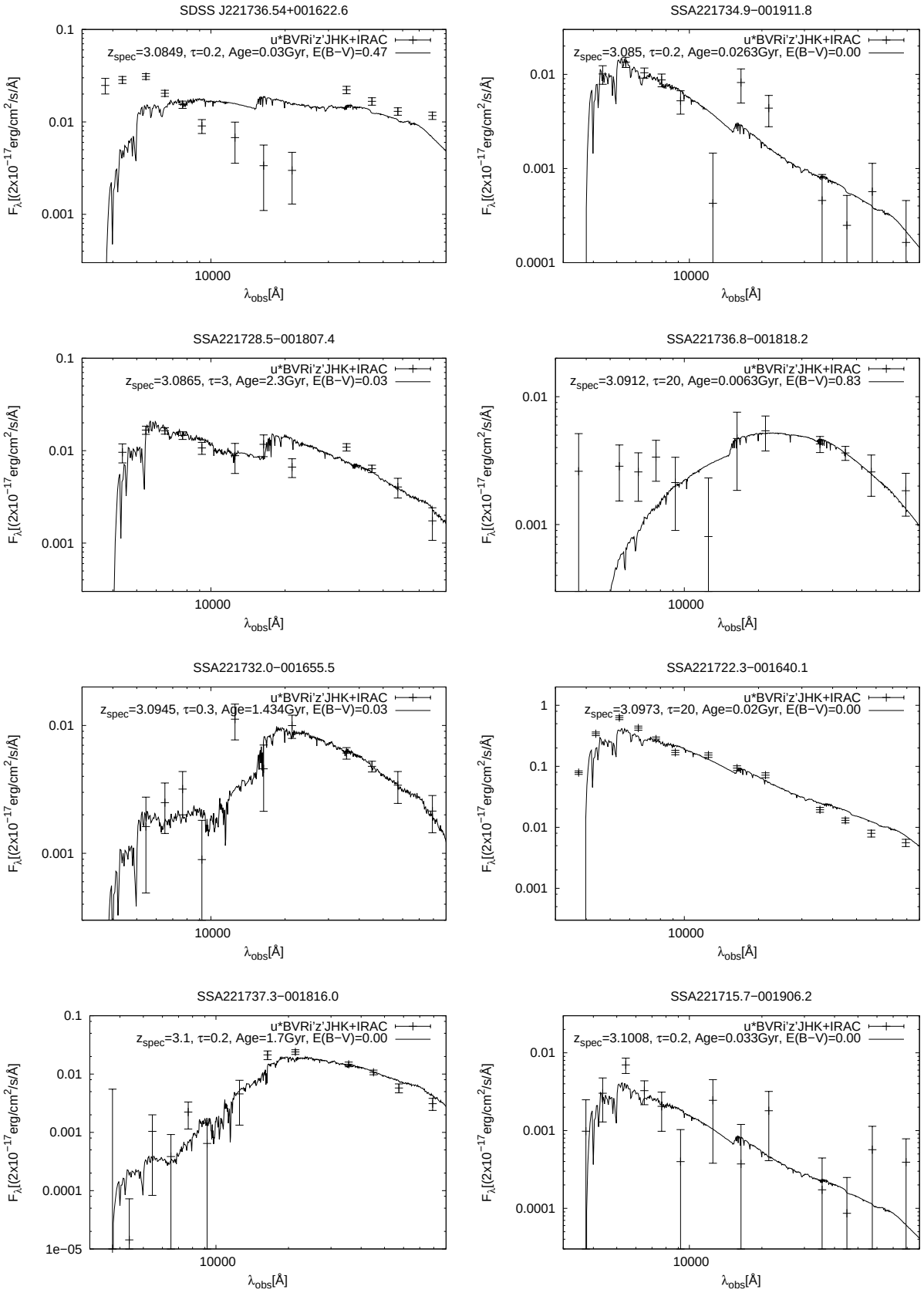

FIG. 33.— *Continued.*

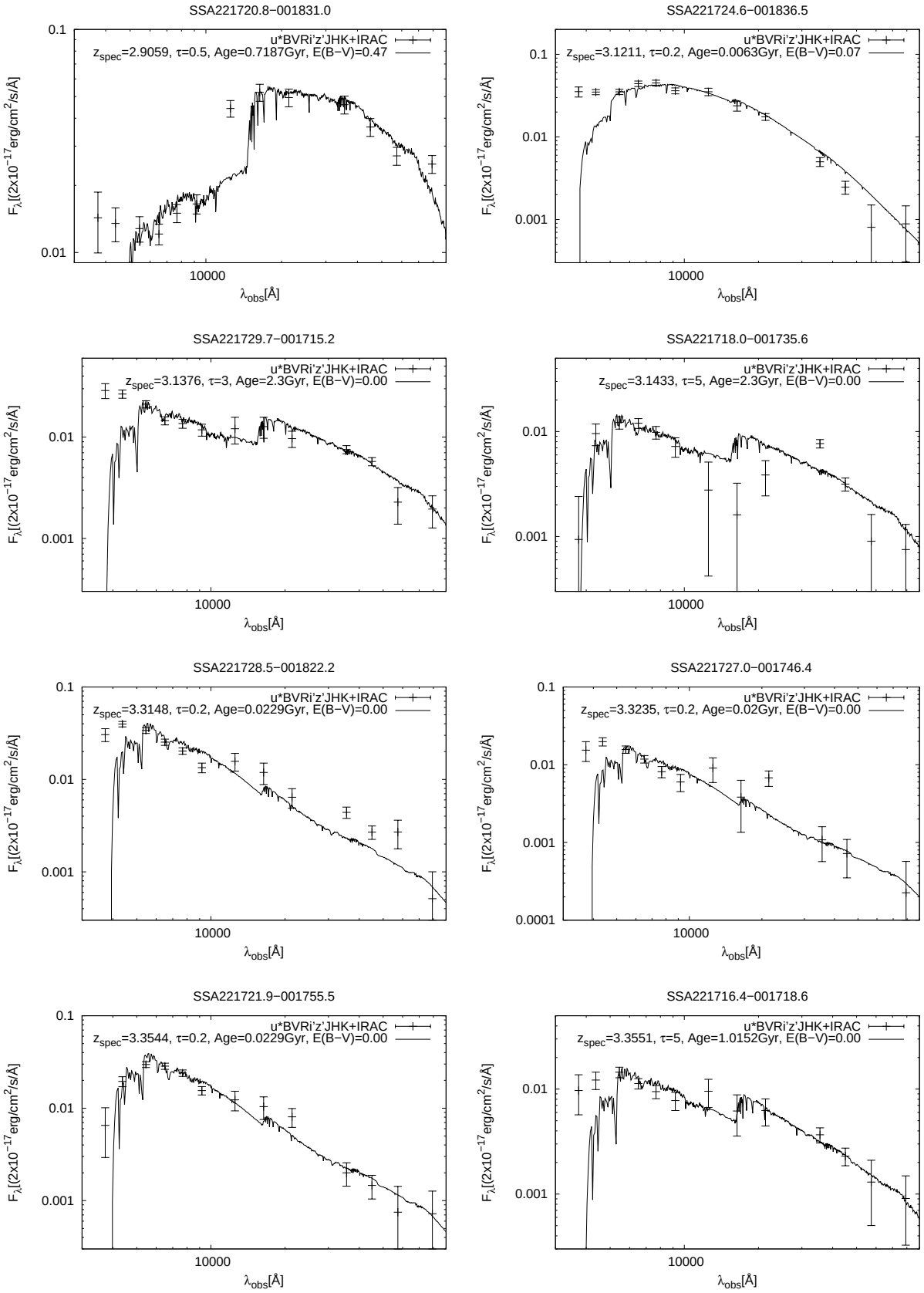

FIG. 33.— *Continued.*

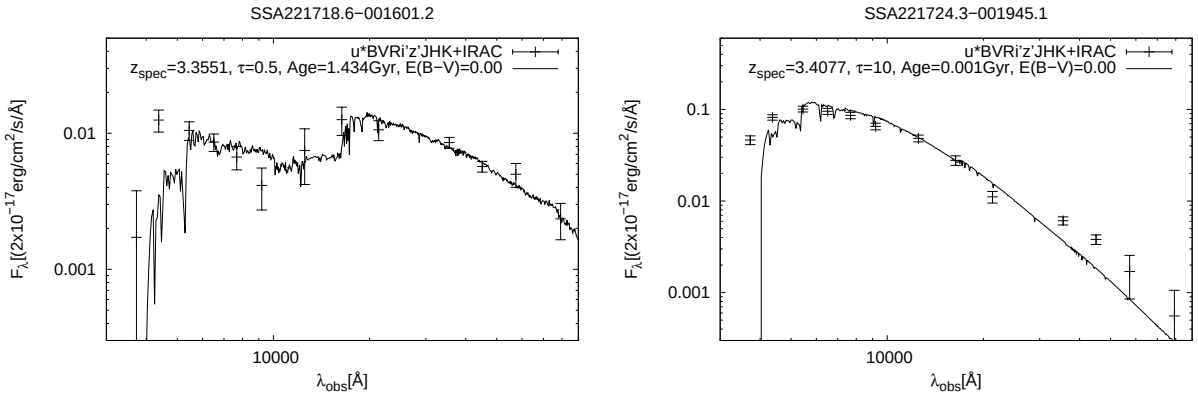

FIG. 33.— Similar to Fig. 32 but for the galaxies which are not well fitted with model SED of the galaxies above 70% confidence level.